CORA Cork Open Research Archive
Cartlann Taighde Oscailte Chorcaí

Title	Multi-scale modelling of atomic layer deposition
Authors	Shirazi, Mahdi
Publication date	2014
Original Citation	Shirazi, M. 2014. Multi-scale modelling of atomic layer deposition. PhD Thesis, University College Cork.
Type of publication	Doctoral thesis
Rights	© 2014, Mahdi Shirazi - http://creativecommons.org/licenses/by-nc-nd/3.0/
Download date	2026-11-04 14:29:40
Item downloaded from	https://hdl.handle.net/10468/1427

UCC
University College Cork, Ireland
Coláiste na hOllscoile Corcaigh

Multi-scale modelling of atomic layer deposition

Mahdi Shirazi



NATIONAL UNIVERSITY OF IRELAND, CORK

Department of Physics

Tyndall National Institute

Thesis submitted for the degree of Doctor of Philosophy

15 January 2014

Supervisors: Dr. Simon D. Elliott

Head of Department/School: Prof. John McInerney

Research supported by The Science Foundation Ireland

Contents

List of Tables iv
Acknowledgements vii
Abstract viii

1 Introduction **1**
1.1 Advantage of computer modelling 1
1.2 Application of atomic layer deposition 1
1.3 Motivation to study amide precursors 4
1.4 Computational studies of atomic layer deposition 6
1.4.1 Multiscale modelling of atomic layer deposition 6
1.4.2 Atomistic approach in homodeposition and heterodeposition 7
1.4.3 Accuracy of atomic model vs. accuracy of approach in search of plausible reaction pathway 8
1.4.4 Retaining the accuracy of kinetic Monte-Carlo 8
1.5 Generalizing the mechanistic interpretation of ALD 9

2 Micro-scale and macro-scale calculations **12**
2.1 Micro-scale calculations 12
2.1.1 Born and Oppenheimer approximation 12
2.1.2 Potential energy surface 13
2.1.3 Methodology of density functional theory 14
2.1.3.1 Introduction 14
2.1.3.2 Pseudopotential 17
2.1.3.3 Projector-augmented waves 17
2.1.4 Hierarchy of DFT functionals 18
2.1.4.1 Local (spin)-density approximation 19
2.1.4.2 Generalized gradient approximation 20
2.1.4.3 *Meta*-GGA 20
2.1.4.4 Hybrid functionals 21
2.1.5 Beyond density functional theory 22
2.1.5.1 Correcting on-site Coulomb repulsions DFT+U 22
2.1.5.2 Many-body perturbation theory-The GW approach 23
2.1.5.3 Van-der-Waals bonding 24
2.1.6 Generating slab models 24
2.1.7 Nudged elastic band 25
2.2 Macro-scale calculations 27
2.2.1 Introduction 27

2.2.2 Transition state theory 30
2.2.3 Time evolution 31
2.2.4 KMC solver 35

3 Multiple proton diffusion and film densification 36
3.1 Introduction 37
3.2 Computational details 38
3.3 End of H_2O pulse 40
3.4 Adsorption during Hf pulse 40
3.5 Proton diffusion (during either precursor pulse) 41
3.6 Elimination of ligands and densification 44
3.7 Start of H_2O pulse 51
3.8 Discussion of densification of $Hf(N(CH_3)_2)_4$ and H_2O molecules . 52
3.9 Summary 57

4 Cooperation effects in both metal and oxygen pulses 59
4.1 Introduction 59
4.2 Computational details 60
4.3 Cooperative effect in growth of Al_2O_3 from methyl precursors and H_2O molecules 62
4.4 Cooperative effect in growth of HfO_2 from amide precursors and H_2O molecules 66
4.5 Cooperative effect in growth of HfO_2 from halide precursors and H_2O molecules 68
4.6 Summary 73

5 Implementation of kinetic Monte-Carlo 74
5.1 Lattice site 74
5.2 Pulse time and purge time 76
5.3 Event type 76
5.4 Hf precursor adsorption 77
5.5 HfX_4 desorption 78
5.6 Proton diffusion 78
5.7 Rotation of the protonated ligand 80
5.8 Elimination of the ligand 80
5.9 Densification of HfX_2 81
5.10 Migration of HfX_2 81
5.11 Steric effect 83
5.12 H_2O adsorption 86
5.13 H_2O densification and ligand exchange 87

5.14 H_2O migration 88
5.15 H_2O decomposition 88
5.16 H_2O desorption 89
5.17 Neglected reactions 89
5.18 Summary 90

6 Results of kinetic Monte-Carlo simulations and discussion 91
6.1 Kinetics of reactions at the growing surface 91
6.1.1 Computational details and overview of growth 91
6.1.2 The metal precursor pulse 94
6.1.3 The purge 97
6.1.4 The oxygen precursor pulse 99
6.2 Simultaneous growth in different layers 101
6.3 Simulated atomic ratio from KMC 102
6.4 Calculated mass gain from KMC 104
6.5 Discussion and conclusion 105

7 Ongoing research and future studies 106
7.1 Accuracy of reaction pathways 106
7.2 Morphology and reaction condition 107
7.3 Advantages and disadvantages of KMC-derived data 107
7.4 Problems well suited to being addressed by KMC 108

A List of all ALD reactions included in KMC calculation 111

List of Tables

3.1 Diffusion barriers for protons in ALD and HfX_4 adsorption energies. E_a is activation energy and X = $N(CH_3)_2$. The 'dn' and 'up' indicate the position of proton on the nitrogen. surf-* means Hf precursor is anchored to * on the surface. 42

3.2 Activation energy for HX desorption from protonated HfX_4 and HfX_3 configurations i.e. probably Hf pulse. ΔG is free energy at $T = 500$ K and E_a is activation energy. X = $N(CH_3)_2$ and the 'dn' and 'up' show the position of proton on the nitrogen. 44

3.3 Reaction routes for HX dissociation after densification, and ligand exchange with oxygen, ΔG is free energy at $T = 500$ K and E_a is activation energy. 50

4.1 Reaction routes for proton transfer, ligand dissociation, and ligand exchange with oxygen, ΔE is energy difference and E_a is activation energy. X=CH_3 and $N(CH_3)_2$ for Al and Hf respectively. 63

A.1 This table contains reaction type α. 113

A.2 This table contains reaction type β. 114

A.3 This table contains reaction type γ. A1

I, Mahdi Shirazi, certify that this thesis is my own work and I have not obtained a degree in this university or elsewhere on the basis of the work submitted in this thesis.

Mahdi Shirazi

To my parents

Acknowledgements

Financial support from the Science Foundation Ireland (SFI)-funded strategic research cluster 'Functional Oxides and Related Materials for Electronics' (FORME), is gratefully acknowledged, www.tyndall.ie/forme. The authors also wish to acknowledge the SFI/HEA Irish Centre for High-End Computing (ICHEC) for the provision of computational facilities and support.

Abstract

High-permittivity ("high-k") dielectric materials are used in the transistor gate stack in integrated circuits. As the thickness of silicon oxide dielectric reduces below 2 nm with continued downscaling, the leakage current because of tunnelling increases, leading to high power consumption and reduced device reliability. Replacing the silicon oxide gate dielectric with a physically thicker high-k layer allows an increase in gate capacitance without the associated leakage current. Hence, research concentrates on finding materials with high dielectric constant that can be easily integrated into a manufacturing process and show the desired properties as a thin film. Atomic layer deposition (ALD) is used practically to deposit high-k materials like HfO_2, ZrO_2, and Al_2O_3 as gate oxides.

ALD is a technique for producing conformal layers of material with nanometer-scale thickness, used commercially in non-planar electronics and increasingly in other areas of science and technology. ALD is a type of chemical vapor deposition that depends on self-limiting surface chemistry. In ALD, gaseous precursors are allowed individually into the reactor chamber in alternating pulses. Between each pulse, inert gas is admitted to prevent gas phase reactions.

This thesis provides a profound understanding of the ALD of oxides such as HfO_2, showing how the chemistry affects the properties of the deposited film. Using multi-scale modelling of ALD, the kinetics of reactions at the growing surface is connected to experimental data. This allows the validity and accuracy of plausible reaction pathways to be examined. Extending ALD to new materials and new industrial processes will be assisted through such understanding.

The complete ALD growth mechanism is extremely complicated, as it consists of acid/base reactions, structural relaxation ("densification") and self-limiting surface chemistry, all of which are strongly influenced by factors such as steric hindrance. The common assumption about the ALD mechanism for metal oxides is that the dominant reaction is proton transfer to a ligand, followed rapidly by desorption of the protonated ligand. There has been discrepancy between theory and experiment, insofar as many proton transfer and ligand desorption reactions are computed to be energetically unfavorable, although the corresponding ALD process operates well in practice.

In this thesis, we use density functional theory (DFT) method to simulate more realistic models for the growth of HfO_2 from $Hf(N(CH_3)_2)_4/H_2O$ and $HfCl_4/H_2O$ and for Al_2O_3 from $Al(CH_3)_3/H_2O$. In DFT, the electron-electron interactions in many-electron systems are replaced with an effective one-electron potential, which is a functional of the electron density only. We obtain a detailed picture of the growth mechanism, including a resolution to the above contradic-

tion.

Three major breakthroughs are discovered. A new reaction pathway, 'multiple proton diffusion', is proposed for the growth of HfO_2 from $Hf(N(CH_3)_2)_4/H_2O$. This pathway describes the protonation of multiple ligands after precursor adsorption which leads to desorption of ligands and densification of the metal.

As a second major breakthrough, a 'cooperative' action between adsorbed precursors is shown to play an important role in ALD. By this we mean that previously-inert fragments can become reactive once sufficient molecules adsorb in their neighbourhood during either precursor pulse. Through the calculated activation energies and free energies of reaction, the cooperative mechanism is shown to have a profound effect on proton transfer and ligand desorption. Adsorbate molecules seem to 'catalyse' the reaction at adjacent sites. This resolves the above-mentioned contradiction between experiment and theory and accounts for the success of ALD at low temperatures. It also explains how reactions self-limit at the end of one ALD pulse, but become reactivated at the start of the next pulse. We anticipate that this study will be the starting point for more realistic ALD models.

As a third breakthrough, the ALD of HfO_2 from $Hf(N(CH_3)_2)_4$ and H_2O is implemented for the first time into 3D on-lattice kinetic Monte-Carlo (KMC) that includes densification and steric effects. In this integrated approach (DFT+KMC), retaining the accuracy of the atomistic model in the higher-scale model leads to remarkable breakthroughs in our understanding. The resulting atomistic model allows direct comparison with experimental techniques such as X-ray photoelectron spectroscopy and quartz crystal microbalance. All atomistic reaction pathways in DFT are implemented as reaction events on the lattice. This contains all steps, from the early stage of adsorption of each ALD precursor, kinetics of the surface protons, interaction between the remaining precursors (steric effect), influence of remaining fragments on adsorption sites (blocking), densification of each ALD precursor, migration of each precursor, and cooperation between the remaining precursors to adsorb H_2O (cooperative effect).

The essential chemistry of the ALD reactions depends on the local environment at the surface. The coordination number and a neighbour list are used to implement these dependencies. The validity and necessity of the proposed reaction pathways are statistically established at the mesoscale. The formation of one monolayer of precursor fragments is shown at the end of the metal pulse. The migration of the low coordinated remaining precursor fragments is also proposed. This process introduces a slow re-ordering motion ('crawling') at the mesoscale, leading to the smooth and conformal thin film that is characteristic of ALD.

Chapter 1

Introduction

1.1 Advantage of computer modelling

Simulation provides a bridge between theory and experiment, using the remarkable computational power available today in order to perform virtual experiments and examine the theories in complex systems. Validation of a model can be achieved if simulation shows agreement with experiment. It is better if a simulation can explain experimental data by supplying evidence for one model over another. Best of all is if a simulation can forecast, reduce the number of choices and lead to deep understanding without experimental input. Regardless of the balance between computed and measured data, computational studies can simplify the investigation of a novel process or reduce the amount of development time in the laboratory.

The aim of this thesis is to unravel the essential mechanisms behind ALD using an atomistic approach and understand each part of the derived mechanism in the context of the entire mechanism. In the future, the determined mechanisms can be applied to other ALD systems resulting in better design of ALD precursors.

1.2 Application of atomic layer deposition

ALD is a technique for producing conformal layers of nanometer scale thickness, used commercially in non-planar electronics and increasingly in other high-tech industries.[1–3] ALD is a variant of chemical vapour deposition (CVD) with slow growth rate, in which two or more gaseous precursors are allowed to flow separately into a reactor in alternate pulses. Inert gas is admitted between each pulse to purge the remaining precursor from the reactor and avoid gas phase reactions. Because of this, the precursors react with the substrate only. In the ideal case, ALD surface reactions are self-limiting, meaning that reactions cease after

the formation of one monolayer of precursor fragments at the end of the pulse. Growth of the product film therefore takes place at the level of a sub-monolayer in each cycle, conformally coating all exposed surfaces if the dose in each pulse is sufficient. The sequences of pulses and purges is followed until the desired thickness of film is obtained.

Thin film materials, with thicknesses of the order of 1-100 nm, have a wide variety of technological applications. ALD provides relatively accurate control of composition and good conformality over high-aspect-ratio structures.[4,5] It can be carried out at lower temperatures than other vacuum deposition techniques. Developing new ALD processes requires better understanding of how film growth depends on the chemicals being used.

Below we list some main applications of ALD in the electronics industry, ALD is used to deposit conformal layer high-K gate oxides, high-K memory capacitor dielectrics, ferroelectrics, and metals and nitrides for electrodes and interconnects.[6] The deposition control of ultra-thin film is the essential requirement in high-K oxides. In dynamic random access memories (DRAMs), even higher conformality is required and ALD is the only method that can be used when feature sizes become smaller than 100 nm. ALD is expected to come in to wider use at 45 nm technology.

Gate oxides: When the SiO_2 metal-oxide semiconductor field-effect transistor (MOSFET) is downscaled to a thickness of 1.0 nm, the tunnelling current through the SiO_2 increases and reduces the efficiency of the electronic device. Replacement of SiO_2 with a high-K oxide deposited by ALD was needed in order to improve the efficiency of the electronic device.

Research into the ALD of high-K gate oxides was mainly concentrated on three systems: $Al(CH_3)_3/H_2O$, $ZrCl_4/H_2O$ and $HfCl_4/H_2O$. These systems all provide good results, yielding metal oxide films in range of 1-2 nm. However, scaling the thickness down further is difficult and requires careful attention to the pretreatment of the silicon surface and design of the new precursors. Therefore alternative chemistry is being developed for the ALD of oxides (see section 1.3).

DRAM Capacitors: The development of DRAM capacitor dielectrics is similar to that of gate dielectrics. ALD is a very promising technique to achieve high conformal thin film required in DRAM application. DRAM trench capacitors are three dimensional in which conformal thin film with permittivity values above 200 is required. Therefore, the candidate materials are different from those used for MOSFET gate dielectrics. The most extensive studies candidates are $SrTiO_3$ and $BaTiO_3$. Growth of ternary and quaternary compounds is very demanding for chemical thin-film deposition methods. ALD chemistry was developed for $SrTiO_3$ and $BaTiO_3$ using strontium and barium cyclopentadienyl compounds,

and water as precursors.[7]

Transition-Metal Nitrides: TiN and TaN, transition-metal nitrides, are deposited as metallization barriers and as gate metals. A metallization barrier is required to avoid Cu diffusion into the surrounding insulators and silicon substrate. A metal gate electrode (rather than polysilicon) is required to eliminate any increase in equivalent oxide thickness-increasing due to depletion layer capacitance.[6] The ALD process for deposition of TiN from $TiCl_4/NH_3$ has been extensively studied. Films with low resistivity (< 200 $\mu\Omega$cm) and high conformality are achieved.[8] The process is not ideal because of the modest reactivity of ammonia, the halide residue content, the modest deposition rate and the fact that the byproduct HCl causes pitting of copper.[8] Many alternative titanium precursors have been studied but no ideal alternative solution has been found for the TiN process.[6]

ALD chemistry has been developed for TaN and WN_x materials, which are more challenging to deposit than TiN since they need stronger reduction. A three-precursor process ($TaCl_5/Zn/NH_3$) using Zn as reducing agent was employed to deposit TaN.[9] However, the use of zinc is not accepted in microelectronic fabrication and therefore alternative reducing agents like trimethylaluminum,[10] dimethylhydrazine,[11] and tert-butylamine[12] have been used to deposit TaN.

Plasma enhancement provides new possibilities for the ALD of TaN and other transition-metal nitrides. For instance, tert-butylimidotris(diethylamido)tantalum, $[(Et_2N)_3Ta{=}NtBu]$, and hydrogen radicals are used as precursors. The process has a good growth rate (0.8 Å/cycle) at low temperature (260 °C), but requires long hydrogen plasma exposure times (30 s).[13]

WN is an alternative barrier material, which has been deposited from WF_6 and NH_3 with a rate of 0.42 Å/cycle at 350 °C.[8] With longer exposure time, the same process resulted in a much higher deposition rate of 2.55 Å/cycle.[14] A new process using WF_6, NH_3 and $B(C_2H_5)_3$ has been developed for deposition of WC_xN_y (atomic composition: W 57% C 30%, N 13%).[15] 7 nm thin films of this material showed a resistivity of 600-900 $\mu\Omega$cm.

Metal films: Metal ALD has several motivations: (I) Cu seed layers for Cu electrodeposition and W seeds for W CVD, (II) Ti and Ta for Cu interconnect barriers, (III) noble metals for ferroelectric random access memory and DRAM capacitor electrodes, and (IV) high- and low-workfunction metals for dual-gate MOSFETs. Growth of metals is quite demanding by ALD. Utilizing metal CVD chemistry in ALD processes has been unsuccessful.

Deposition of copper has been reported to be quite problematic.[16] It was shown that a copper seed layer can be formed indirectly by deposition of a copper oxide film from $Cu(thd)_2/O_3$ (thd=2,2,6,6-tetramethyl-3,5-heptanedionate)

as precursors and then utilizing a reducing agent, like alcohols or aldehydes,[6] to reduce CuO to metallic copper. It has been shown that copper can be deposited from $Cu(acac)_2$ (acac=acetylacetonate) utilizing hydrogen radicals from plasma discharge.[6] The deposited films are quite rough. In another report, copper metal thin films were deposited from $Cu(dmap)_2/Et_2Zn$ at low temperature of 100-120 °C. In this ALD process, the surface reactions are found to be self-limiting and complementary enough to make a uniform, conformal, high-quality copper metal thin film.[17]

The noble metals Ru and Pt have been deposited from the organometallic precursors $Ru(C_5H_5)$ and $(CH_3C_5H_4)Pt(CH_3)_3$ and oxygen.[18] The essential mechanism is that oxygen atoms remain adsorbed on the Ru and Pt surface after the oxygen pulse and following purge. During the organometallic pulse, the oxygen atoms oxidize part of the hydrocarbon ligands and result in carbon dioxide and water. The remaining hydrocarbon fragments are oxidized during the next oxygen pulse, which creates the adsorbed oxygen-atom layer. The grown thin film is pure and shows resistivity of 10-20 $\mu\Omega$cm. This kind of ALD chemistry has been applied to many noble metals capable of catalyzing the dissociation of molecular oxygen.

However, the use of radicals has introduces new possibilities for metal ALD. Depositing electropositive elements, like titanium and tantalum, without increasing temperature in thermal ALD is apparently impossible. Using reactive hydrogen radicals generated in a remote plasma discharge, these materials have been deposited from the chloride precursors.[19] A reasonable growth rate, resistivity, and step coverage have been reported for these metal thin films. Aluminum has been deposited at low temperature with a growth rate of 1.5 Å/cycle by a hydrogen-plasma enhanced ALD process from trimethylaluminum.[20] Nickel films were also indirectly deposited by first making the oxide and then reducing that with hydrogen radicals.[21]

1.3 Motivation to study amide precursors

Hafnium oxide (HfO_2) shows a band gap of approximately 6 eV and a high dielectric constant in thin film form[22] of $k = 25$ which makes it an important high-k material. In the ongoing miniaturization of electronic devices, nanometre-thin films of hafnium oxide are replacing silicon oxide as the gate insulator in field effect transistors (section 1.2).[5] The hafnium oxide thin films are fabricated using ALD.[23]

In ALD of hafnium oxide, $HfCl_4$ and water are the most frequently used precursor combination.[24] However, a major difficulty with the $HfCl_4$ precursor

is chlorine contamination in the thin films. The contamination decreases with increasing substrate temperature. However higher temperature means a drop in coverage of reactive OH fragments as H_2O dissociates and consequently a drop in growth rate per cycle. Therefore an alternative precursor chemistry is required that exhibits suitable thermal stability, conformal ALD growth and low levels of impurities at low temperature.

Hafnium alkylamide precursors, like $Hf(NEtMe)_4$, $Hf(NEt_2)_4$ and $Hf(NMe_2)_4$ (Et = C_2H_5, Me=CH_3), are interesting alternatives together with water, leading to smooth and conformal thin films.[25] These precursors operate at relatively low temperature ($\sim$ 300 °C). While there is discussion about the stability of alkylamide precursors as a function of temperature, this is out of the scope of this study, where we consider only "ideal" ALD reactions.

In 2002, Hausmann *et al.*[25,26] used metal alkylamide precursors to grow metal oxides rather than the halide precursors that were commonly used in CVD reactors. In their studies, they monitored growth with the quartz crystal microbalance (QCM). QCM measures a change in mass per unit area as consequence of change in frequency of a quartz crystal resonator. As mass is deposited on the surface of the crystal, the frequency of oscillation decreases from the initial value. With considering some simplification, the change of frequency can be correlated to the change of mass down to a level of 1 $\mu g/cm^2$.

Karavaev *et al.*[27] recently used *in situ* X-ray photoelectron spectroscopy (XPS) to measure elemental composition. XPS is a surface chemistry analysis technique that measures elemental composition, chemical state and electronic state of the elements that exist within 10 nm of material from top of the surface. By irradiating a material with a beam of X-rays, an XPS spectrum is measured. XPS measures the kinetic energy and number of electrons that escape from the surface. A typical XPS spectrum shows the number of electrons detected versus binding energy. Each element generates a particular set of XPS peaks at particular binding energy values that indicates the existence of the particular element in the surface of the sample. The number of detected electrons in each peak is directly correlated to the amount of element within the area irradiated.

Lack of computational studies of alkylamide ALD chemistry motivates us to describe the plausible reaction pathways at low temperature. We carry out calculations of the $Hf(N(CH_3)_2)_4$ and H_2O precursors in chapter 3. Many plausible reaction pathways are discovered in this thesis that describe why alkylamide precursors operate well at low temperature. For such ideal ALD reactions, we expect that the three commonly-used amides listed above will behave similarly.

The growth of hafnium oxide from $HfCl_4$ and water on different substrates was studied theoretically before.[28,29] The effect of under-coordinated surface oxy-

gen and hydroxyl groups (as the active sites) on the hafnium of the adsorbing precursor was inspected and it was shown that the dissociation of HCl is facilitated via increasing the coordination number (c.n.) of hafnium during the water pulse.[30] The ALD reactions for elimination of HCl from $HfCl_4$ are computed to be endothermic[28,30] which is in sharp contrast to the success of this precursor in ALD experiments. In the cluster model the neglect of under-coordinated atoms[29] might cause this discrepancy, while in the slab model the neglected change in entropy[30] might be the cause. Therefore, in the current study of metal alkylamide precursors, we consider both the change in entropy and the influence of under-coordinated atoms and find exothermic reactions, which resolves the discrepancy between experiment and theory. Here we should emphasize that some aspects of the reaction pathways for amides are different from those of halides. The amide is more bulky and more reactive toward a hydroxylated surface than the chloride. The amide ligands are more Brønsted basic than chloride ligands. The films deposited by metal alkylamide precursors show a high degree of conformality and low level of impurities.[25,31]

1.4 Computational studies of atomic layer deposition

The ALD process occurs across many length scales.[32,33] The alternate flow of gases into metre-scale reactors, around millimeter-scaled geometries, results in chemical reactions between atoms, which grow into nanometre thin films and coat micron-scaled pores. It is unlikely to be possible to describe explicitly all of these length scale in one model. The most plausible approach that has come to mind so far is the multi-scale approach. A successful multi-scale approach combines the selected length scale approaches to minimize the errors from one scale to another.[34] The problem of timescale in ALD is perhaps even more difficult than that of length scale. While a combination of fast (ps-ns) and slow reactions (μs-ms) influence the film growth rate, gases are pulsed and purged over second-long timescales.

1.4.1 Multiscale modelling of atomic layer deposition

Multiscale modelling has a broad definition in engineering, mathematics, physics, chemistry and computer science. In multiscale modelling, material properties and system behavior are modelled on each level using information from the other levels. The following levels are most common in computational material science: (I) level of quantum mechanics includes electron interactions between clamped nuclei, (II) level of molecular dynamics includes the thermal motion of individ-

ual atoms, (III) mesoscale or nano level includes groups of atoms and molecules, (IV) macroscale includes bulk-like elements objects. Mesoscopic and macroscopic objects both contain a large number of atoms. However, macroscale modeling describes the average properties derived from its constituent materials, and they usually obey the laws of classical mechanics. In contrast, mesoscale model investigates the fluctuations around the average that is subject to quantum mechanics. Each level describes phenomena over a specific frame of length and time.

This study particularly concentrates on the application of multiscale modelling to ALD. This allows one to predict properties of materials grown by ALD based on knowledge at the atomistic level. In this thesis, we will not discuss macroscale modelling (*e.g.* fluid flow, reactor-scale). We will particularly focus on two size scales.
(I) Electronic structure scale: Schrödinger equation is solved in theoretical framework of density functional theory (DFT).
(II) Nanoscale: The formulation of an on-lattice kinetic Monte Carlo (KMC) to describe growth over multiple ALD cycles.

1.4.2 Atomistic approach in homodeposition and heterodeposition

Most recent computational studies of ALD are motivated by the needs of the electronic industry, particularly the ALD of high-permittivity ('high-k') dielectrics onto semiconductors as part of the gate stack in CMOS transistors. The two largest sections of the computational work in the literature cover the ALD of high-k oxides, both the reaction mechanisms themselves and how deposition onto semiconductor substrates occurs. The first is used to refer to the constant growth rate that is obtained over cycles of product-on-product growth. This refers to 'homodeposition' which is the main objective of this thesis. The second is the deposition of subnanometre thin films onto a substrate, which is termed 'heterodeposition' to separate it from the steady-state 'homodeposition'. This thesis only includes simulation of the ALD process itself and not of heterodeposition or of properties of the materials deposited by ALD.

Atomistic calculations, which are discussed in next chapter, are now recognized as important complement to experiment. The electronic structure describes a system by approximately solving the Schrödinger equation, which provides the wavefunction, energy gradient, etc. The more accurate the approach, the more computationally demanding and the fewer atoms can be simulated. The various approaches of atomistic simulation have been developed during last the 4 decades form a hierarchy of accuracy versus cost and system size.

1.4.3 Accuracy of atomic model vs. accuracy of approach in search of plausible reaction pathway

It is commonly expressed that ALD is controlled by kinetics, rather than thermodynamics, presumably due to the irreversible loss of by-products into the stream of exhaust gases. However, certain reaction steps are reversible and thermodynamically controlled, such as the sampling of surface sites by frequently adsorbing/desorbing precursor molecules. The kinetic competition between the ALD reactions is important for successful ALD and therefore much of the interest of atomistic simulations is on the activation energies for such reaction steps.

Calculating the activation energy still remains a difficult task in atomistic simulations. Such bond-making-breaking is a sensible calculation in ab initio methods (*e.g.* DFT)) and the system size remains under 1000 atoms on today's computer power. Nevertheless, error cancellation is poor when the wavefunction changes strongly at the transition state, so the reliable chemical accuracy can only be obtained by post-Hf approaches like coupled cluster singles and doubles (CCSD)[35] or configuration interaction[36] possible for fewer than 100 atoms.

There is an inevitable compromise between the accuracy of the quantum mechanical solution and the veracity of the atomic model. The latter describes the number of atoms, the number of possible geometries and how many possible pathways can be examined. This means that reasonably large selection of atoms is as crucial as accuracy when computing activation energy. For instance, if the model consists of just one H and one ligand, then the number of possible pathways for proton diffusion is unrealistically low relative to actual ligands on an OH-covered surface.

In chapter 4, we add more complexity to this subject by considering the consequence of adsorbate-adsorbate on the H-transfer pathway. It will be shown that the sampling of phase space of a system is more important than the accuracy of the quantum mechanical solution. Hence, even though DFT underestimates the activation energy, it still is preferred to post-Hartree Fock methods which are too computationally demanding. This breakthrough has been demonstrated for alkylamide, alkyl, and halide precursors and is speculated to be valid for all other ALD processes that operate well in practice. We can also speculate that adsorbate-adsorbate interactions are equally important in related processes like heterogeneous catalysis or non-pulsed CVD.

1.4.4 Retaining the accuracy of kinetic Monte-Carlo

To describe the complete ALD growth mechanism is extremely complicated, as it consists of acid/base reactions, structural relaxation 'densification' and self-

limiting surface chemistry, all of which are strongly influenced by factors such as steric hindrance. For such a complex system with many competing reaction pathways, the reaction rates and pathways can be used as input into a stochastic simulation method such as KMC[37–39] and a direct simulation of how the system advances through its possible events can be achieved. In the KMC approach, time is coarse-grained, and advances in irregular jumps from one reaction event to the next. The timescale of seconds required for ALD pulse and purge can therefore be simulated. The most common implementation of KMC calculation is lattice based where events occur on a fixed lattice of cells in space. The crystalline lattice of the material is often chosen as the simulation lattice.

In most multi-scale modelling, the overall aim is to establish a coupling between atomistic calculation (*e.g.* DFT) and another approach (*e.g.* KMC) to achieve an upward trend in scales while retaining the accuracy of lower scales. In KMC calculation, the activation energies are used as input. However, the error in DFT activation energies is not consistent across different class of reactions and hence, the trends and relative values may not be accurate. For this reason, many KMC strategies adjust activation energies so as to fit measurements.[40] However, in this thesis the activation energies and reaction pathways are discovered exclusively from DFT calculation. The use of plausible pathways from DFT and implementation of the discovered pathways into KMC in this study represent a substantial advance in the state-of-art. Using this approach (DFT+KMC), the probability of a certain DFT-derived reaction pathway in the context of all the other pathways will be examinable by KMC. In a few cases, a plausible reaction pathway may be proposed during KMC that can then be examined by DFT.

Potential outputs from KMC calculation can validate the proposed reaction pathways, the amount of film deposited and gaseous by-product (in terms of moles, mass and thickness), the distribution of remaining precursors, the stoichiometry and morphology of the grown film. All these predictions can be compared with experiment. In the chapter 3, DFT+KMC outputs are compared with experimental data (QCM, XPS).

1.5 Generalizing the mechanistic interpretation of ALD

ALD process development obviously depends on deep understanding-first of the homodeposition mechanism, and after that, the mechanism of deposition onto various substrates. The aim of chapter 3 and 4 is to identify the elementary chemical reactions that transform precursor molecules into product film. Of course, in

reality these chemistries consist of both ALD and non-ALD growth reaction, as well as those reactions that cause impurities. The knowledge of the elementary chemical reactions provides predictions of growth rate, temperature dependence, optimum pulse/purge duration and morphology of the as-grown film. It may also help in designing precursors for new thin film materials.

In ideal ALD, it is supposed that precursors react only on the growing surface and not in gas-phase. Elliott[34] described the film growth reactions for element M as:

$$\text{gas}-\text{ML}_\text{n} \rightleftharpoons \text{surf}-(\text{ML}_\text{n}) \rightleftharpoons \text{surf}-(\text{ML}_\text{x}) \rightleftharpoons \text{bulk}-\text{M} \tag{1.1}$$

where ML_n is a single precursor molecule with n ligands L and x is the remaining ligands ($0 \leq \text{x} \leq \text{n}$). However, in this study a generalized version of Eq. 1.1 is proposed considering adsorbate-adsorbate interaction on the growing surface obtained from DFT calculations:

$$\text{gas}-\text{s}(\text{ML}_\text{n}) \rightleftharpoons \text{surf}-\text{s}(\text{ML}_\text{n}) \rightleftharpoons \text{surf}-\text{s}(\text{ML}_\text{x}) \rightleftharpoons \text{bulk}-(\text{M}_\text{s}) \tag{1.2}$$

where s is an integer that quantifies the number of neighbouring adsorbates that influence each other on the surface, and 'bulk-M_s' refers to the atoms in crystalline thin-films. The position of the equilibrium between the steps in Eq. 1.2 depends on the reaction energetics, activation energies, reaction conditions and on the availability of reagents during the pulse-purge cycle of ALD. In chapter 4, it will be shown that the activation energies of ALD change as a consequence of adsorbate-adsorbate interaction at the surface.

The initial step in Eq. 1.2 is molecular adsorption. Many unsuccessful ALD processes cease here due to poor adsorption or low population of adsorption sites at surface. The second step is ligand desorption. Reaction conditions identify the experimental details relating to how transformation of gaseous precursor to bulk-like material is carried out in laboratory settings. The reaction conditions, such as temperature, pressure and time, influence the number of desorbed ligands and consequently the plausible reaction pathways. A change of the plausible reaction pathways results in a different growth rate and different morphology of the grown film. In the scenario of Eq. 1.2, the number of adsorbates neighbouring a fragment have essential effects on its desorption of ligands. In the last step, bulk-like atoms are produced. The final bulk-like state may not be reached until after several ALD cycles due to poor co-adsorption of the alternate precursor. To summarize: describing the overall ALD chemistry means describing each of the steps in Eq. 1.2, particularly considering the interactions between ML_x adsorbates

on the substrate or growing surface.

Chapter 2

Micro-scale and macro-scale calculations

2.1 Micro-scale calculations

During the last 4 decades, computer simulation based on quantum-mechanical description have been improved significantly. This progress provides better understanding in theoretical physics and chemistry and enables us to contribute significantly to materials design for future technology. This development in micro-scale calculation is built on two columns: (I) The improved description of electronic structure of many-body systems within DFT and the forthcoming post-DFT approaches; (II) The implementation of many-body approaches into efficient and versatile computer code.

In this section, we will describe the approaches that are used in the next chapters to extract the necessary data for macroscale calculations or will be used in prospect of ALD simulation. We will discuss the implementation of various DFT functionals [local-density approximation (LDA), generalized gradient approximation (GGA), meta-GGA, hybrid functional mixing DFT, and exact (Hartree-Fock) exchange] and post-DFT approaches [DFT+U, many body perturbation theory (GW), van-der-Waals] and optimization tool [slab modelling and nudged elastic band (NEB)]. These are all implemented in the Vienna ab initio simulation package (VASP).[41,42] VASP is a plane-wave all electron code using the projector-augmented wave approach[43] to describe the electron-core interaction.

2.1.1 Born and Oppenheimer approximation

In quantum mechanics, the computation of the energy and the wavefunction of a system is a difficult task. To alleviate this complexity and solve time independent Schrödinger equation, Born and Oppenheimer in 1927 proposed to compute the

energy and wavefunction in two less complicated sequences. In this approach termed as Born and Oppenheimer (BO) approximation, the wavefunction of a system is broken into its electronic and nuclear components.

$$\Psi_{\text{total}} = \Psi_{\text{electronic}} \times \Psi_{\text{nuclear}} \tag{2.1}$$

In the first step of the BO approximation, the electronic Schrödinger equation is solved. This provides the wavefunction $\Psi_{\text{electronic}}$ which depends on electrons only. During the first step the nuclei are fixed in a certain configuration, very often the equilibrium configuration. The electronic energy is composed of the nuclear potential, electron kinetic energy, electron-electron interaction and electron-nuclear attractions. In the BO approximation, the inertia of electrons considered to be negligible in comparison to the atom to which they are bound. In the second step of the BO approximation this function serves as a potential in a Schrödinger equation containing only the nuclear potential energy of the system.

The BO approximation is successful due to the high mass ratio of nucleus/electron. The approximation is an essential assumption in quantum chemistry; without it only the lightest molecule, H_2, could be handled. All computations of wavefunctions for molecular chemistry and condensed matter physics make use of it. Even in the cases where the BO approximation breaks down, it is used as a start point for the computations.

2.1.2 Potential energy surface

Within the Born-Oppenheimer approximation in quantum mechanics and statistical mechanics a potential energy surface is generally utilized to model chemical reactions and interactions in simple chemical and physical systems. The "surface" name refers to the fact that the total energy of an atom arrangement can be represented as multidimensional surface, with atomic positions as variables. The best imagination would be to think of a landscape that the height of the land shows the energy associated with given values in length and width.

A simple description of the very simplest chemical systems can be provided by a simple potential energy surface. However, to model a real chemical reaction, a potential energy surface must be created to consider every possible orientation of the reactant and product molecules and the electronic energy of each of these orientations. Typically, the electronic energy is provided for each of tens of thousands of possible orientations, and these energy values are then fitted numerically to a multidimensional function. The accuracy of these points depends upon the level of theory used to calculate them.

Once the potential energy surface has been achieved, many points of interest must be determined. Perhaps the most important is the global minimum for the energy value. This global minimum, which can be found numerically, corresponds to the most stable nuclear configuration. Other interesting features are the reaction coordinate (the path along the potential energy surface that the atoms "travel" during the chemical reaction), saddle points or local maxima along this coordinate (which correspond to transition states), and local minima along this coordinate (which correspond to reactive intermediates).

In chapter 4, the number of adsorbates in ALD system will be changed to improve description of a dynamical system. Hence, computing a larger system goes further towards satisfying the thermodynamics of ALD and the resulting reaction pathway, saddle point and reactive intermediates are better representations of experimental reality.

2.1.3 Methodology of density functional theory

2.1.3.1 Introduction

The non-relativistic Hamiltonian for a many-electron system is presented (in atomic units $\hbar$=m=e=1) by

$$H = \sum_{\mathrm{i}}[-\frac{1}{2}\nabla^2(r_{\mathrm{i}}) + V(r_{\mathrm{i}})] + \frac{1}{2}\sum_{\mathrm{i}\neq\mathrm{j}}\frac{1}{\mid r_{\mathrm{i}} - r_{\mathrm{j}} \mid} \tag{2.2}$$

where V is a local external potential such as the field from the nuclei. The Coulomb interaction of the last term makes the Schrödinger equation difficult to solve. For a small system, such as an atom or a small molecule, it is possible to accurately determine the many-particle ground-state wavefunction using the configuration interaction approach[36] or coupled cluster (CCSD) approach.[35] In those approaches, the wavefunction is expanded as a sum of Slater determinants[44] whose orbitals and coefficients are determined by minimizing the total energy. However, the computational effort scales exponentially with the system size so that application to large molecules or solids is not possible. For excited states, the computational effort becomes extremely large even for small systems. In practice, we attempt to find quantities that do not require the full knowledge of the wavefunctions (*e.g.* the total energy).

Approximate theories are usually concentrated on finding a good single-particle approximation that simplifies the Coulomb term. The earliest of these theories is the Hartree approximation (1928) where the non-local Coulomb term is replaced with an average local Coulomb potential (Hartree potential) for all the electrons. In spite of the fact that it produces reasonable results, because of

a cancellation between exchange and correlation, the Hartree theory is not accurate enough in many cases.[45] An extension of the Hartree theory which takes into account the fermionic nature of the electrons leads to the Hartree-Fock (HF) approximation (Fock 1930). In this regime, in addition to the average local Coulomb potential there is a non-local exchange potential which represents the Pauli exclusion principle. In reality the HF approximation performs well for atoms, but for insulating solids the electronic energy gap is in most cases too large. The reason for this can be reflected back to the neglect of correlations or screening, which is not too important in atoms but crucial in solids. HF already takes into account to a large extent correlation between electrons of the same spin, since the Pauli exclusion principle (exchange) stops them getting close together. Two electrons of opposite spin on the other hand are allowed to occupy the same single-particle state at the cost of a large Coulomb energy. Correlations keep electrons away from each other, creating a screening hole around each electron, which decreases the interaction with the other electrons and similarly the Coulomb energy. The energy cost of transferring an electron from one site to a neighbouring site is substantially reduced by screening. Thus, correlation or screening reduces the gap from its Hartree-Fock value. In metals, the absence of correlation in the HF approximation causes qualitatively wrong results.

To simulate the effect of correlation, Slater introduced the X_α method where the exchange potential is modelled by a local potential of the form $V^{\mathrm{x}} = \alpha n^{\frac{1}{3}}$, derived from the electron gas and scaled by a constant α to simulate correlation. n is the local electron density.[44,46] This approach has been quite successful in calculating ground-state properties and excitation spectra but it is semiempirical. The X_α theory may be considered as a precursor of modern DFT (Hohenberg and Kohn 1964,[47] Kohn and Sham 1965[48]), which has become a standard method for calculating ground-state properties of molecules and solids. In DFT, the ground-state energy can be shown to be a functional of the ground-state density and satisfies the variational principle with respect to the density. The explicit form of the functional in terms of the density is not known and such an explicit functional may not exist. Using the variational property of the energy functional, one arrives at a set of single-particle equations, the Kohn-Sham (KS) equations (Kohn and Sham 1965), to be solved self-consistently:

$$[-\frac{1}{2}\nabla^2 + V^{\mathrm{H}} + V^{\mathrm{XC}}]\phi_{\mathrm{i}} = \varepsilon_{\mathrm{i}}\phi_{\mathrm{i}} \tag{2.3}$$

$$n = \sum_{\mathrm{i}}^{\mathrm{occ}} \mid \phi_{\mathrm{i}} \mid^2 \tag{2.4}$$

where V^H and V^{XC} are the Hartree and exchange-correlation potential re-

spectively. The KS eigenvalues ε_i have no clear physical meaning except for the highest occupied which corresponds to the ionization energy (Almbladh *et al.*[49]).

To solve the many-electron Schrödinger equation (the KS equations) a hierarchy of approximate functionals has been developed. Exchange-correlation functionals are designed to satisfy as many exact constraints as possible.[50,51] These constraints are known from many-body theory. Parameters are nonempirical in the sense that they are determined by these constraints. Nonempirical functionals that achieve a sufficient number of constraints are most likely transferable and perform equally well in different systems. In the search for better density functionals, different communities in quantum chemistry and in condensed matter physics have developed different functionals.

In the quantum chemistry community, the atomic one- and two-electron densities in atoms and molecules are reproduced. In addition, to increase the accuracy, a number of empirical parameters are often considered in a functional. An excellent example is provided by the B3LYP functional[52,53] which is the most popular functional in quantum chemistry. This functional maintains a total of eight empirical parameters, which allow to achieve a very high accuracy for almost all properties of a small molecule. The resulting semiempirical approximation may be very accurate within systems that are similar to the fitting data sets while often failing when applied to different situations.

The advance of electronic structure theory of solids was improved by an excellent paper published in 1985 by Car and Parrinello.[54] They suggested to solve the equation of motion of the coupled multi-atom, multi-electron system using a dynamical simulated annealing strategy. The Car-Parrinello (CP) method replaced the traditional approach of iterative self-consistent solution of the KS equations for the electrons. The forces acting on the atoms are calculated via the Hellmann-Feynman[55]theorem, and the dynamics are obtained by integration of the Newtonian equations of motions of the ions and electrons. This procedure should be repeated after each ionic integration step until the ground state of the many-electron system and many-atom had been achieved. The CP paper introduced several other important new concepts. The first innovation was the use of fast Fourier transforms to switch between real-space and momentum space representations. The kinetic energy has a diagonal representation in momentum space while the potential energy is diagonal in real space. Therefore, different parts of the calculation can be done most efficiently in one space or the other. The second innovation as a milestone in solving KS equations was based on the observation that is deficient to do one part of the calculation with very high accuracy while the other part (the determination of the equilibrium ionic configuration) is still far away from convergence. Hence, the total energy of a system could be mini-

mized at the same time with respect to both the electronic and ionic degrees of freedom.

Modern DFT calculations are specified by several technical choices:

(I) The choice of a basis set to expand the KS eigenfunctions. Essentially the choice is between plane waves and localized basis functions.
(II) The interactions between nuclei and core electrons and the valence electrons can be described either by a full-potential approach or by a pseudopotential eliminating the need to account for the complex nodal character of the valence orbitals.
(III) The approach adopted for the determination of the eigenstates of the KS Hamiltonian.
(IV) The description of the electron-electron interaction via functionals proposed within DFT.

In those cases where DFT alone does not provide an adequate solution (*e.g.* strong electronic correlations, excited eigenstates) post-DFT corrections such as many-body perturbation theory[45,56] or dynamical mean field theory[57,58] may be used to improve the DFT predictions.

2.1.3.2 Pseudopotential

Pseudopotentials have been introduced to remove the need for an explicit treatment of the strongly bound and chemically inert core electrons. This is a necessary requirement to reduce the computational effort of plane-wave methods or local-basis set methods. The theory of pseudopotentials is well-developed. However, constructing reliable, transferable, and efficient pseudopotentials is not a trivial task. Conserving the norm of the wavefunction and ultrasoft pseudopotential are two principles for treating core electrons. The norm-conservation is applied to node-less pseudo-wavefunctions. This maintains the logarithmic derivative of the exact and pseudo-wavefunction and their derivatives with respect to the energy at the chosen reference energy and cut-off radius. The ultrasoft pseudopotential is used once the norm-conservation criterion is dropped. Valence wavefunction oscillates rapidly near ion cores. This situation is problematic because it needs many Fourier component to describe the wavefunctions accurately. To overcome this difficulty the projector-augmented wave method was proposed.

2.1.3.3 Projector-augmented waves

The projector-augmented wave (PAW) method originally proposed by Blochl[43] provides an attempt to obtain simultaneously the computational efficiency of

the pseudopotential method and the accuracy of the full-potential linearized augmented-plane-wave method. The PAW approach handles above problem by transforming these rapidly oscillating wavefunction into smooth wavefunctions which are more computationally efficient. The linear transformation operator $\mathcal{T}$ transforms the fictitious pseudo wavefunction $|\tilde{\Psi}\rangle$ to the all-electron wavefunction $|\Psi\rangle$:

$$|\Psi\rangle = \mathcal{T}|\tilde{\Psi}\rangle. \tag{2.5}$$

The all-electron wavefunction is a KS single particle wavefunction. $|\tilde{\Psi}\rangle$ and $|\Psi\rangle$ differ only in the regions near the ion cores, we can write

$$\mathcal{T} = 1 + \sum_R \hat{\mathcal{T}}_R \tag{2.6}$$

where $\hat{\mathcal{T}}_R$ is non-zero only within some spherical augmentation region Ω_R surrounding atom R. Around each atom, it is useful to expand the pseudo wavefunction into pseudo partial waves:

$$|\tilde{\Psi}\rangle = \sum_i c_i |\tilde{\phi}_i\rangle. \tag{2.7}$$

The operator $\mathcal{T}$ in Eq. 2.7 is linear, the coefficients c_i therefore can be shown as an inner product with a set of so-called projector functions, $|p_i\rangle$:

$$c_i = \langle p_i|\tilde{\Psi}\rangle \tag{2.8}$$

where $\langle p_i|\tilde{\phi}_j\rangle = \delta_{ij}$. The all-electron partial waves, $|\phi_i\rangle = \mathcal{T}|\tilde{\phi}_i\rangle$, are typically chosen to be solutions to the Kohn-Sham equation for an isolated atom. The transformation $\mathcal{T}$ is therefore specified by three sets:
(I) a set of all-electron partial waves $|\phi_i\rangle$
(II) a set of pseudo partial waves $|\tilde{\phi}_i\rangle$
(III) a set of projector functions $|p_i\rangle$.

Outside the augmentation regions in regions between the PAW spheres surrounding the atoms, the pseudo partial waves are identical to the all-electron partial waves. Inside the spheres, they can be any smooth continuation, such as a linear combination of polynomials or Bessel functions.

2.1.4 Hierarchy of DFT functionals

In order to improve the results from DFT calculations, more accurate exchange-correlation functionals are developed. A ladder of approaches of increasing accuracy for the exchange-correlation energy as a functional of the electron density is

proposed which is sometimes referred to as the 'Jacob's ladder' of DFT.[59] At the lowest rung of this ladder, the contribution to the energy from a volume element of 3-dimensional space is determined by the local density there. Higher rungs or levels incorporate increasingly complex ingredients constructed from the density or the KS orbitals in or around this volume element. The four important rungs on Jacob's ladder accessible so far are (I) the local density approximation (LDA);[60] (II) the generalized gradient approximation (GGA);[61] (III) the *meta*-GGA[62,63] introducing in addition a dependence on the Laplacian of the electron density, and (IV) hybrid functionals mixing DFT and exact (Hartree-Fock) exchange.[64,65] We describe which additional exact conditions can be satisfied at each level, and discuss the extent to which the functionals at each level may be constructed without empirical input.

2.1.4.1 Local (spin)-density approximation

The LDA is a class of approximations to the exchange-correlation energy functional in DFT that depends solely upon the value of the electronic density at each point in space (and not, for example, derivatives of the density or the KS orbitals). Many approaches can obtain local approximations to the exchange-correlation energy. However, the successful local approximations are those that have been derived from the homogeneous electron gas (HEG) model.[66] In this regard, LDA is generally synonymous with functionals based on the HEG approximation, which are then applied to realistic systems (molecules and solids).

$$E_{\mathrm{XC}}^{\mathrm{LDA}} = \int \varepsilon_{\mathrm{XC}}(n) n(\vec{r}) d^3r \tag{2.9}$$

The local spin-density approximation[67] (LSDA) is a straightforward generalization of the LDA to include electron spin:

$$E_{\mathrm{XC}}^{\mathrm{LDA}}[n\downarrow, n\uparrow] = \int \varepsilon_{\mathrm{XC}}(n\downarrow, n\uparrow) n(\vec{r}) d^3r. \tag{2.10}$$

Highly accurate formulae for the exchange-correlation energy density $\varepsilon_{\mathrm{XC}}(n_\uparrow, n_\downarrow)$ have been constructed from quantum Monte Carlo simulations of the HEG model. It is well known that the LDA tends to overestimate the bond strength in solids, the calculated lattice constants are too small, cohesive (binding) energies are overestimated, and energy gaps in semiconductors and insulators are generally underestimated.

2.1.4.2 Generalized gradient approximation

The generalized gradient approximation (GGA) introduces a dependence of the exchange-correlation functional on the local gradient $\vec{\nabla}n(\vec{r})$ of the electron density. For the exchange energy, the GGA has the form

$$E_{\mathrm{XC}}^{\mathrm{GGA}}[n\downarrow, n\uparrow] = \int \varepsilon_{\mathrm{XC}}(n\downarrow, n\uparrow, \vec{\nabla}n\downarrow, \vec{\nabla}n\uparrow)n(\vec{r})d^3r \tag{2.11}$$

Many functionals have been constructed. The Perdew-Wang (PW91) functional[61] has been constructed using QMC data for the uniform electron gas and exact properties of the exchange-correlation hole. The Perdew-Burke-Ernzerhof (PBE) functional[51] presented a more elegant derivation of the functional using exact properties of the exchange-correlation energy. A GGA functional designed to include surface effects was developed by Armiento and Mattson[68] (AM05). A revised PBE density-functional that improves predictions of equilibrium properties of solids (PBEsol) was recently proposed by Perdew *et al.*[69] The GGA corrects the overbinding tendency inherent in the LDA, although with a certain tendency to overcorrect. The LDA functionals underestimate lattice constants by about 1%. The PBE functional overestimates them by nearly the same amount. Other equilibrium properties such as bulk moduli, phonon frequencies, and magnetic moments, which are sensitive to the lattice constant, are overestimated by the GGA.[70] However, it should be pointed out that the GGA renders the correct ground state for magnetic transition metals where the LSDA fails quite badly.[71] In the LSDA, Fe is predicted to be hexagonal close-packed and nonmagnetic instead of body-centered cubic and ferromagnetic.[71] For surface energies, the LSDA predictions are too low, but even lower values are produced in the GGA.[72] For the adsorption energies of small molecules on solid surfaces, however, the lower values predicted by GGA are definitely superior to the LSDA results.[73]

In a few cases, LDA calculations yield better agreement with experiments than calculations using the GGA. Examples are layered crystals such as graphite or molecular crystals where binding between atomic layers or between molecules is based on van der Waals interaction only. In such cases, interlayer or intermolecular distances are in better agreement with experiment if the LDA has been used. However, it has to be pointed out that this is a mere artefact due to the overbinding inherent in the LDA and not a proper description of the physical binding mechanism.

2.1.4.3 *Meta*-GGA

The meta-GGA is a straightforward extension of the concept underlying the GGA.[62,63] In addition to the dependence on the local density $n(\vec{r})$ and its gradi-

ent $\nabla n(\vec{r})$, the meta-GGA functional depends also either on the Laplacian of the electron density $\Delta n(\vec{r})$ or on the local kinetic energy density $\tau(\vec{r})$ defined as

$$\tau(\vec{r}) = \frac{1}{2}\sum_{\mathrm{k}=1}^{\mathrm{N}} |\nabla\psi_{\mathrm{k}}(\vec{r})|^2, \tag{2.12}$$

where the summation extends over all occupied KS eigenstates. Meta-GGA functionals using the kinetic energy density $\tau(\vec{r})$ depend explicitly on the orbitals. Again, the many meta-GGA functionals proposed in the literature may be divided into semi-empirical parametrized functionals and functionals following the philosophy of the PBE-GGA and attempting to eliminate adjustable parameters as far as possible. An example is the PKZB functional proposed by Perdew *et al.*. An improved form of the meta-GGA has been proposed by Tao *et al.* (TPSS).[74] Molecular tests proved a substantial improvement of atomization energies, while for lattice constants and bulk moduli of solids the performance of the PKZB and TPSS meta-GGA's is essentially on par with the PBE results. For small molecules, the meta-GGA leads to significant improvements of the atomization energies, but for solids the results are more ambiguous.[74]

2.1.4.4 Hybrid functionals

Hybrid functionals are described by mixing nonlocal Fock exchange and local or semilocal DFT exchange in a certain proportion. The exact exchange energy functional is expressed in terms of the KS orbitals rather than the density, so is termed an implicit density functional. The construction of hybrid functionals is motivated by the fact that the deficiencies of DFT and HF are in some sense complementary. Band gaps predicted by DFT are too narrow, gaps calculated using HF are far too wide.[64,65] Hence there is some hope that mixed functionals may not only predict more accurate gaps, but also lead to more accurate total energies and geometries. The most popular hybrid is the three-parameter B3LYP functional mixing 80% of LDA with 20% of HF exchange (adding a certain amount of Beck's correction, $\Delta E_{\mathrm{X}}^{\mathrm{B88}}$), and mixing in the correlation part 19% of the Vosko-Wilk-Nusair[75] (VWN) functionals with 81% of Lee-Yang-Parr[76] correlation (note that these exchange and correlation functionals in turn contain some empirical parameters),

$$E_{\mathrm{XC}}^{\mathrm{B3LYP}} = 0.8E_{\mathrm{X}}^{\mathrm{LDA}} + 0.2E_{\mathrm{X}}^{\mathrm{HF}} + 0.72\Delta E_{\mathrm{X}}^{\mathrm{B88}} + 0.19E_{\mathrm{C}}^{\mathrm{VWN}} + 0.81E_{\mathrm{C}}^{\mathrm{LYP}}. \tag{2.13}$$

Another attempt to reduce the degree of empiricism has been made with the PBE0 and HSE03 functionals. The PBE0 functional[75] mixes $\frac{1}{4}$ of exact (HF)

exchange with $\frac{3}{4}$ of PBE exchange, and describes correlation in the GGA (PBE),

$$E_{\mathrm{XC}}^{\mathrm{PBE0}} = 0.25E_{\mathrm{X}}^{\mathrm{HF}} + 0.75E_{\mathrm{X}}^{\mathrm{PBE}} + E_{\mathrm{C}}^{\mathrm{PBE}}, \tag{2.14}$$

For molecular systems, the improvement achieved with the PBE0 functional is well documented,[77] and it can be attributed to the fact that an admixture of a certain part of exact reduces the self-interaction error of DFT.[78]

2.1.5 Beyond density functional theory

Even after climbing to the highest rung of 'Jacob's ladder',[59] DFT does not solve all problems. Examples are strongly correlated materials (d- and f- electron systems with narrow bands), excited states in semiconductors and insulators, and dispersion forces in rare-gas solids or molecular crystals. In all these cases, it is necessary to go beyond DFT.

2.1.5.1 Correcting on-site Coulomb repulsions DFT+U

In DFT, the orbital-dependence of the exchange correlation energy is rather weak. In many cases, this is appropriate, but in systems with narrow 3d- or 4f-bands and localized orbitals, DFT fails to account for the strong Coulomb repulsion between electrons occupying these narrow bands, which leads to enhanced exchange splitting between occupied and empty eigenstates. The DFT+U method attempts to cure this defect by adding a Hubbard-type Coulomb repulsion to the DFT Hamiltonian. Many versions of DFT+U have been presented in the literature. The implementation in VASP is based on the work of Dudarev[79] and Liechtenstein,[80] using the spin-dependent on-site density matrix $\rho_{\mathrm{ij}}^{\sigma}$ to define the DFT+U energy functional as

$$E_{\mathrm{DFT+U}} = E_{\mathrm{DFT}} + \frac{U-J}{2}\sum_{\sigma} Tr[\rho^{\sigma} - \rho^{\sigma}\rho^{\sigma}], \tag{2.15}$$

where the Hubbard parameter[42] $U = E(d_{\mathrm{n+1}}) + E(d_{\mathrm{n\text{-}1}}) - E(d_{\mathrm{n}})$, measures the increase in energy caused by placing an additional electron into a particular site, and J is a screened Stoner-like exchange parameter. Note that in this formulation the Hubbard-like part of the Hamiltonian is rotationally invariant. The one-electron potential is given by the variational derivative of the total energy with respect to the density,

$$V_{\mathrm{ij}}^{\sigma} = \frac{\delta E_{\mathrm{DFT+U}}}{\delta \rho_{\mathrm{ij}}^{\sigma}} = \frac{\delta E_{\mathrm{DFT}}}{\delta \rho_{\mathrm{ij}}^{\sigma}} + (U-J)[\frac{1}{2}\delta_{\mathrm{ij}} - \rho_{\mathrm{ij}}^{\sigma}], \tag{2.16}$$

i.e., relative to the DFT eigenvalues the energies of occupied states are lowered

by -*(U-J)*/2 and increased by *(U-J)*/2 for unoccupied states. If the density matrices are idempotent, $(\rho^\sigma)^2 = \rho^\sigma$, i.e. for a completely empty or a full band, the energy is given by the DFT alone. The DFT+U capability of VASP has been applied to transition-metal sulphides,[81] transition-metal oxides[82] and to f-electron systems.[83] The DFT+U is a semi-empirical approach, because the Hubbard parameter U is an adjustable parameter. However, it has been shown that if the Hubbard correction is applied to spin-polarized GGA calculations, good agreement for lattice parameters, magnetic moments, band gap and exchange splitting can be achieved with a single value of U for each element. If, as often reported in the literature, the DFT+U is applied on the basis on non-spinpolarized LDA or GGA results, a much larger value of U is required to reproduce the experimentally observed exchange splitting, spoiling the agreement for the lattice parameters and other volume-dependent quantities.[42] To some extent, the DFT+U approach has been superseded by hybrid-functional calculations. However, it has still the advantage of a much lower computational effort.

2.1.5.2 Many-body perturbation theory-The GW approach

The accurate calculation of excitation spectra (i.e. of quasiparticle energies) is a long-standing problem of solid-state theory. That DFT fails to correctly predict excited state energies is not surprising, since there is no formal justification to interpret DFT eigenvalues for unoccupied states as quasiparticle energies. A widely used approach to calculating quasiparticle energies and the spectral function is the GW approach.[45,56] Within the GW method, the quasiparticle energies $E^{\mathrm{QP}}_{n\vec{k}}$ are the solutions of the following set of nonlinear equations

$$(T + V_{\mathrm{ne}} + V_{\mathrm{H}} - E^{\mathrm{QP}}_{n\vec{k}})\Psi_{n\vec{k}}(\vec{r}) + \int d^3r' \sum(\vec{r}, \vec{r}', E^{\mathrm{QP}}_{n\vec{k}})\Psi_{n\vec{k}}(\vec{r'}) = 0 \tag{2.17}$$

where T is the kinetic energy operator, V_{ne} the potential due to the nuclei, V_H the Hartree potential and $\sum$ is the self-energy operator given by

$$\sum(\vec{r}, \vec{r}', \omega) = \frac{i}{4\pi} \int_{-\infty}^{\infty} e^{i\omega'\delta} G(\vec{r}, \vec{r}', \omega + \omega') W(\vec{r}, \vec{r}', \omega') d\omega' \tag{2.18}$$

where G is the Green's function, and W is the screened Coulomb interaction of the electrons. The GW method includes many-body effects in the electron-electron interaction and goes beyond the mean-field approximation for independent particles. This is achieved via the dynamical screening of the exchange operator with the frequency-dependent dielectric matrix of the system.

2.1.5.3 Van-der-Waals bonding

The van-der-Waals force is the sum of attractive or repulsive forces between molecules (intermolecule or intra-molecule) other than those due to the covalent bond, the hydrogen bond, or electrostatic interaction of ions with one another with neutral molecule or charged molecule. A correct description of van-der-Waals interactions requires a treatment of dynamic long-range correlation effects. The van-der-Waals force includes: (I) force between two permanent dipoles (Kessom force) (II) force between a permanent dipole and a corresponding induced dipoles (Debye force) (III) force between two instantaneously induced dipoles (London force).

London forces are showed by non-polar molecules due to correlated movement of the electrons in interacting molecules. The electrons in neighbouring molecules "flee" as they repel each other, electron density is redistributed in proximity to another molecule. This redistribution of electron density results in the formation of instantaneous dipoles that attract each other. The larger the molecule is, the London forces become stronger. Due to the increase of polarizability of molecule, more dispersed electron clouds will be obtained.

Dispersion-corrected DFT include functionals that are a mix true of conventional and an add-on energy terms. For instance, B3LYP-D shows a functional with the usual B3LYP functional plus a D dispersion correction energy term. The dispersion correction energy term is a simple function of interatomic distances and contains adjustable parameters that are fitted to conformational and interaction energies calculated by CCSD.[35] DFT-D and DFT-D2 energy corrections include all pairs of atoms while DFT-D3 also consider triplets of atoms to account for three-body effects.

2.1.6 Generating slab models

One of the challenges in any simulation is generating a realistic model to describe the properties of interest. How to model a surface is described in this section. The surface can be created through the cleavage of bulk (supercell) parallel to (h k l) plane. The stability of a surface is quantified using the surface energy. Surface energy is the disruption of inter-atomic forces occurring when a surface is created. In solid state physics, surface is less energetically favorable than a bulk of a material. In first principle (FP) calculation, surface energy of a crystalline solid, such as metals or metal oxides, can be achieved through below equation:

$$E_{\text{surface}}^{\text{n-layers}} = \lim_{n \to +\infty} \frac{E_{\text{n}} - k \cdot E_{\text{bulk}}}{2A} \tag{2.19}$$

Where E_{n} stands for different number of layers in direction of [h k l] (slab). E_{bulk} is the computed bulk energy per unit cell and k is number of repetitive unit cell in a direction (h k l) normal to the surface. Clearly, for a slab with two identical faces, the total area is twice the area of the primitive surface unit A.

The cleaved surface can be polar or non-polar. In latter case, the planar surface is favoured because it minimizes the surface energy leading to convergence of surface energy. In the case of polar surface, care is needed when cleaving the crystal. Generation of polar surfaces parallel to (h k l) leads to inadvertent divergence of surface energy. An unrelaxed polar surface is particularly unstable, leading to release the massive electrostatic energy and reconstruction of cleaved surface.

The surface reconstruction occurs due to reordering of the forces at the terminated surface along a given plane. The reconstructed surface shows the lower symmetry than the cell of bulk termination. FP calculation has unique capacity to evaluate the stability of reconstructed surface and building an (n $\times$ m) cell that can be compared with experimental data.

2.1.7 Nudged elastic band

A common and important problem in theoretical chemistry and condensed matter physics is the identification of a lowest energy path for a rearrangement of a group of atoms from one stable configuration to another. Such a path is often called the 'minimum energy path' (MEP). It is utilized to define a 'reaction coordinate' for transitions, such as chemical reactions. The potential energy maximum along the MEP is the saddle point energy which describes the activation energy or barrier. The saddle point energy is a quantity of central importance for estimating the transition rate within harmonic transition state theory[84,85](hTST).

Since crystalline atoms are usually tightly packed and typical temperature of interest is relatively low (comparing with the melting temperature) hTST can typically be used in studies of diffusion and reactions in crystals or at crystal surface. This simplifies the problem of simulating the rates. The search for the optimum transition state then converts to a search for the lowest few saddle points at the edge of the potential energy basin of the initial state. The rate constant for transition through the region around each of the saddle points can then be derived from the energy and frequency of normal modes at the saddle point and the initial state. The most difficult part in this approach is the search for the saddle points.[86,87]

Many different approaches have been introduced for finding reaction pathways and saddle points.[88] Some of the approaches start at the local minimum on the

potential energy surface representing the initial state and then trace a series of distinct points and check for a saddle point. However, these methods do not necessarily yield saddle points. In other approaches, both initial and final minima for the transition are typically given. Since a first order saddle point is a maximum in one direction and a minimum in all other directions, approaches for finding saddle points always include some kind of maximization of one degree of freedom and minimization in other degrees of freedom.

The path joining the initial and final states that particularly has the greatest statistical weight is the MEP. At any point along the path, the force on the atoms is simply pointing along the path. The maximum is the saddle point on the MEP. A potential energy surface may have many saddle points. The length between two points along the MEP is a natural option for a reaction coordinate. This is given by the normal mode eigenvector which corresponds to negative curvature at the saddle point.

Nudged elastic band (NEB) is an efficient approach to search the MEP between a given initial and final minima of a transition.[89–91] It has been widely used for calculating the activation energy within the hTST approximation. The approach has been performed in combination with electronic structure calculations, in particular plane wave based DFT calculation. The MEP is found by building a set of images (replicas) of a system, typically of the order of 4-20, between the initial and final state. A spring interaction is applied between neighbouring images to maintain continuity of the path, thus resembling an elastic band. An optimization of the band, including the minimization of the force acting on each of the images, drags the band to the MEP.

A special feature of the NEB method, distinguishing it from other elastic band approaches, is force projection. This prevents the spring forces interfering with the convergence of the elastic band to the MEP and prevents that the true force does affect the distribution of images along the MEP. In order to decompose the true force and the spring force into components parallel and perpendicular to the path, the tangent to the path at each image and every iteration should be predicted during the minimization. Only the perpendicular component of the true force and the parallel component of the spring force are considered. This force projection is referred to as 'nudging'. The spring forces then only determine the distance of the images along the band. When this projection scheme is not used, the elastic band is too firm and the path may cut a corner and hence miss the saddle point region. In this situation, the spring forces tend to prevent the band from following a curved MEP (because of 'corner-cutting').[92] If a smaller spring constant is used k=0.1 then the true force along the path causes the images to move smoothly away from the high energy regions towards the minima, thereby

reducing the density of images where they are most needed (the 'sliding-down' problem).[92] In the NEB method, there is no such competition between the true forces and the spring forces. The spring constant can be varied by a few orders of magnitude without affecting the equilibrium position of the band.

An elastic band with $N+1$ images can be defined by $[R_0, R_1, R_2, ..., R_N]$, where the end points, R_0 and R_N, are fixed and given by the energy minima of to the initial and final states. The $N-1$ intermediate images are adjusted by an optimization algorithm; we have utilized the conjugate-gradient algorithm.[93] In the NEB approach, the total force acting on an image is the sum of the spring force along the local tangent and the true force perpendicular to the local tangent

$$F_{\mathrm{i}} = F_{\mathrm{i}}^{\mathrm{s}} \mid_{\parallel} -\nabla E(R_{\mathrm{i}}) \mid_{\perp}, \tag{2.20}$$

where the true force is given by

$$\nabla E(R_{\mathrm{i}}) \mid_{\perp} = \nabla E(R_{\mathrm{i}}) - \nabla E(R_{\mathrm{i}}).\tau_{\mathrm{i}}, \tag{2.21}$$

Here, E is the electronic energy of the system, at R_{i}, the atomic coordinates for image i, and τ_{i} is the normalized local tangent at image i. The spring force is

$$F_{\mathrm{i}}^{\mathrm{s}} \mid_{\parallel} = k(\mid R_{\mathrm{i+1}} - R_{\mathrm{i}} \mid - \mid R_{\mathrm{i}} - R_{\mathrm{i\text{-}1}} \mid)\tau_{\mathrm{i}}, \tag{2.22}$$

where k is NEB the spring constant. An optimization algorithm is then used to move the images according to the force in Eq. 2.20. The images converge to the MEP with equal spacing if the spring constant is the same for all the springs.

2.2 Macro-scale calculations

2.2.1 Introduction

Modelling a complete ALD process requires integration of three modelling scales: a model for the reactive flow of the vapour-phase species on the scale of the whole reactor and within microscopic features,[94] a model for the evolution of the atomic structure at the growth surface and a model for the reaction kinetics in both the vapor and at the surface. The overall ALD growth dynamics across all three scales is too complicated to be fully modelled. This section describes the reaction kinetics and structural relaxation at the growing surface, ignoring fluid dynamics and pressure fluctuations at either the feature or reactor scale. The information used in this model is obtained from an electronic structure model (chapter 3).[95] Before we describe our model in detail, we will briefly survey the existing literature on similar ALD models.

A simple analytical model based on the mass balance of chemisorption, can be used to relate the growth rate to the size of the reactant and the chemisorption events.[96,97] Steric hindrance of the ligands controls the saturation of chemisorption at the adsorption sites. This model can be used for various ALD systems[3] if the mechanism is known. While it can estimate growth rates, it does not give insights into the fundamental surface chemistry or predict properties such as the morphology of the film.

Another approach is to perform all-atom molecular dynamics (MD) simulations using an empirical inter-atomic potential. This technique has been used to model the growth of amorphous Al_2O_3 from $Al(CH_3)_3$ and H_2O.[98] Experimental results[99] show that ALD using this system is possible at low temperatures and therefore, a relatively low activation energy for the gaseous by-product methane is expected. Hence, MD simulation of short duration ($< 1\mu$s) applying inter-atomic potentials seem to be a well-suited approach to describing the structural relaxation during ALD growth. However, using MD simulations is unsuitable for ALD systems whose primary reactions fall into the category of rare events.[38] Also, experimentally measured O/Al ratios vary between 1.34 to 1.70 depending on growth temperature.[99] In this situation, due to the process of densification, which is a driving force for the ALD reactions (chapter 3),[95] the Al atoms should exist at higher coordination numbers (i.e. c.n. $= 5$ or 6) than the calculated value (c.n. $= 3$ or 4). Therefore, a denser film than that actually obtained would be expected and the inter-atomic potential does not adequately describe the structural relaxation taking place during ALD growth.

Another approach is KMC,[100] a powerful method for describing the stochastic time evolution of inter-dependent events. KMC is used in a wide range of areas from chemistry to biology. In KMC modelling, the true dynamical information (atomic positions and momenta) is dismissed and the atomic trajectories are replaced by a set of discrete positions, chosen from a set of pre-determined possible atomic sites. KMC is ideally suited for modelling reaction events in surface science, involving adsorption, desorption, cooperative reaction, and structural relaxation at the surface of the growing film.[37,101] The method can reach simulation times of orders of magnitude longer than atomistic MD, while preserving a level of atomic detail. KMC can accommodate events at different time scales, including rare events. There are many KMC approaches, from coarse-grained model systems with hypothetical input values, to realistic atomic simulation with accurate chemical kinetics for the making and breaking of bonds. In the latter, a proper evaluation of surface kinetics at the mesoscopic scale is possible by using accurate information from first principles electronic-structure calculations.

Neizvestny et al.[40] used KMC as a coarse-grained model to simulate the ALD

process. To reproduce the experimental situation, hypothetical activation energies were used. However, the KMC approach that we follow here is to carry the accuracy of electronic structure calculation theories over to the mesoscopic scale. Along these lines a ground-breaking KMC model for ALD was proposed by Dkhissi et al.[102] that made use of ALD reactions and activation energies from DFT calculations. They used a complicated lattice-based KMC to describe the growth of HfO_2 from $HfCl_4$ and H_2O on Si. A lattice framework was used to describe the transition between silicon crystal substrate and the oxide thin film. However, the complexity of the densification process on the growing surface was not implemented, insofar as changes in Hf and O c.n. from the gas to solid phase[95] and associated structural relaxation was not considered. The steric demand of the precursor fragments was only partially accounted for.

As a general rule, an accurate description of a system by KMC requires a complete set of reaction pathways because the absence of an important reaction pathway results in a poor description. As will be shown in this study, the absence of cooperation between the remaining ligands to adsorb H_2O molecules[95] (which we term the cooperative effect, chapter 3, chapter 4) results in overestimation of the growth rate. In this study, multiple proton diffusion, steric effects, structural relaxation, and cooperative effects are included for the first time in ALD growth simulation and the necessity of including these in the mesoscale chemistry is justified.

Another major concern with the input data to the model is the accuracy of activation energies, which affects the growth rate and time evolution. The chemistry presented here has been obtained by ab initio calculations using DFT (chapter 3). There is a systematic error due to the approximate DFT exchange-correlation functional that often results in underestimated activation energies for breaking and making bonds (subsection 2.1.3). This can, in principle, be overcome by using more accurate methods[35,36] rather than DFT. However, owing to the complicated reaction pathways that result from cooperative effects, computing large cells with many atoms (*e.g.* 500 atoms) is necessary, which is too computationally demanding for the more accurate methods. Hence, at the present time we rely on the activation energies calculated using DFT. If all activation energies are underestimated, then the time taken to saturation during ALD will be too short, but the sequence of reactions will be correct.

The chemical reactions that can occur at a given site depend not only on the chemical identity of that site but also on the spatial environment - both local bonding to adjacent atoms (described via the c.n.) and steric effects due to more distant species. Hence, to implement the surface chemistry discussed, a lattice-based KMC is used and the spatial environment is described through

the c.n. and a neighbour list. Clearly, a lattice-based KMC does not explain the morphology of the film during ALD (*e.g.* crystalline vs amorphous). In this study, we present only on-lattice KMC. However, the morphology of the film as a function of temperature could be studied by off-lattice KMC.[103] This means that the reported ALD reactions and their activation energies could be used for future off-lattice studies.

In the next section, some background of KMC simulations is described. However, the main part of this study is explaining how DFT-derived reaction pathways are implemented into lattice-KMC (chapter 5). Evaluating how that played out as surface intermediates and growth behaviour is presented in chapter 6.

2.2.2 Transition state theory

The common approach to modelling chemical kinetics is transition-state theory (TST). In TST, the rate constant for the transition from a minimum A to a minimum B is estimated from the equilibrium flux crossing a dividing surface separating the two minima. The dividing surface is the hyperplane perpendicular to the reaction coordinate and the transition state (TS) is where the two intersect. Here, there are two assumptions. First, it is supposed that the system has reached thermal equilibrium between A and TS. Secondly, it is assumed that successful transitions through the dividing surface from A to B are uncorrelated, meaning that each forward transition through the dividing surface moves the system from A to B. For these assumptions to be valid, the best choice of dividing surface is near the saddle point in the minimum energy path between A and B, where the entire equilibrium flux is minimized. If thermal motion around the saddle point and the minima can be described by second-order expansions (harmonic vibrational modes) then the transition between the two minima can be explained by harmonic TST (hTST). From these assumptions, the rate constant k_{AB} for the transition from minimum A to minimum B can be derived from the Markovian[39] state-to-state dynamics equation:

$$k_{\mathrm{AB}}^{\mathrm{TST}}(T) = A \exp(E_{\mathrm{a}}/k_{\mathrm{B}}T) \tag{2.23}$$

where E_{a} is activation energy and the prefactor is determined from

$$A = f_{\mathrm{AB}}^{\mathrm{TST}}(T)(k_{\mathrm{B}}T/h) \tag{2.24}$$

where h is Planck's constant, k_{B} is the Boltzmann constant, T is temperature and

$$f_{\mathrm{AB}}^{\mathrm{TST}}(T) = (q_{\mathrm{TS}}^{\mathrm{vib}}/q_{\mathrm{A}}^{\mathrm{vib}}) \tag{2.25}$$

where $q_{\mathrm{TS}}^{\mathrm{vib}}$ and $q_{\mathrm{A}}^{\mathrm{vib}}$ are the vibrational partition functions at the TS and at the bound state A respectively.

Thus, in order to evaluate $k_{\mathrm{AB}}^{\mathrm{TST}}$, static information about the potential energy surface (PES) at the initial minimum A and at the TS and the partition functions at those locations are typically required. In most cases involving surface-bound reactants and products, the vibrational properties of the system at the minimum and TS are found to be similar,[37] so we consider the ratio $f_{\mathrm{AB}}^{\mathrm{TST}}(T)$ ∼1 in Eq. 2.25. However, gas-surface reactions include large changes in entropy and so this assumption does not apply. The prefactor A has values of the order of 10^{12} s^{-1} to 10^{13} s^{-1} depending on temperature.

In hTST, the key information from the PES which is entered into Eq. 2.23 is E_{a}, the potential energy of the TS relative to the (meta)stable initial minimum. In ALD, many transition states correspond to situations where bonds are made or broken. E_{a} for such situations can be obtained from ab initio quantum chemistry models. These models, in the Born-Oppenheimer approximation, treat electrons adiabatically at every configuration of atomic positions and atomic dynamics take place on the resulting PES (subsection 2.1.2).

However, hTST certainly cannot be used for the adsorption process (A = gas-phase, B = adsorbate on surface). Adsorption of the precursor takes place with a probability given by Maxwell-Boltzmann statistics. The molecular flux or impingement rate to the adsorption sites is obtained from

$$k_{\mathrm{n,B}}^{\mathrm{ads}}(T, P_{\mathrm{n}}) = \frac{S_{\mathrm{n,B}}(T) P_{\mathrm{n}} A_{\mathrm{uc}}}{\sqrt{2\pi m_{\mathrm{n}} k_{\mathrm{B}} T}} \tag{2.26}$$

where $S_{\mathrm{n,B}}(T)$ is the sticking coefficient that quantifies the fraction of molecules that stick to an adsorption site. For simplicity it was assumed that $S_{\mathrm{n,B}} = 1$ based on calculations of adsorption (section 3.4). P_{n} and m_{n} are the partial pressure and the mass of precursor molecules respectively. A_{uc} is the area of the surface unit-cell including site B and n is a label for the different precursors.[37,104]

2.2.3 Time evolution

A KMC simulation consists of a sequence of separate hops from one minimum to another (known as 'events') taking place at sites within the simulation cell. The random choice of which event at which location after which amount of time is governed by the probabilities of the events that are inputted to KMC. Starting

from a given minimum, the KMC algorithm determines which minimum to hop to and the appropriate time step Δt therefore changes at each KMC iteration. The system clock is advanced by this time:

$$t = t + \Delta t \tag{2.27}$$

Each pathway therefore has its own probability (Poisson) distribution function for time evolution. The probability of event m consisting of hopping from minimum i to minimum j at a given site is given by Eq. 2.28:

$$p_{\mathrm{m}}(\Delta t) = k_{\mathrm{ij}} exp(-k_{\mathrm{ij}}\Delta t) \tag{2.28}$$

The system has many possible events each with a fixed probability that is obtained its rate constant k_{ij} using Eq. 2.23. To advance the dynamics of the system in time, many numerical KMC algorithms have been suggested in the literature.[105] The first-reaction method[106] employs Eq. 2.29 to determine the timestep for each possible event.

$$\Delta t_{\mathrm{m}} = \frac{ln(\rho_{\mathrm{m}})}{k_{\mathrm{m}}} \tag{2.29}$$

where m = 1...N (total possible events). This algorithm has been used in other approaches to ALD modelling.[102,107] A random number $\rho_{\mathrm{m}} \in]0, 1]$ for each of the N possible events is generated, so that the timesteps are properly weighted by the rate constants. The pathway with the shortest timestep is chosen and executed. The system moves to the new state (minimum), and the system clock is advanced by the corresponding shortest timestep. In this algorithm, many random numbers must be generated, all of which are discarded apart from one.

Another commonly used algorithm was proposed by Bortz, Kalos and Lebowitz (BKL)[39] and is also referred as the Gillespie, rejection KMC, N-fold way, or residence-time algorithm (Fig. 2.1). This is the approach followed here. Initially, the BKL algorithm as with any KMC algorithm, begins by finding all N possible pathways across all the sites in the simulation cell. The corresponding N different rate constants are obtained using Eq. 2.23. The algorithm accumulates all the possible events together with their associated rates into an event list. Then the total rate constant is obtained by summing all the individual rate constants:

$$k_{\mathrm{tot}} = \sum_{\mathrm{m}=1}^{N} k_{\mathrm{m}} \tag{2.30}$$

Then, in contrast to the first-reaction method, only two random numbers ρ_1 and $\rho_2 \in]0, 1]$ are generated. When N is large, generating and processing two random numbers instead of N random numbers makes a large computational

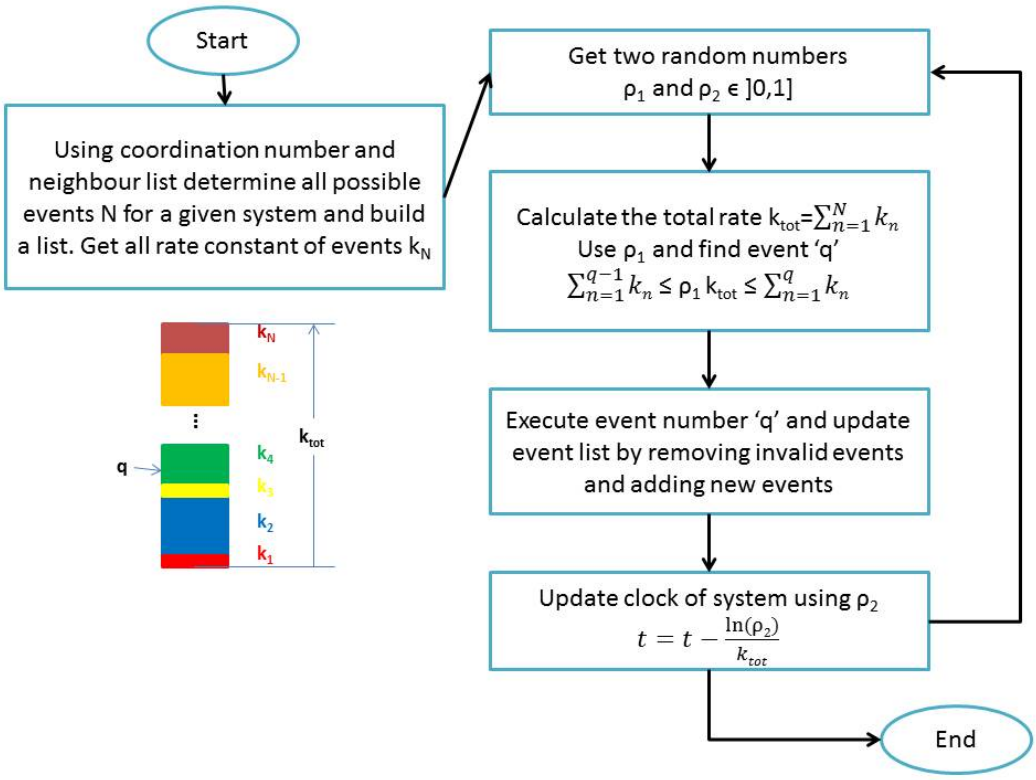


Figure 2.1: Flow chart describes the basic steps in the N-fold way BKL algorithm. The loop starts with the determination of all possible events (and their rate constants). Coordination number and neighbour list are used to accumulate all possible ALD reactions into the event list. Two random numbers are generated. The system is advanced corresponding to the process selected by the first random number. After execution of the selected event, the event list is updated locally rather than globally to avoid re-initialization of all possible events in each iteration. The system clock also progresses according to the computed total rate constant and the second random number, as prescribed by an ensemble of Poisson processes. The simulation continues until a sufficiently long time span has been covered.

difference. Hence, the first-reaction method is not as computationally efficient as the BKL method. ρ_1 is used to select one of the possible events via Eq. 2.31. Obviously, an event with a large rate constant is more likely to occur. Therefore the algorithm searches for the event q in the event list that fulfils Eq. 2.31 and the event q is executed.

$$\sum_{\mathrm{m=1}}^{\mathrm{q\text{-}1}} k_{\mathrm{m}} \leq \rho_1 k_{\mathrm{tot}} \leq \sum_{\mathrm{m=1}}^{\mathrm{q}} k_{\mathrm{m}} \tag{2.31}$$

An update of the event list is needed after each execution of an event. Even if the system includes thousands of potential events, typically only a few events are removed and a few events are added (in the order of one digit) to the event list after each execution. It is most efficient to preserve the event list and simply

modify the executed event and affected events in the vicinity of that site. Therefore, re-initialization of all possible events in each iteration is not required (Fig. 2.1), an enormous computational saving. In fact, updates of the event list have a much higher impact on the computational cost than generating the random numbers. In this respect, the first reaction method and BKL algorithm perform similarly well.

The other important aspect of the BKL algorithm is the time step and how the system clock is advanced. By executing the chosen event, the system moves to the new state and the system clock is advanced by the equation below:

$$t = t - \frac{ln(\rho_2)}{k_{\text{tot}}} \tag{2.32}$$

where ρ_2 is the second random number. The time evolution is independent of the chosen event, but does depend on the total sum k_{tot}. This means that when high rate events (fast processes) become dominant - not only in terms of weight but also in terms of number - the simulation advances extremely slowly. Such disparity between low and high rate events occurs when the system is trapped in a set of adjacent minima (a 'superbasin'). In this situation, a more advanced model[108] is needed that reduces the occurrence of frequent events. Our KMC model is also faced with the problem of this disparity (see section 5.6).

Some of the events observed during ab initio MD are highly exothermic and barrierless or have a small barrier (less than 0.2 eV) and so may be thought of as deterministic, rather than stochastic. To implement these processes in the stochastic model, a small barrier (0.2 eV) is assigned to each of the deterministic processes. The definition of a small barrier can be problematic because it can create a disparity in the rate of reactions and disturb the time evolution of the system. However, the reverse of these deterministic process is extremely rare and therefore the reverse reaction is omitted from our event list.

A larger system typically means more events. More events in the total event list means that the sum k_{tot} in the BKL approach becomes larger, even though the same reaction list is used. Hence, the system clock progresses slower for a large system than for small one, which is physically correct. However, in order to achieve a realistic cycle time for an ALD process with a reasonable computational time, some fast processes are ignored.

The system size and the fast processes therefore largely dictate the progress of the simulation time. In order to tackle a realistic ALD system, many reactions have to be included (see chapter 5).

2.2.4 KMC solver

The ALD application was developed as a new feature in the stochastic parallel particle kinetic simulator (SPPARKS)[109,110] code. SPPARKS is written in a modular fashion, allowing new functionality to be added in a straightforward manner. All possible events are specified before the simulation begins. The event list consists of all possible events at each site. rKMC is chosen as the KMC solver for choosing an event from the event list. This KMC solver uses the previously defined BKL-algorithm[39] to update the system clock by Eq. 2.32. The solver executes the chosen event and modifies the occupation of sites. The event list is updated by removing events that have become invalid at modified sites and adding new events for these sites to the event list.

Chapter 3

Multiple proton diffusion and film densification

The scope of this chapter is to provide the results of microscale calculations which have been simulated by DFT. To investigate the ALD reactions for growth of HfO_2 from $Hf(N(CH_3)_2)_4$ (TDMAHf) and H_2O, a DFT slab model was employed (subsection 2.1.6). We inspected all steps, from the early stage of adsorption of each ALD precursor to the densification of multiple atoms into bulk-like HfO_2 layers. The first section of this chapter is devoted to the study of the reaction mechanisms of ALD of HfO_2 from $Hf(N(CH_3)_2)_4$ and H_2O precursors as isolated adsorbates on the surface. In the next chapter 4, we will discuss the cooperation between adjacent adsorbates in either the metal pulse or the oxygen pulse. The data of this chapter will be inputted into kinetic simulations for a quantitative view of the complex film growth process in chapter 5.

The activation energy calculations show that repeated proton diffusion from the surface to amide ligands and rotation of the protonated amine is more energetically accessible than the simple elimination of the amine in the initial stage. We therefore propose that multiple protons diffuse to the amide ligands of the Hf precursor before desorption of protonated ligands takes place. Loss of a proton from surface oxygen frees it up for bonding to Hf of the precursor. Protonation of ligands, and especially desorption of ligands, frees up Hf for bonding to surface oxygen. These effects are termed 'densification', as they bring Hf−O packing closer to the bulk scenario. Densification is associated with substantial release of energy. During the metal pulse, saturation of the surface by remaining fragments HfX (X=$N(CH_3)_2$) causes adsorption of further metal precursor to stop. The presence of these fragments prevents further chemisorption of HfX_4, since this requires the creation of a strong dative bond between Hf and O. Next, during the H_2O pulse, Hf exchanges its remaining ligands with OH groups. The exchange occurs due to the decomposition of adsorbed H_2O molecules in clusters of HfX.

Decomposition of H_2O when adsorbed onto a (HfX_y) (y≥2) cluster (*e.g.* dimers) also increases the coordination of Hf and O. Simultaneously, low-coordinated oxygen atoms appear at the surface, which are reactive sites for the next metal pulse. With saturation of the surface by OH groups, H_2O molecules begin to appear. This detailed description of ALD chemistry allows us to make qualitative predictions about how the process depends on temperature.

3.1 Introduction

The intention of our work in this section is to elucidate the mechanism of hafnium oxide ALD, by obtaining quantitative information on the energetics ΔE, ΔG and E_a of reactions between adsorbate structures during both the $Hf(N(CH_3)_2)_4$ pulse and the water pulse. We use DFT to compute the reaction energetics of $Hf(N(CH_3)_2)_4$ adsorption, amide group dissociation and proton diffusion on a fully hydroxylated hafnium oxide surface. We also compute the reactions during the H_2O pulse, such as the interaction of H_2O with fragments of $Hf(N(CH_3)_2)_4$ precursor, explaining how the water molecule obtains higher coordination and becomes densified at the surface. The model thus describes chemical reactions throughout the ALD process, from the early stage of the $Hf(N(CH_3)_2)_4$ precursor with the substrate to obtaining bulk-like hafnium oxide at the end of the water pulse.

Calculations using a periodic slab are carried out on a HfO_2 surface subjected to $Hf(N(CH_3)_2)_4$ and other precursors and H_2O pulses. In this model, the acid-base reactions of precursor adsorption and by-product elimination are described. The effect of bridging O, bare O and OH as adsorption sites are considered. Under-coordinated oxygen are expected to have an important role during densification of precursor fragments. Densification is defined as the increase in density due to improved Hf−O packing, associated with an increase in coordination numbers of Hf and O from their molecular values (4 and 2 respectively) towards bulk solid values (7 and 4).[111] Moreover, H-transfer from sites adjacent to the adsorbed precursor is considered so as to see how those transfers change the reaction path in ALD.

It is clear that OH groups play an important role in growth reactions in oxide ALD, whether the co-reagent is H_2O or O_3 (protons are produced during oxidation of organic fragments in the latter case[3]). Different types of proton diffusion are inspected, to investigate whether multiple proton diffusion can facilitate dissociation of the fragment. We find that the way protons are diffusing between the surface and the adsorbed complex, as well as within the complex, reveals why low temperature ALD works in this case.

3.2 Computational details

To model the growth reactions of HfO_2 from HfX_4 (X = $N(CH_3)_2$) and H_2O, self consistent DFT was employed[112] (subsection 2.1.3). The reaction energies, activation energies and ab initio molecular dynamics (MD) of the system were calculated in a 3D periodic model utilizing VASP.[41] In these calculations, the electronic energies were approximated using the PAW[113] description of atomic cores (subsection 2.1.3.3) and the functional of PBE[51] (subsection 2.1.4.2). The plane wave cutoff energy was 400 eV.[114] For Hf atoms $5\,d^2 6\,s^2$, N atoms $2\,s^2 2\,p^3$, O atoms $2\,s^2 2\,p^4$, and C atoms $2\,s^2 2\,p^2$ electrons were included as valence electrons. All calculations were closed shell since no unpaired electrons are expected in these calculations. The self-consistent steps were converged to an energy difference of 10^{-4} eV.

Geometries were optimized using the conjugate-gradient scheme[93] with no symmetry restraints and no fixed atoms to a convergence of gradients to less than 10^{-3} eV/Å. To compute ab initio thermodynamics, the translational entropy (S) of gas-phase molecules only were calculated[115] under the assumption that rotational, and vibrational contributions to S are approximately constant. TS^{transl} at $T = 500$ K were calculated to be 1.50, 1.21, and 0.49 eV for gas phase HfX_4, HX, and H_2O respectively. This allows Gibbs free energies $\Delta G{=}\Delta E\text{-}T\Delta S$ of the reactions to be reported step by step.

Hafnium oxide has a different crystal structure at different temperatures.[116] The monoclinic phase is the most stable phase at low temperature, and our calculation showed that the (111) surface plane has the lowest energy. Therefore this plane has been regarded as a stable substrate for studying reactions during HfO_2 growth on HfO_2. The surface structure during actual ALD reactions is not known, but is certainly more complex. ALD produces amorphous or polycrystalline films of HfO_2, depending on precursor chemistry and growth temperature,[117] but the limitations of our periodic model do not permit us to simulate amorphous solids. Converged values of surface energies of the (111) surfaces showed that four layers of HfO_2 are enough to be considered as the slab.[118] To avoid slab-slab interaction in the periodic model, 10 Å was regarded as the vacuum distance. The k-point sampling in reciprocal space was generated by the Monkhorst-Pack method:[119] 4×4×4 and 4×4×1 grid sizes were utilized for bulk and slab respectively. For the hydroxylated surface, we used a four-layered 2×2 supercell and so k-point sampling was reduced to 2×2×1.

Ab initio MD calculations were carried out within the microcanonical ensemble.[120] The Verlet algorithm was used to integrate Newton's classical equations of motion for the ions. A time step of 1 femtosecond was found to be adequate

for all frequencies of oscillation in the system. The calculations were done for 400 ionic steps. The initial temperature for assigning random velocities was varied from 300 to 600 K, in line with ALD experiments.

In our modelling, we are confronted with the obstacle of rare events.[121] For long periods of time (relative to our MD simulation) the system is trapped in one minimum and cannot escape from that minimum. To observe the transition to a new minimum, very long MD simulations would be needed, which would be inaccessible with current computational power. We therefore tried out other plausible configurations (candidate minimums) by hand and checked stability with optimization or ab initio MD. Occasionally, chemical reactions occurred rapidly from the chosen configurations and were observed during optimization or MD. In those cases, we then looked for pathways showing how the system reached those configurations.

To calculate activation energies between two minima, we used the NEB approach[122,123] with climbing option. The conjugate gradient algorithm was found to be much faster than quasi-Newton methods to minimise forces in the NEB method and therefore conjugate gradient was employed for these calculations. To compute the activation energy of HX desorption from surface-Hf with NEB, only the Hf−N bond length was stretched and all other degrees of freedom were optimised. Up to ten images were considered in those reaction paths. The maximum change in ionic coordinates between images was 0.30 Å. In proton diffusion, several reaction paths between each pair of minima were searched to find the MEP (subsection 2.1.7). In the case of proton diffusion from oxygen to nitrogen, only the coordinates of the proton were fixed as it moved from one minimum to the other one. The maximum change in coordinates between images was 0.10 Å. For HX rotation, all atoms in the HX group were rotated around the Hf−N bond typically by 20° in every image.

Generally in ALD, we are looking for low reaction barriers, accessible at process temperatures of around 500 K (k_BT= 0.043 eV). In many cases, the barriers obtained were larger than 1 eV, and those are not reported here. For instance, for ligand rotation, the barrier is sensitive to whether the precursor is attached to O or OH. If attached to O, the precursor cannot move up from the surface and a higher barrier is obtained (1.78 eV), which is too high to be relevant for ALD. Instead we report the lower barrier for attachment to OH (0.05-0.39 eV). Furthermore, if the rotational barrier in one direction is larger than in the other direction then we quote the lower value of E_a.

3.3 End of H_2O pulse

Bare HfO_2 has many Lewis acid (Hf) and base (O) sites at the surface because of under-coordination. By contrast, at the end of the H_2O pulse in ALD, the surface is saturated with OH groups. In our model, we therefore added H_2O molecules to the bare (111) surface until we had obtained a hydroxylated surface. Those H_2O molecules are added to both top and bottom of the slab to minimise the slab dipole. The H_2O molecules initially are dissociated to H^+ and OH^-. Under-coordinated surface oxygen splits a proton from the water molecule and surface hafnium also gets a higher c.n. due to bonding to the OH group. The bond length between the Hf (c.n. = 7) and the terminal OH group at the surface (c.n. = 2) is 2.06 Å which is less than the bond length between the Hf (c.n. = 7) and O (c.n. = 3), 2.17 Å. When hafnium and oxygen atoms achieve a sufficiently high c.n., they do not dissociate water molecules at the surface any more. In other words, when the surface is saturated by hydroxyl groups, there are no Lewis acid and base sites to dissociate water molecules. At this stage, water molecules can persist at the surface. The bond length between Hf of the surface and an adsorbed H_2O molecule is 2.42 Å. Those molecules are not tightly bonded to the surface and during ab initio MD simulation at 500 K they were seen to separate from surface. The NEB calculation shows 0.46 eV barrier for dissociation of H_2O from the 7 coordinated hafnium at the surface. The resulting model of the surface had a coverage of 5 OH/nm^2 and 2 H_2O/nm^2.

3.4 Adsorption during Hf pulse

Although unreactive towards H_2O, the OH-terminated surface has Lewis basic oxygen sites, i.e. those that can make a chemical bond by electron donation to the metal of the precursor. Those active sites can be sorted into terminal hydroxyl groups, terminal oxygen, and bridging oxygen (Fig. 3.1). Terminal hydroxyl groups and terminal oxygen are one coordinated and bridging oxygen is two coordinated (excluding H). Our calculations show that the HfX_4 precursor cannot anchor to the bridging oxygen. Likewise, other oxygen atoms with even higher c.n. are inaccessible to the metal of the precursor. We find that only the terminal oxygen and hydroxyl oxygen are able to make a dative chemical bond with Hf of the precursor.

ΔE were calculated for the mentioned sites (Table 3.1, reactions 3,4,5). If the change in entropy in the adsorption reaction is considered, which is essentially from translational entropy, then the chemisorption is energetically unfavorable. ΔG are respectively 1.37, 1.49, and 1.65 eV for reaction 3 to 5 (Ta-

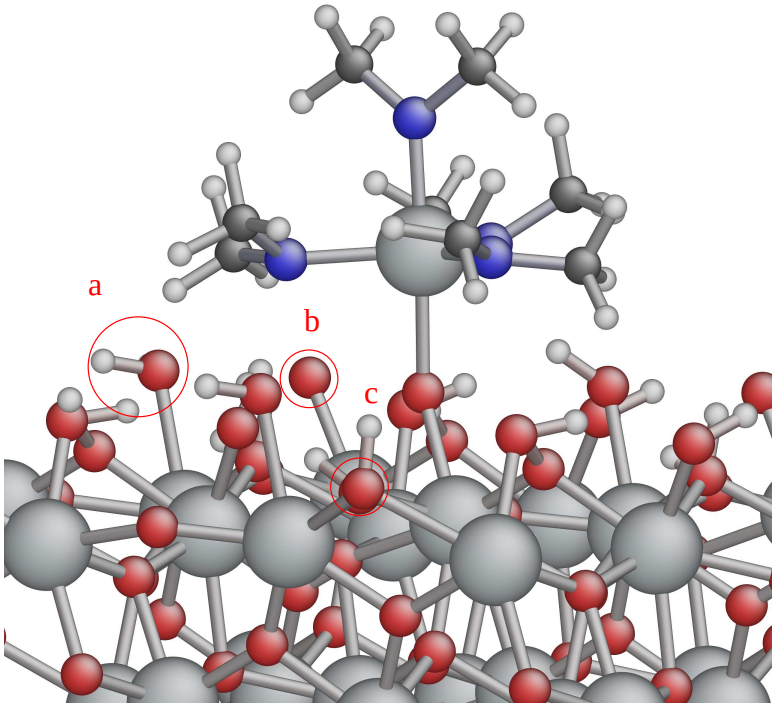


Figure 3.1: Optimized geometry for adsorption of HfX_4 molecule onto OH terminated HfO_2. Terminal hydroxyl group (a), terminal oxygen (b) and bridging oxygen (c) are highlighted. The HfX_4 is anchored to a terminal oxygen. (Red = O, Blue = N, White = H, large grey = Hf, small grey = C).

ble 3.1). The NEB calculation showed that the desorption barrier (E_a) for ($HfX_4(s) \longrightarrow HfX_4(g)$) is 1.00 eV and during ab initio MD also no evidence of desorption was observed. Therefore, we suggest that the hafnium precursor is anchored to the surface in a metastable state at either site for periods of time that are long enough for further reactions to take place.

3.5 Proton diffusion (during either precursor pulse)

On the growing surface during ALD, protons may be bound to O or to N (of the ligand) and hence there are many proton diffusion paths, which can be sorted as diffusion from oxygen to oxygen, oxygen to nitrogen, and nitrogen to nitrogen. All proton diffusion types are shown in Table 3.1. In the calculations of proton diffusion, changes in entropy are small and can be ignored, so only changes in energy are reported. Different diffusion pathways have different activation energies.

We consider first proton diffusion from oxygen to oxygen in different situations

Table 3.1: Diffusion barriers for protons in ALD and HfX_4 adsorption energies. E_a is activation energy and X = $N(CH_3)_2$. The 'dn' and 'up' indicate the position of proton on the nitrogen. surf-* means Hf precursor is anchored to * on the surface.

label	reaction	E_a (eV)	ΔE (eV)	explanation
1	$O_{c.n.=1}(s) + OH_{c.n.>1}(s) \rightleftharpoons OH_{c.n.=1}(s) + O_{c.n.>1}(s)$	0.00	0.00	—
2	$O_{c.n.=m}(s) + OH_{c.n.=m}(s) \rightleftharpoons OH_{c.n.=m}(s) + O_{c.n.=m}(s)$	0.75	0.00	m=1,2
3	$HfX_4(g) \rightleftharpoons HfX_4(s)$	1.00	-0.13	surf−O
4	$HfX_4(g) \rightleftharpoons HfX_4(s)$	1.00	-0.01	surf−OH
5	$HfX_4(g) \rightleftharpoons HfX_4(s)$	1.00	0.15	surf−H_2O
6	$HfX_4(s) + OH(s) \rightleftharpoons Hf(H_{dn}X)X_3(s) + O(s)$	0.05	-0.57	surf−OH
7	$Hf(H_{dn}X)X_3(s) + OH(s) \rightleftharpoons Hf(H_{dn}X)(H_{dn}X)X_2$	0.20	-0.19	surf−OH
8	$Hf(H_{dn}X)(H_{dn}X)X_2(s) + OH(s) \rightleftharpoons Hf(H_{dn}X)(H_{dn}X)(H_{dn}X)X(s) + O(s)$	0.30	-0.08	surf−OH
9	$Hf(H_{dn}X)(H_{dn}X)(H_{dn}X)X(s) \rightleftharpoons Hf(H_{up}X)(H_{dn}X)(H_{dn}X)X(s)$	0.51	-0.13	surf−OH
10	$Hf(H_{up}X)(X')X_2(s) \rightleftharpoons HfX(H_{up}X')X_2(s)^a$	0.59	-0.47	surf−OH
11	$Hf(H_{up}X)(H_{dn}X)X_2(s) \rightleftharpoons Hf(H_{up}X)(H_{up}X)X_2(s)$	0.49	-0.32	surf−OH
12	$Hf(H_{up}X)(H_{up}X)(H_{dn}X)X(s) \rightleftharpoons Hf(H_{up}X)(H_{up}X)(H_{up}X)X(s)^b$	0.42	-2.30	surf−OH
13	$Hf(H_{dn}X)(H_{dn}X)X(s) \rightleftharpoons Hf(H_{up}X)(H_{dn}X)X(s)$	0.38	0.00	surf−OH
14	$HfX_2(s) + OH(s) \rightleftharpoons Hf(H_{up}X)X(s) + O(s)$	0.91	-0.34	—
15	$Hf(H_{up}X)X(s) + OH(s) \rightleftharpoons Hf(H_{up}X)(H_{up}X)(s) + O(s)$	0.88	-0.27	—

[a] X′ shows the topmost nitrogen.
[b] densified precursor, this precursor is not stable at the surface.

(Table 3.1, reactions 1 and 2). Generally, we find that protons stay on under-coordinated oxygen. If we remove a proton from one-coordinated hydroxyl, the oxygen spontaneously dissociates a proton from a nearby H_2O molecule or from another hydroxyl with higher c.n. (reaction 1). These proton transfers are barrierless and take place during optimization. So we conclude that protons move quickly to the oxygen with lowest c.n.. However, there is a 0.75 eV barrier for proton diffusion from one or two coordinated oxygen to a similar oxygen with the same c.n. (reaction 2).

We investigated whether protons diffuse from the surface to sub-surface layers. A proton could not be optimized on the four coordinated oxygen of the sub-surface and it transferred spontaneously to the three coordinated oxygen. In another case, the existence of a proton on a four coordinated oxygen caused the bond between hafnium and that oxygen to break, with an overall cost for proton transfer of ΔE = +1.03 eV. Therefore during the processes of ALD, protons stay on top of the HfO_2 surface and do not diffuse into sub-surface layers of highly coordinated O.

Another type of proton diffusion is from oxygen to the ligand. For a bulky

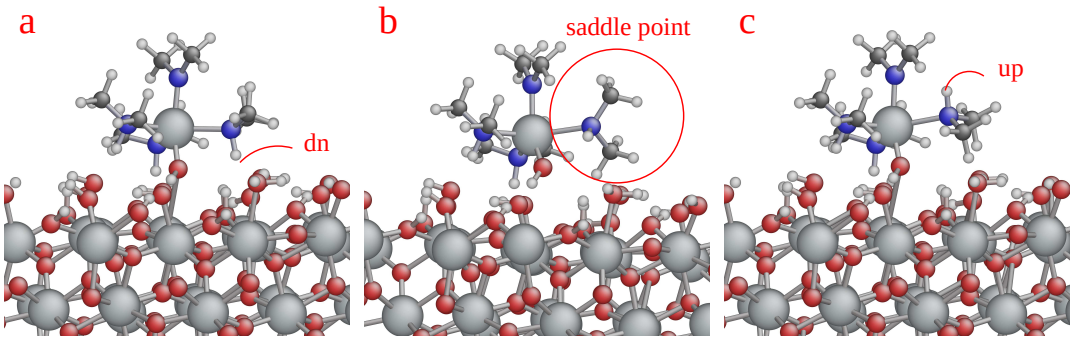


Figure 3.2: Rotation of protonated ligand from $Hf(H_{dn}X)(H_{dn}X)(H_{dn}X)X$ to $Hf(H_{dn}X)(H_{dn}X)(H_{up}X)X$, $X = N(CH_3)_2$ where the 'dn'(a) and 'up'(c) show the orientation of the proton on nitrogen relative to the surface. The saddle point is indicated in (b).

ligand like amide, there are various geometries for the protonated ligand HX. The NEB calculations showed that the rate of proton diffusion strongly depends on the distance that the proton hops from O to N. For example, we obtained a 1.35 eV barrier for diffusion of the proton across the distance 2.43 Å, while we obtained various values from 0.05 to 0.39 eV for the much shorter diffusion distance $\sim 0.7 \pm 0.05$ Å (Table 3.1, reactions 6, 7, and 8) (The corresponding O−N distances are similar, i.e. 2.8-3.0 Å). During ab initio MD or NEB calculations, these protons move up or down between the surface and the ligand. The bond length between Hf of the precursor and surface OH (c.n. = 3) is changed from 2.26 to 2.18 and 2.07 Å due to the first and second proton diffusion from the surface diffusion to the nitrogen (Table 3.1, reaction 6, 7).

Protons can also diffuse through the adsorbate via rotation of the protonated ligand HX (Fig. 3.2). The proton on nitrogen can be oriented down towards the surface or up away from the surface. Those locations are indicated by 'dn' and 'up' respectively in Fig. 3.2. Several reaction paths were regarded to find how the proton moves. The ligand needs space to rotate and this is facilitated by lengthening of the Hf$\cdots$O bond between the entire precursor and the surface. Such lengthening apparently costs more energy for surf−O−Hf ($E_a \sim 1.78$ eV for rotation of HX) than for surf−OH−Hf ($E_a \sim 0.51$ eV) (Fig. 3.2 and Table 3.1, reaction 9). In other words, a higher barrier exists towards amide rotation when the precursor is attached to terminal oxygen, and this is probably because terminal oxygen does not allow the precursor to move away from the surface as easily as OH does. The adsorption mode thus affects the rate of proton diffusion and hence of ligand elimination and ALD growth. The bond length between the Hf of the precursor and the surface OH (c.n. = 3) is slightly decreased from 2.18 to 2.15 Å because of the rotation of the protonated ligand in $Hf(H_{dn}X)X_3 \rightleftharpoons Hf(H_{up}X)X_3$.

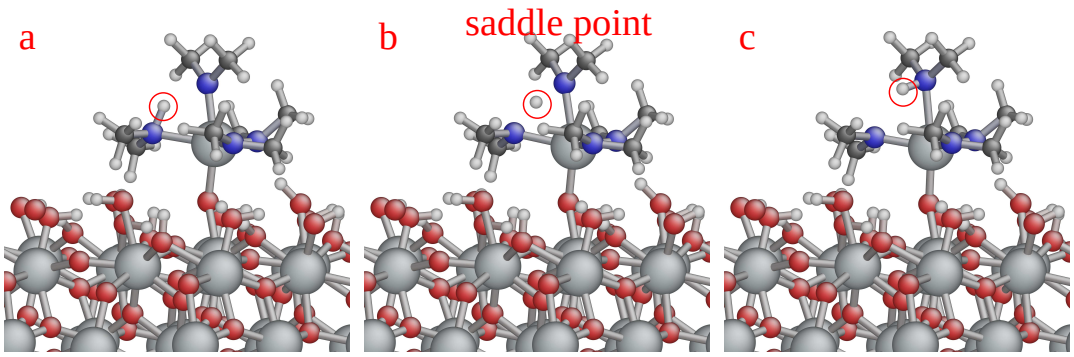


Figure 3.3: The highlighted proton diffuses from nitrogen to the topmost nitrogen. The saddle point is indicated in the middle snapshot (b).

Table 3.2: Activation energy for HX desorption from protonated HfX_4 and HfX_3 configurations i.e. probably Hf pulse. ΔG is free energy at $T = 500$ K and E_a is activation energy. $X = N(CH_3)_2$ and the 'dn' and 'up' show the position of proton on the nitrogen.

label	reaction	E_a (eV)	ΔE (eV)	ΔG^{500K} (eV)
1	$Hf(H_{dn}X)X_3(s) \rightleftharpoons HfX_3(s) + HX(g)$	0.89	-0.35	-1.56
2	$Hf(H_{up}X)(H_{dn}X)(H_{dn}X)X(s) \rightleftharpoons Hf(H_{dn}X)(H_{dn}X)X(s) + HX(g)$	0.89	-0.94	-2.15
3	$Hf(H_{up}X)(H_{up}X)(H_{dn}X)X(s) \rightleftharpoons Hf(H_{up}X)(H_{dn}X)X(s) + HX(g)$	0.39	-0.44	-1.65
4	$Hf(H_{up}X)(H_{up}X)(H_{up}X)X(s) \rightleftharpoons Hf(H_{up}X)X(s) + 2\,HX(g)$	0.00	-1.91	-4.33
5	$Hf(H_{dn}X)X_2(s) \rightleftharpoons HfX_2(s) + HX(g)$	1.69	-1.18	-2.39
6	$Hf(H_{up}X)(H_{up}X)(H_{dn}X)(s) \rightleftharpoons Hf(H_{up}X)(H_{dn}X)(s) + H_{up}X(g)$	1.09	-2.92	-4.13
7	$Hf(H_{up}X)(H_{up}X)(H_{dn}X)(s) \rightleftharpoons Hf(H_{up}X)(H_{dn}X)(s) + H_{up}X(g)$	1.07	-2.92	-4.13
8	$Hf(H_{up}X)(H_{up}X)(H_{dn}X)(s) \rightleftharpoons Hf(H_{up}X)(H_{up}X)(s) + H_{dn}X(g)$	1.73	-2.92	-4.13

Proton diffusion from nitrogen to nitrogen within the adsorbate after proton rotation is the final diffusion type that we consider (Fig. 3.3). $E_a = 0.59$ eV was calculated by NEB for this diffusion (Table 3.1, reaction 10).

3.6 Elimination of ligands and densification

The common assumption about the ALD mechanism is that proton transfer to a ligand, $X(s) \longrightarrow HX(s)$, is followed rapidly by desorption of the protonated ligand, $HX(s) \longrightarrow HX(g)$, before the next proton transfer step to the remaining precursor fragment.[115] Accordingly, the activation energy for desorption of the first HX from $Hf(H_{dn}X)X_3$ was calculated by NEB to be $E_a = 0.89$ eV (Table 3.2, reaction 1).

Here, we test the alternative mechanism, where multiple proton transfer gives $Hf(HX)(HX)X_2(s)$ or $Hf(HX)(HX)(HX)X(s)$ etc., followed later by desorption of HX(g) (Table 3.1, reactions 11, 12, and 13). As shown in Fig. 3.4, the Hf−N

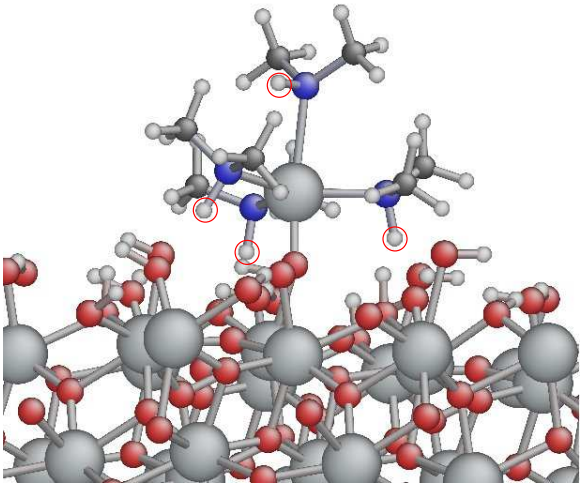


Figure 3.4: The Hf(H_{up}X)(H_{dn}X)(H_{dn}X)(H_{dn}X) precursor at the surface. Because of multiple proton diffusion, the topmost bond between Hf−N is stretched. Red circles show the diffused protons from the surface to the nitrogen.

distance increases from 2.2 to 2.6 Å as a result of protonation of the amide, showing that there is still substantial bonding between the neutral protonated amine (dn) and the Hf centre. Reaction 2 in Table 3.2 is dissociation of H_{up}X from Hf(H_{up}X)(H_{dn}X)(H_{dn}X)X. The activation energy E_a = 0.89 eV for this reaction is the same as that computed for reaction 1 in Table 3.2. To achieve this, a proton initially diffuses from the surface to nitrogen, then rotates to the 'up' position, and diffuses to the highest nitrogen, before finally desorbing as HX. Those diffusion steps are explained above.

These data show that rotation of the protonated ligand (Table 3.1, reactions 9, 11, and 12) has a much higher rate than dissociation of H_{up}X from the precursor (Table 3.2, reactions 1 and 2). For instance, using the computed E_a in the Arrhenius equation for 500 K shows that the rate of Table 3.1 reaction 9 is 4 orders of magnitude higher than Table 3.2 reaction 2.

In terms of activation energy the most likely desorption is reaction 3 in Table 3.2, in which three protons have diffused to the precursor and two amides have rotated upwards. These protons are highlighted in Fig. 3.5. The activation energy was calculated by NEB to be 0.39 eV. The rate of this reaction is therefore 6 orders of magnitude higher at 500 K than dissociation of H_{dn}X in Table 3.2 reaction 1 and 2. In other words, when the precursor has the Hf(H_{up}X)(H_{dn}X)(H_{dn}X)X configuration, the next proton rotation dn $\longrightarrow$ up makes the desorption of H_{up}X easier. We have observed that HX dissociates from Hf(H_{up}X)(H_{up}X)(H_{dn}X)X during ab initio MD (Fig. 3.5) at T = 500 K for 0.4 ps. Therefore H_{up}X is not

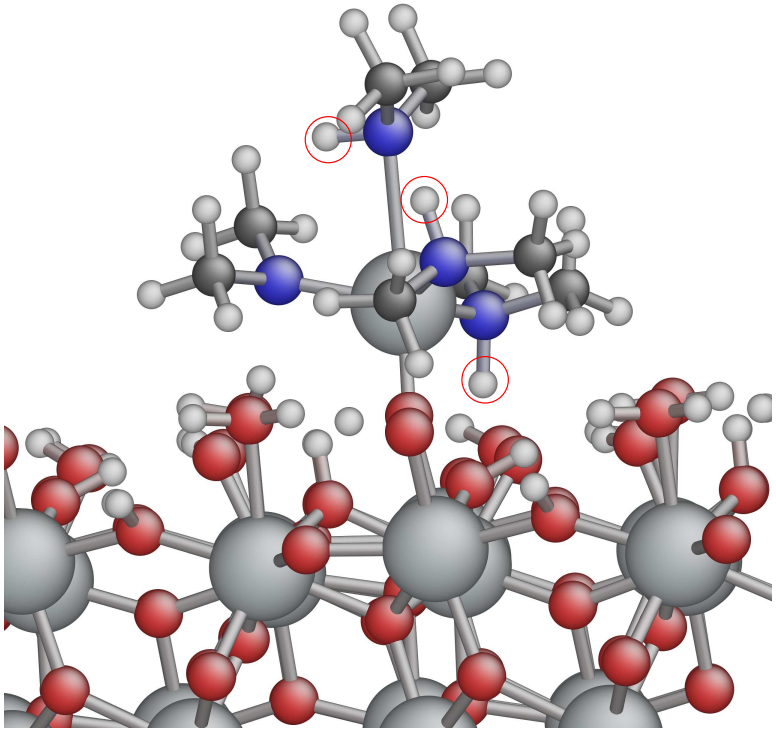


Figure 3.5: The Hf(H_{up}X)(H_{up}X)(H_{dn}X)X precursor at hafnium oxide surface. The topmost HX is dissociating from hafnium during ab initio MD calculation. Red circles show the diffused protons from surface to the ligands.

tightly bonded to the metal when another H_{up}X is present. The bond length between Hf of the precursor and the surface O (c.n. = 2) changes from 1.80 Å in Hf(H_{up}X)(H_{dn}X)(H_{dn}X)X to 1.82 Å in Hf(H_{up}X)(H_{up}X)(H_{dn}X)X.

The bonds between N and Hf in HfX_4 may have some covalent character. When the precursor chemisorbs to the surface, hafnium makes a bond with oxygen at the surface and hafnium becomes 5 coordinated. After the first elimination, the hafnium is once again 4 coordinated. With further elimination of HX, hafnium bonds with more oxygen at the surface, becomes more highly coordinated and thus densifies towards the bulk c.n..

Rotation of the third proton from Hf(H_{up}X)(H_{up}X)(H_{dn}X)X to Hf(H_{up}X)(H_{up}X)(H_{up}X)X (Table 3.1, reaction 12) causes spontaneous desorption of two HX at the same time (Table 3.2, reaction 4). In a similar way, as shown in Fig. 3.6, Hf moves spontaneously downwards into the surface during optimization of Hf(H_{up}X)(H_{up}X)(H_{up}X)(H_{up}X) and the Hf(H_{up}X)(H_{up}X) fragment densifies to the surface (i.e. c.n. of Hf increases from 4 to 6). The HX desorption step is barrierless in these cases.

As indicated in Table 3.2, multiple proton diffusion to N and rotation to H_{up}X reduces the activation energy for HX desorption. Upwardly-oriented HX disso-

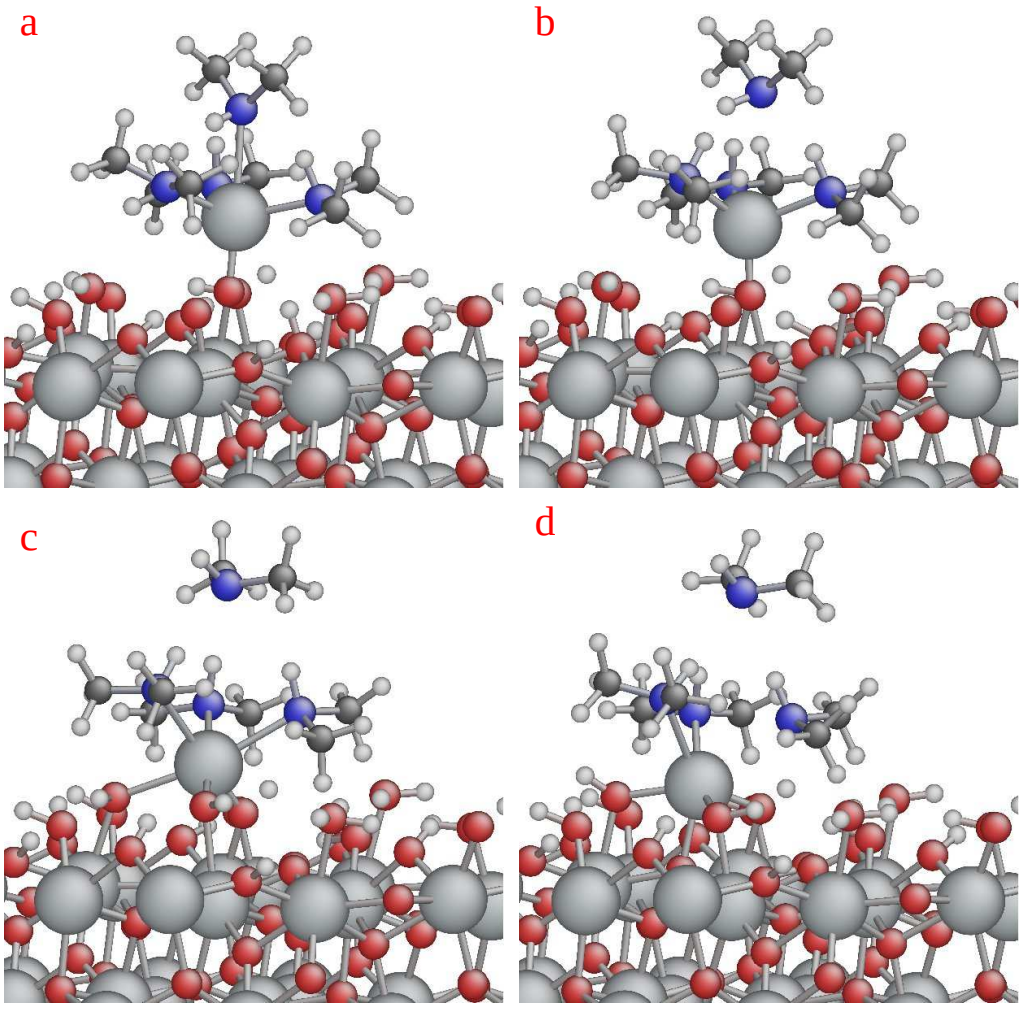


Figure 3.6: Snapshots from optimization of $Hf(H_{up}X)(H_{up}X)(H_{up}X)(H_{up}X)$ configuration. Hf moves down into the surface and becomes strongly attached to a total of four O atoms in the surface as 2 HX desorb spontaneously.

ciates readily from $Hf(H_{up}X)(H_{up}X)(H_{dn}X)$ during ab initio MD. Therefore as already observed above for HfX_4 configurations, the diffusion of multiple protons to the adsorbate increases the HX dissociation rate, in the case of ligands like X = amide. The bond length between the Hf of the precursor and the surface O (c.n. = 2) changes from 1.91 Å for HfX_3 to 1.87 and 1.81 Å in $Hf(H_{dn}X)X_2$ and $Hf(H_{dn}X)(H_{dn}X)X$ respectively. This bond length is not changed in $Hf(H_{up}X)(H_{up}X)(H_{dn}X)$.

A substantial exothermic energy difference ΔG= -4.1 eV at $T = 500$ K is seen for dissociation of the second HX (Table 3.2 reactions 6). This energy difference is higher than the first dissociation and this probably comes from densification, as shown in serial snapshots in Fig. 3.7. Loss of the second HX allows hafnium to move down into the surface and bond with under-coordinated oxygen. As the remaining amide groups are bulky in HfX_2 configurations, we found a small

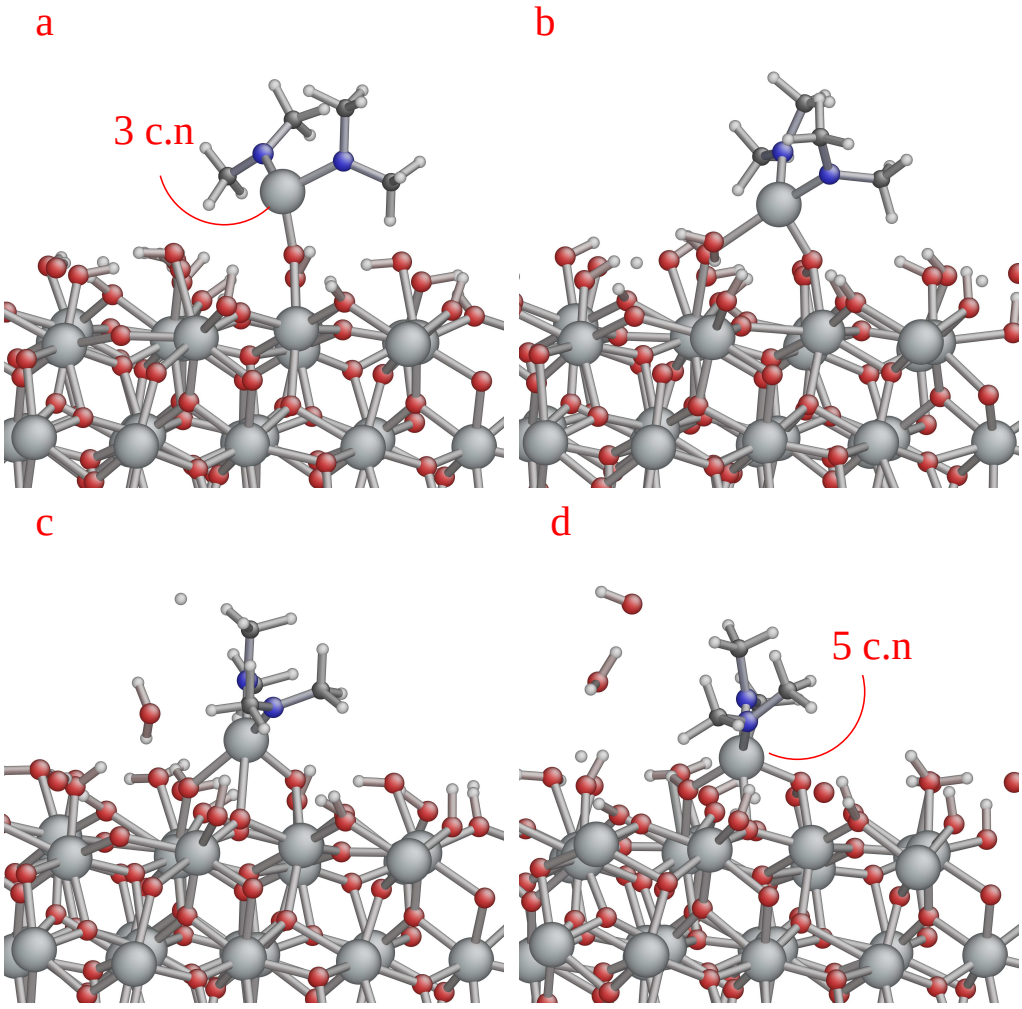


Figure 3.7: By densification, the c.n. of Hf in the precursor is increased as HfX_2 becomes strongly attached to 3 oxygen atoms at the surface. Snapshots are from ab initio MD at $T = 500$ K for 0.4 ps.

barrier towards this densification step, which is overcome during ab initio MD. After densification, the amide groups in HfX_2 are bent up (Fig. 3.7d) and so the next proton can be expected to travel a larger distance than in HfX_3 to bind to N and detach HX from hafnium. Indeed, calculations show a larger barrier than before for proton diffusion from oxygen to nitrogen (Table 3.1, reaction 14, 15).

When the precursor is densified to the surface, the Hf c.n. increases from 3 to 5. This changes the rate of subsequent dissociation of HX because we find a strong dependence of activation energies on c.n. of Hf for the crucial reaction steps of HX rotation and desorption. The activation energy $E_a = 1.13$ eV was calculated for HX dissociation from $Hf(H_{dn}X)X$ (Table 3.3, reaction 1). After densification, hafnium has a higher c.n., which may explain why this dissociation has a lower barrier than $Hf(H_{dn}X)X_2$ (Table 3.2, reaction 5). In the case of $Hf(H_{up}X)X$, $E_a = 0.89$ eV is calculated for HX desorption (Table 3.3, reaction 2).

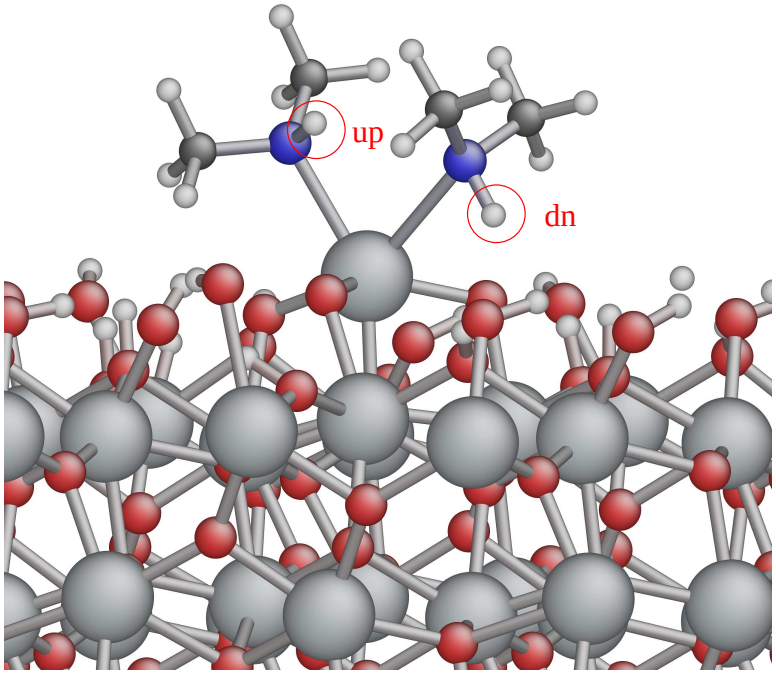


Figure 3.8: Optimized Hf(H_{dn}X)(H_{up}X) attached to 3 oxygen atoms at the surface where the 'dn' and 'up' show the orientation of the proton on nitrogen relative to the surface.

Multiple diffusion increases the dissociation rate in these configurations also (Fig. 3.8): Hf(H_{dn}X)(H_{up}X), has a lower barrier E_a = 0.30 eV (Table 3.3, reaction 3) than Hf(H_{dn}X)X.

As indicated in Table 3.3 reaction 3, exothermic ΔG = -0.40 eV was obtained for HX desorption from HfX_2. However, for dissociation of the last HX, the reaction is endothermic, ΔG = 0.53 eV, with a substantial activation barrier E_a=1.64 eV (Table 3.3, reaction 8). Hence the energetics favour Hf(HX) as the most likely fragment at the end of the HfX_4 pulse, if there are sufficient surface protons.

Another interesting reaction is transferring X from the adsorbed fragment HfX_2 to another under-coordinated Hf at the surface. As shown in Fig. 3.9, HfX_2 releases a ligand, which is transferred to the neighbouring hafnium and changes it from c.n. = 4 to c.n. = 5. This mechanism is observed during ab initio MD, indicating a small barrier.

Table 3.3: Reaction routes for HX dissociation after densification, and ligand exchange with oxygen, ΔG is free energy at $T = 500$ K and E_a is activation energy.

label	reaction	E_a (eV)	ΔE(eV)	ΔG^{500K}(eV)
1	$Hf(H_{dn}X)X(s) \rightleftharpoons HfX(s) + HX(g)$	1.13	1.36	+0.15
2	$Hf(H_{up}X)X(s) \rightleftharpoons HfX(s) + HX(g)$	0.89	1.03	-0.17
3	$Hf(H_{dn}X)(H_{up}X)(s) \rightleftharpoons Hf(H_{up}X)(s) + HX(g)$	0.30	0.80	-0.40
4	$4\,HfX(s) + H_2O(g) \rightleftharpoons 3\,HfX(HfH_{up}X)(s)^a + OH(s)$	0.00	-2.24	-1.75
5	$3\,HfX(HfH_{up}X)(s) + H_2O(g) + O(s) \rightleftharpoons 3\,HfX(HfH_{up}X)(s) + OH(s) + OH(s)$	—	-1.56	-1.07
6	$3\,HfX(HfH_{up}X)(s) + H_2O(g) \rightleftharpoons 2\,HfX(HfH_{up}X)(HfH_{up}X)(s) + OH(s)$	—	-1.19	-0.70
7	$2\,HfX(HfH_{up}X)(HfH_{up}X)(s) + H_2O(g) \rightleftharpoons HfX(HfH_{up}X)(HfH_{up}X)(HfH_{up}X)(s) + OH(s)$	—	-1.25	-0.76
8	$Hf(HX)(s)(c\cdot n\cdot = 5) \rightleftharpoons Hf(s)(c\cdot n\cdot = 4) + HX(g)$	1.64	1.74	+0.53
9	$Hf(HX)(s)(c\cdot n\cdot = 6) \rightleftharpoons Hf(s)(c\cdot n\cdot = 5) + HX(g)$	0.83	0.80	-0.40
10	$Hf(HX)(s)(c\cdot n\cdot = 7) \rightleftharpoons Hf(s)(c\cdot n\cdot = 6) + HX(g)$	0.56	-0.14	-1.35

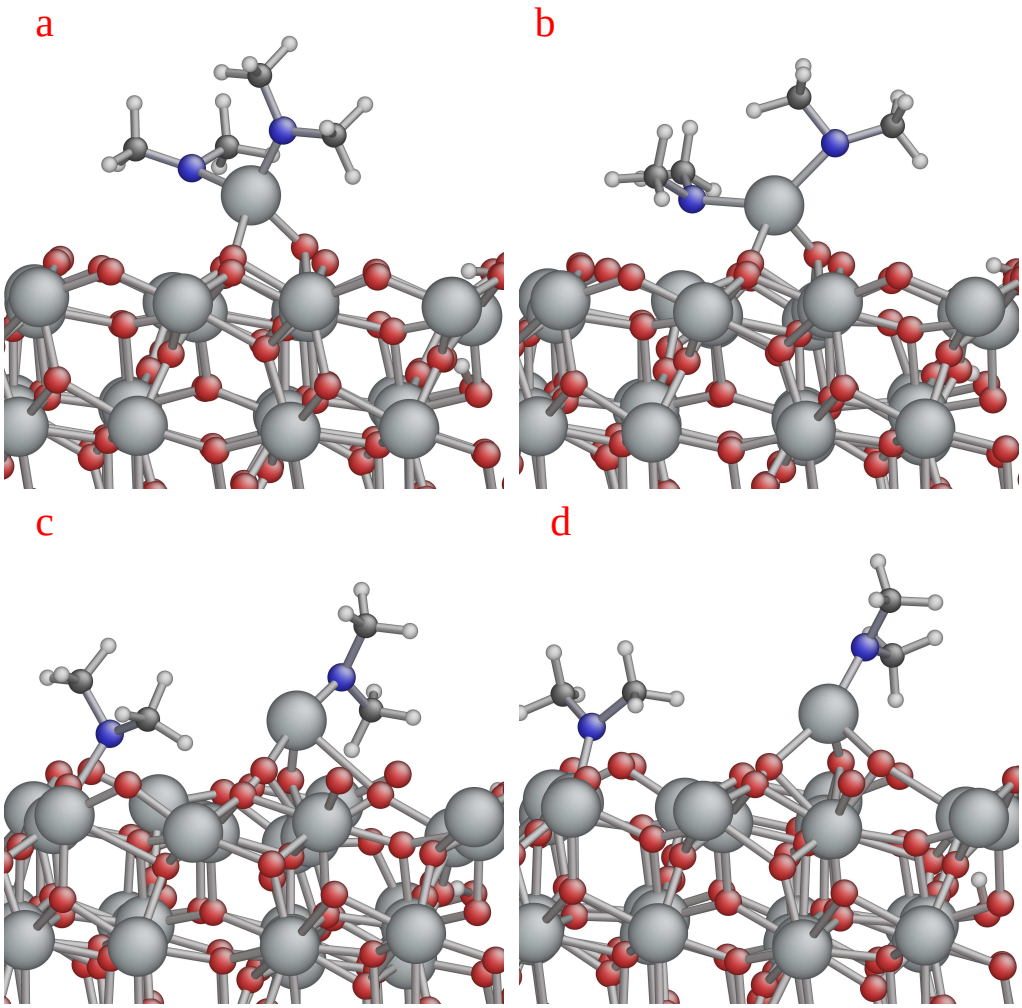


Figure 3.9: The amide group of the densified HfX_2 was transferred to under-coordinated hafnium at the surface; snapshots are from ab initio MD calculation, starting at $T = 500$ K and running for 0.4 ps.

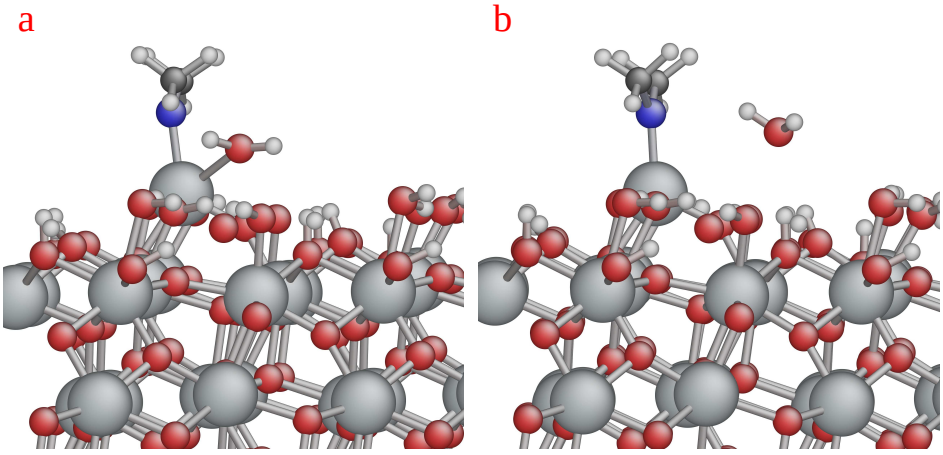


Figure 3.10: An adsorbed H_2O molecule is not dissociated but desorbs instead when there are not enough Lewis acid and base sites in terms of number; snapshots are from optimization.

3.7 Start of H_2O pulse

As was mentioned above (section 3.6), the most probable configuration for the metal precursor is predicted to be HfX or Hf(HX) at the end of the metal pulse. Therefore, during the subsequent water pulse, adsorbing H_2O interacts mostly with HfX (c.n. = 4 or 5 for Hf). In our models, we attached H_2O to HfX via $O\cdots Hf$ bonding (Fig. 3.10a), but when we have low population of exposed Hf at the surface, the attached H_2O is not dissociated and desorbs spontaneously from the system (Fig. 3.10b). It seems that there are not enough active sites on the surface to dissociate H_2O into OH^- and H^+. In the case of HfX_2, the problem is worse because of steric hindrance by X with H_2O. Moreover, other Hf in the sub-surface layers are 6 or 7 coordinated and so cannot effect dissociation of OH from H_2O.

However, a cluster of HfX leads to dissociation of adsorbed H_2O molecules. For instance, four HfX is considered as such a cluster. In Fig. 3.11a, four HfX are optimized on adjacent sites ($Hf\cdots Hf$ = 3.3-5.2 Å). We proceeded by adding H_2O molecules one by one to Hf atoms within the 4 HfX cluster at the surface (Fig. 3.11b). As indicated in Table 3.3, reaction 4, the first H_2O molecule is spontaneously dissociated to H^+ and OH^- during optimization. The proton is bound to N (Lewis base) as HX and the hydroxyl group is attached to Hf (Lewis acid). For the second H_2O, dissociation of the H_2O molecule does not take place instantly. So the H_2O molecule was taken apart to OH^- and H^+ by hand, and the new geometry was optimized (Table 3.3 reaction 5). This time the proton forms a bond to under-coordinated O at the surface. Indeed, occasionally both protons of the H_2O molecule were transferred to surface O and left two coordinate oxygen

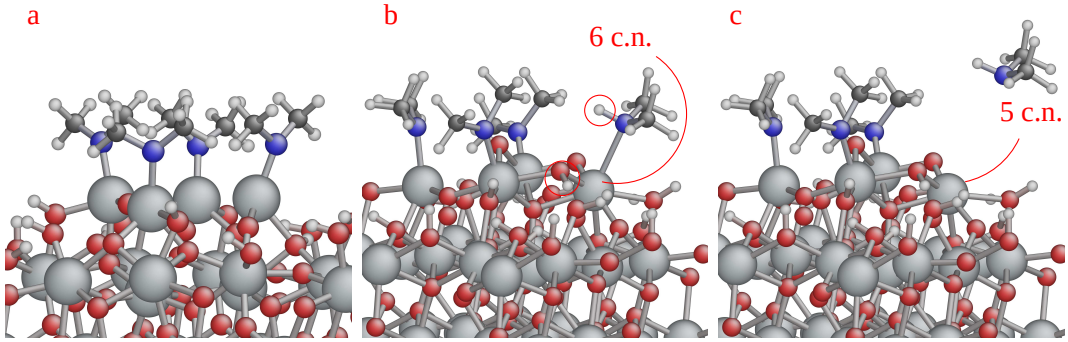


Figure 3.11: (a) The cluster of four HfX (b) The upper-most oxygen originally adsorbed as H_2O where red circles show typical OH and H from H_2O dissociation (c) Dissociation of HX from six coordinated Hf during the water pulse.

bridging between under-coordinated hafnium. For the next two adsorbing H_2O molecules (Table 3.3 reactions 6 and 7), the proton was optimized on nitrogen and the remaining hydroxyl group was bridging between under-coordinated hafnium. As there are many active sites (basic and acidic sites) in this surface model, calculation of activation energies for these steps was difficult to manage.

As tabulated in Table 3.3 from reactions 4 to 7, ΔE and ΔG are both negative for the dissociative chemisorption of H_2O. From reactions 4 to 6, whenever we add more H_2O molecules to the surface, ΔG and ΔE become less negative. This reduction seems to accompany the loss of Lewis acid and base sites through increased coordination to H_2O.

For HX loss, the opposite effect is seen in reactions 8 to 10 (Table 3.3) where ΔG becomes more negative as Hf c.n. increases. In other words, repeated adsorption of H_2O molecules increases the c.n. of Hf and is accompanied by the simultaneous dissociation of more and more HX from the surface. The activation energy is reduced from 1.64 eV to 0.56 eV for the last HX dissociation from Hf(HX) (Table 3.3 reactions 8 and 10). In the case of Fig. 3.11b, $3H_2O$ were added and optimized. The E_a for loss of HX is 0.83 eV when Hf is six coordinated. Another H_2O molecule was added to the c.n. = 6 hafnium that is shown in Fig. 3.11b producing Hf with c.n. = 7 to oxygen (Fig. 3.12a). E_a = 0.56 eV is the activation energy for the last HX dissociation (Table 3.3, reaction 10).

3.8 Discussion of densification of $Hf(N(CH_3)_2)_4$ and H_2O molecules

Ab initio calculations show that the Hf of the precursor adsorbs by making a dative bond with the Lewis base sites at the surface. Formation of Hf−O bonds is energetically favorable. The existence of low coordinated O or OH is necessary

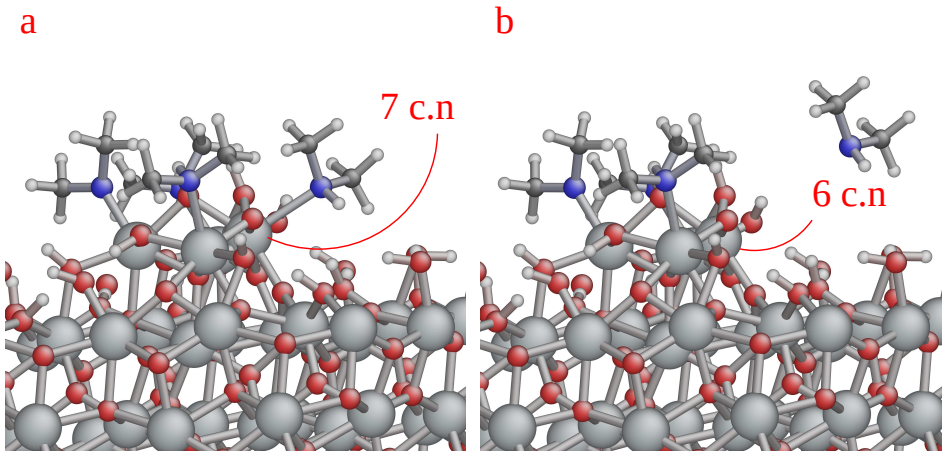


Figure 3.12: Dissociation of HX from seven coordinated hafnium during water pulse. Four oxygen (originally adsorbed as H_2O) are coordinated to the cluster and dissociation of HX from the resulting 7-coordinate Hf is more favourable than the situation in Fig. 3.11.

for the dative bond to persist. The dative bond between the Hf of the precursor and high coordinated O (c.n. = 2) is not strong enough to preserve it for further reactions. The low and high coordinated O sites are created by decomposition of H_2O molecules during the H_2O pulse. Their equilibrium population essentially depends on the temperature of the substrate, which rules the rate of adsorption and finally the rate of growth in ALD. We could not find any reaction path for other adsorption modes of HfX_4 or for direct reactions between X of gas-phase HfX_4 and surface protons. The existence of the Hf−O dative bond is the necessary prerequisite for HX elimination.[124]

As the existence and mobility of Brønsted acidic protons is crucial in the ALD of oxides, various proton diffusion pathways are inspected (Table 3.1). Proton diffusion from oxygen to oxygen has various barriers, which change according to the c.n. of oxygen. Generally protons remain on low coordinated oxygen, and therefore remain primarily at the surface rather than in the bulk. The existence of protons at the surface makes them available as co-reagents for the dissociation of ligand fragments.

The proton diffusion from oxygen to ligand nitrogen is another type of proton diffusion. In our simulations, this proton hops frequently between oxygen and nitrogen and may be thought of as a shared proton between the oxygen and nitrogen. The desorption barriers of the fragment $H_{dn}X$ are relatively large, but are lowered by a factor of 2-3 by rotation of the protonated ligand to $H_{up}X$ (Table 3.1, reactions 9, 11, and 12 respectively), hence facilitating the desorption of the fragment $H_{up}X$. For all proton diffusion pathways, which are tabulated from reaction 6 to 13 in Table 3.1, the barriers are lower than the desorption

barrier for $H_{dn}X$ (Table 3.2 reaction 1 and 2), which makes proton diffusion more probable than desorption of $H_{dn}X$ at the initial stage of precursor adsorption. In other words, multiple ligands become protonated before desorption commences.

Proton diffusion from the O of surface to the N of HfX_4 shows relatively low barriers and exothermic reactions energies (Table 3.1, reactions 6, 7, and 8). However, these proton diffusion barriers in HfX_2 are much higher than in HfX_4, at least for smooth surfaces (Table 3.1, reactions 14 and 15), because the proton must then travel a larger distance from O to attach to the N. However, if HfX_2 is densified into the sub-surface layers, then Hf is surrounded by more oxygen than at the smooth surface. In this case, the proton may travel a shorter distance to attach to the nitrogen than on the smooth surface. The proton diffusion barrier therefore is lower. An alternative route to protonated HfX_2 is by repeated loss of HX from larger protonated fragments such as $Hf(H_{up}X)(H_{up}X)(H_{up}X)(H_{dn}X)$. The resulting $Hf(H_{up}X)(H_{dn}X)$ species can densify directly, without the need for proton diffusion.

However, if Hf of the precursor is not coordinated to enough oxygen from the surface, for instance if it bonds to just two oxygen atoms, in spite of multiple diffusion, the HfX_2 or $Hf(HX)_2$ configuration keeps both ligands. This illustrates the link between ligand loss and coordination to the surface, as already computed by Zydor and Elliott for Ti precursors.[124]

Diffusion of protons from the surface oxygen to the nitrogen in ligands weakens the bonds between hafnium and ligands. Then, as noted above, rotation of protonated ligand dn $\longrightarrow$ up lowers the activation energy for HX desorption significantly. The more protonated ligands that rotate, the more rapidly the dissociation of HX proceeds. In the extreme case, we observed that two ligands spontaneously dissociated from $Hf(H_{up}X)(H_{up}X)(H_{up}X)X$ and Hf simultaneously densified to the surface. In other words, the system prefers to pass several low barriers instead of few high barriers in ALD. When the temperature is increased, those pathways with high barriers become more active. For instance, thermally-activated decomposition reactions that do not need co-reagents such as H^+ (i.e. standard chemical vapour deposition) may become active at higher temperatures. However, we have not computed such reactions here.

Hf in HfX_4 is bound to a single O and so is 5 coordinated. By loss of a ligand, it becomes 4 coordinated HfX_3. We find that dissociation of another HX from HfX_3 configurations is harder than from HfX_4 ones. (Table 3.2, reactions 1 and 5), showing that second elimination is harder in ALD. The other interesting point is the effect of ligand rotation on the desorption of HX from $Hf(H_{up}X)(H_{up}X)(H_{dn}X)$. As indicated in Table 3.2, reactions 6 and 7 have similar activation energy for $H_{up}X$ dissociation, while the activation energy for $H_{dn}X$

dissociation in reaction 8 is too high for this reaction to be active in ALD. Hence, the proton rotations in HfX_3 configurations also change the dissociation rate.

The bonding between the Hf of the precursor and the low coordinated O changes in response to proton diffusion from the surface to the ligands and rotation of protonated ligand. For instance, multiple proton diffusion decreases the Hf−O bond length from 2.26 Å in HfX_4 to 1.82 Å in $Hf(H_{up}X)(H_{up}X)(H_{dn}X)X$, which is lower than the normal distance between Hf and O in the bulk structure (2.17 Å). This effect appears to be primarily due to the proton diffusion from the surface to the complex, while the rotation of the protonated ligand is only slightly influential.

We observe that densification is the primary energetic driving force at the surface. Substantial energy gain can be seen to accompany the formation of new Hf−O bonds in reactions 4 to 8 in Table 3.2. Densification is reported here for a smooth surface, where Hf of the precursor bonds to 3 or 4 oxygen atoms at the surface. Densification may also happen in sub-surface layers during ALD growth, where Hf and O rearrange so as to obtain more mutual bonding partners, increasing their coordination and density closer to bulk values. In this case, we expect that densification is even more energetically favorable. This leads us to speculate that there will also be a strong driving force for Hf and O ions, once freed of ligands or protons, to migrate from the surface to sub-surface vacancies, thus densifying and completing those layers into bulk-like HfO_2. This would explain the excellent conformality that is achieved in ALD, despite the sub-monolayer rate of growth per cycle. Each ALD cycle thus consists of two simultaneous modes of deposition: completion of high-density sub-surface layers and decoration of the surface with a low-density film. Of course, the situation may be different during the first few cycles of 'incubation' on a substrate.

Based on the computed energetics, HfX is the most probable configuration in the Hf pulse and desorption of this final HX is an endothermic reaction (Table 3.3 reaction 8). This seems to be because HfX is relatively under-coordinated. One bond from X and 3 or 4 bonds from oxygen (on a smooth surface) make Hf 4 or 5 coordinated. Desorption of the last ligand only becomes possible if Hf can coordinate to more oxygen, either during the oxygen pulse or by densification into a position with a higher number of surrounding oxygen (Table 3.3, reactions 8, 9, and 10). Because ideal ALD is symmetric with respect to pulses, the energetics also allow us to identify the most probable surface species saturating the surface at the end of the H_2O pulse. This is low-coordinated hydroxyl, with just one bond to the surface, which resists any type of proton transfer reaction (Table 3.1, reaction 1). Only during the next precursor pulse does adsorption of HfX_4 allow the c.n. of such OH groups to increase, facilitating proton transfer and

densification.

Our calculations show that the H_2O molecule in the oxygen pulse can only adsorb by attaching to a pair or cluster of neighbouring HfX, which is followed by decomposition of the H_2O molecule (Table 3.3 reaction 5). Adsorption of H_2O to a single HfX is not energetically favoured (Fig. 3.10), indicating that the presence of X makes HfX a weak Lewis acid. Also, no evidence of a direct reaction between a proton of the gas phase H_2O molecule and surface ligands was observed, again confirming that chemisorption is needed before HX elimination. If such clusters of HfX do not form in the Hf pulse, which may happen in low temperature or on different interfaces, then H_2O cannot adsorb efficiently in the oxygen pulse. In general, a low number of Lewis acid and base sites after the Hf pulse leads to a low rate of H_2O deposition in the O pulse.

Repeated decomposition of H_2O leads to an increase in c.n. of Hf and O in the cluster. Simultaneously, the densification of Hf and O in the cluster causes a reduction in the barriers to HX desorption (Table 3.3), and the rate of desorption of HX is increased. For this reason, previously inert Hf(HX) can be eliminated in the H_2O pulse. Depletion of HX from the cluster in turn allows further densification: Hf gains c.n. up to 7 by densification with surrounding O while the oxygen obtains wide range of c.n. from 1 to 4.

At this stage, the possibility of association of $H^+ + OH^-$ into H_2O molecules is raised. According to our calculations, terminal -OH_2 with the low coordination of oxygen is more likely to desorb than bridging -OH_2- especially as the temperature is raised. As noted previously, terminal O is the most reactive towards HfX_4 adsorption in the next Hf precursor pulse and so the rate of ALD growth per cycle would be directly lowered as a result of the reduction in adsorption sites. In addition, H_2O desorption depletes the surface of reactive protons for ALD.

In our slab model, under-coordinated surface atoms (oxygen in the hafnium pulse and hafnium in the oxygen pulse) change the activation energies and free energies for reactions in their vicinity, reactions such as desorption of ligands and ligand exchange. Although they appear to be spectators in these reactions, in fact these under-coordinated atoms strongly affect the reaction pathways and energetics, often changing them from endothermic to exothermic reactions. For instance, the substantial gain in energy during the densification process is from under-coordinated atoms. These under-coordinated atoms are ignored in calculations using more limited models.[28,29]

3.9 Summary

In this chapter, we used DFT slab models to investigate the ALD reactions for growth of HfO_2 from $Hf(N(CH_3)_2)_4$ and H_2O. We include all steps, from the early stage of adsorption of each ALD precursor to the densification of multiple atoms into bulk-like HfO_2 layers. The resulting reactions, which explain the fundamental chemistry of ALD at low temperatures (below 500 K), are outlined below.

Adsorption: Chemisorption of precursors is only possible at surface sites of sufficient Lewis activity, namely terminal O and OH for $Hf(N(CH_3)_2)_4$ and $(Hf(N(CH_3)_2))_x$ ($x \geq 2$) clusters (*e.g.* dimers) for H_2O. Saturated surfaces do not have these sites and so resist further adsorption. This explains the self-limiting reactions that distinguish ALD from other techniques.

Multiple proton diffusion: We propose the diffusion of multiple protons to the amide ligands of the Hf precursor before desorption of protonated ligands takes place. The activation energy calculations show that repeated proton diffusion from the surface to the amide ligand and rotation of the protonated amine is more energetically accessible than the simple elimination of the amine in the initial stage. Due to multiple proton diffusion to the fragments, the dative bonds between Hf and N are weakened. This reduction in bond strength facilitates the desorption of fragments from the precursor. The resulting activation energies for protonation and desorption of ligands are low enough that these reactions can take place in low temperature ALD. Multiple proton diffusion is seen in all the stages of ligand elimination.

Densification: Loss of a proton from oxygen frees it up for bonding to Hf of the precursor. Protonation of ligands, and especially desorption of ligands, frees up Hf for bonding to surface oxygen. Decomposition of H_2O at the surface also increases the coordination of Hf and O. These effects are termed 'densification', as they bring Hf−O packing closer to the bulk scenario. Densification is hence accompanied by substantial energy gain and this can be the driving force that facilitates ligand eliminations at the surface and vacancy filling in sub-surface layers. Densification thus accounts for some of the important characteristics of ALD, such as conformal growth.

Saturated surfaces: During the early stage of the metal pulse, due to the saturation of the surface by remaining fragments HfX, adsorption of further metal precursor stops. The presence of these fragments prevents further chemisorption of HfX_4, since this requires the creation of a strong dative bond between Hf and O. A separate effect is depletion of co-reagent (protons) at the surface as HX desorbs. Clearly, no further elimination of HX is possible once protons are exhausted. If

the surface can store a higher population of co-reagent, then a higher growth rate is expected.[125] Next, during the H_2O pulse, Hf exchanges its remaining ligands with OH groups. The exchange occurs due to the decomposition of adsorbed H_2O molecules in clusters of HfX. Simultaneously, low coordinated oxygen atoms appear at the surface, which are reactive sites for the next metal pulse. With saturation of the surface by OH groups, H_2O molecules begin to appear. These molecules are loosely bonded to the surface and readily desorb, reducing the growth rate, especially at high temperatures.

It can thus be seen that a wide variety of reactions can take place simultaneously on the surface during ALD. Competition between the elimination reactions and proton diffusion reactions at different ALD temperatures, and their influence on the conformality of the film, are interesting issues that we investigate by incorporating these DFT data into KMC modelling (chapter 5 and 6).

Chapter 4

Cooperation effects in both metal and oxygen pulses

The common assumption about the ALD mechanism for oxides is that the dominant reaction is proton transfer to a ligand, which is followed rapidly by desorption of the protonated ligand. However, in the previous section we showed that multiple proton diffusion is the effective pathway in the case of alkylamide. Here, we demonstrate another essential pathway, co-adsorption, that plays an important role in ALD. This mechanism was already observed for $4\,HfX + H_2O$ in section 3.7. By this we mean that previously-inert fragments can become reactive once sufficient numbers of molecules adsorb in their neighbourhood during either precursor pulse. Through the calculated activation energies and energies of reaction, the 'cooperative' mechanism is shown to have a profound influence on proton transfer and ligand desorption.

In this section, two distinct types of cooperative effect for H_2O pulse will be presented: (I) cooperation between the remaining precursors to adsorb the incoming H_2O molecule, (II) cooperation between the adsorbed H_2O molecules from the arrival of gas phase. Both types facilitate the proton transfer and ligand desorption. We will show that considering reasonably larger selection of adsorbates modifies the rate of desorption as consequence of change in the rate of proton diffusion.

4.1 Introduction

In ALD, a precursor molecule at a surface site is transformed via series of reactions into a unit of growing film (*e.g.* HfO_2 from $Hf(N(CH_3)_2)_4$ and H_2O) (chapter 3). Therefore, models have to date mostly considered an isolated precursor molecule at a single surface site and resulting intermediates, often for

reasons of computational expediency. In this section, we show that these models are deficient. Each precursor molecule (or fragment thereof) is surrounded by other adsorbates/fragments on the surface and, as we show here, these neighbours have a substantial effect on the kinetics of the ALD reactions of the particular precursor, even though the atoms of the neighbours do not participate directly (either stoichiometrically or catalytically) in these reactions (Fig. 4.1). This is consistent with the work presented in section 3.7, where we saw a strong dependence on c.n. in the adsorption and dissociation of H_2O molecules reactions in the cluster of remaining precursors.[95] We term this a "cooperative effect". We examine the main reaction steps in three representative processes $Al(CH_3)_3/H_2O$, $Hf(N(CH_3)_2)_4/H_2O$ and $HfCl_4/H_2O$ and hence conclude that the cooperative effect is general to the ALD of metal oxides.

Adsorbate-adsorbate interaction was observed before in heterogeneous catalysis.[126,127] To examine the influence of co-adsorbates for ammonia synthesis, Honkala *et al.*[126] used DFT to determine activation energies while changing the adsorbates in neighbouring sites on the surface. The resulting activation energies change from 0.49 eV to 1.25 eV according to their the local environment. Very recently Miller *et al.*[127] used DFT to describe the influence of co-adsorbates on activation energy for O_2 dissociation on Pt(111). Their results show that activation energies change from 0.24 to 0.76 eV and depend on the coverage of O_2 at the surface.

However, the ALD reactions involve densification. Densification is defined as the increase in density due to improved metal-oxide packing, associated with an increase in c.n. of metal and oxygen from their molecular values toward bulk solid values.[95,111] Hence, to describe the change of activation energies in different local environments, the interaction between remaining fragments in the metal pulse is considered before and after densification. Similarly, it will be shown that protonation and desorption of remaining ligands will be facilitated in the oxygen pulse through co-adsorption of oxygen precursors in a cluster of remaining precursor (Fig 4.2).

4.2 Computational details

To model the growth reactions of metal oxides from $Al(CH_3)_3$ (TMA), $Hf(N(CH_3)_2)_4$ (TDMAHf), hafnium tetrachloride and H_2O, self-consistent DFT[112] was used (subsection 2.1.3). To optimize the geometries, we used periodic DFT with the projector augmented wave method and the PBE[51] functional as implemented in the Vienna ab initio simulation package (VASP).[41] The plane wave cutoff energy was 400 eV. Geometries were optimized using the conjugate-gradient

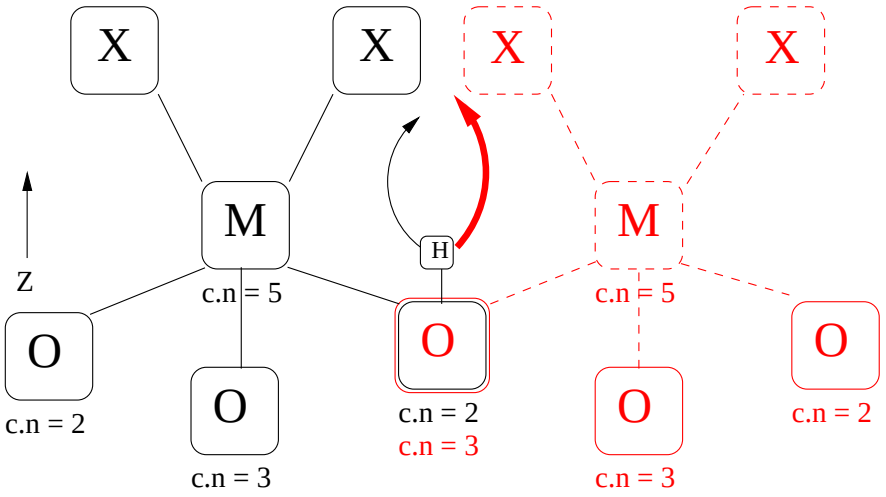


Figure 4.1: A schematic diagram of proton diffusion from the surface to a ligand of the precursor. Co-adsorption of a second fragment (red) increases the c.n. of the central surface oxygen. Hence, the rate of proton diffusion increases significantly (red arrow). Boxes show elements that are oxygen (O), metal (M), proton (H), and ligand (X) in a two dimensional cross-section but the actual c.n. in three dimensions is also given. z shows the direction of growth. The black lines show bonds between the first fragment and the surface while the dashed lines show bonds between the second fragment and the surface.

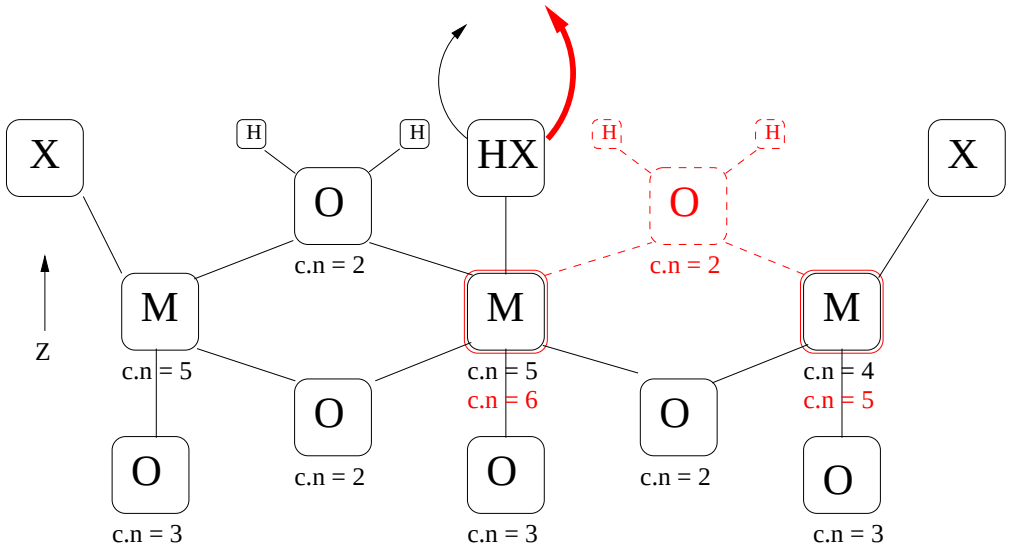


Figure 4.2: A schematic diagram of the cooperative effect of H_2O co-adsorption on ligand desorption. Adsorption of another H_2O molecule into the cluster of remaining MX fragments (the dashed lines) increases the c.n. of the metal atoms. Hence, the rate of desorption of a protonated ligand from a metal atom (arrows) increases significantly (same scheme as Fig. 4.1).

scheme to a convergence of gradients to less than 10^{-3} eV/Å. We calculated activation energies (E_a) between two minima using the NEB approach,[122,123] which is implemented in VASP. The statistical distribution of fragments of TDMAHf precursors at the surface is obtained from the stochastic parallel particle kinetic simulator (SPPARKS) code,[109,110] in which we have implemented ALD surface reaction as a new feature using rejection kinetic Monte-Carlo (rKMC)[39] (chapter 5). As we have not implemented the $Al(CH_3)_3$ and $HfCl_4$ chemistries into the rKMC yet, we assume that they exhibit the same statistical distribution in terms of number of remaining fragments at the end of the metal pulse as TDMAHf.

4.3 Cooperative effect in growth of Al_2O_3 from methyl precursors and H_2O molecules

As seen before in the literature,[115] adsorption of AlX_3 (for simplicity X=CH_3) occurs at surface oxygen atoms (Lewis basic sites) (Fig. 4.3a). In most cases, the surface oxygen atoms are twofold coordinated before adsorption (excluding H). Proton transfer to the methyl group causes the dissociation of methane from the metal precursor. In other words, proton transfer breaks the bond between Al−C and this Al simultaneously forms new bonds to the another oxygen at the surface (Fig. 4.3b). In the standard model, adsorbate-adsorbate interaction is not considered and desorption of each HX is reported to be exothermic.[115]

In order to examine the role of cooperation between adsorbate molecules and the surface oxygen in ligand desorption, we calculated activation energies for proton diffusion from different oxygen atoms at the surface to the carbon of the ligand (for first HX desorption) (Table 4.1 reaction 1). The lowest activation energy is $E_a = 0.28$ eV from the anchor OH group to the carbon of the ligand (Fig. 4.3a). The highlighted OH group is threefold coordinated (excluding H) because of bonding to the Al of adsorbed AlX_3. By contrast, the other neighbouring O are one- or two-coordinated and do not release a proton easily to the precursor, so that the calculated activation energies are much higher (*e.g.* 0.74 eV).

A single AlX_2 is considered at the surface (Fig. 4.3b). We attempted to transfer the proton of a low coordinated OH group to the carbon (Fig 4.3b). However, the transferred proton comes back to the oxygen during optimization. Hence, the second desorption does not occur in this situation. In order to check the effect of cooperation between the remaining fragments on the second HX desorption, we considered two clusters. First, we assume that $2\,AlX_2$ are adsorbed in close proximity and the activation energy for proton diffusion from three coordinated oxygen is found to be 0.34 eV (Table 4.1 reaction 2). Second, the remaining

Table 4.1: Reaction routes for proton transfer, ligand dissociation, and ligand exchange with oxygen, ΔE is energy difference and E_a is activation energy. X=CH_3 and $N(CH_3)_2$ for Al and Hf respectively.

label	reaction	E_a (eV)	ΔE (eV)
1	$AlX_3(s) + OH(s)(c\cdot n\cdot = 3) \rightleftharpoons AlX_2(s) + O(s)(c\cdot n\cdot = 3) + HX(g)$	0.28	-0.78
2	$2\,AlX_2(s) + OH(s)(c\cdot n\cdot = 2) \rightleftharpoons AlX_2(s) + AlX(s) + O(s)(c\cdot n\cdot = 2) + HX(g)$	0.34	-1.78
3	$AlX_2(s) + AlX(s) + OH(s)(c\cdot n\cdot = 3) \rightleftharpoons AlX(s) + AlX(s) + O(s)(c\cdot n\cdot = 3) + HX(g)$	0.26	-0.58
4	$AlX(s)(c\cdot n\cdot = 4) + OH(s)(c\cdot n\cdot = 3) \rightleftharpoons Al(s)(c\cdot n\cdot = 3) + O(s)(c\cdot n\cdot = 3) + HX(g)$	1.28	+1.47
5	$3\,AlX(s) + H_2O(s) \rightleftharpoons 2\,AlX(s) + Al(s) + OH(s) + HX(g)$	0.52	-1.54
6	$3\,AlX(s) + 2\,H_2O(s) \rightleftharpoons 2\,AlX(s) + Al(s) + H_2O(s) + OH(s) + HX(g)$	0.00	-1.12
7	$2\,HfX_2(s) + OH(s)(c\cdot n\cdot = 3) \rightleftharpoons HfX_2(s) + Hf(HX)X + O(s)(c\cdot n\cdot = 3)$	0.64	-0.86
8	$2\,Hf(HX)(HX)(s) \rightleftharpoons Hf(HX)(HX)(s) + Hf(HX) + HX(g)$	0.18	+0.28
9	$HfHX(s)(c\cdot n\cdot = 5) \rightleftharpoons Hf(s)(c\cdot n\cdot = 4) + HX(g)$	1.64	+1.74
10	$4\,HfX(s) + H_2O(s) \rightleftharpoons 3\,HfX(HfHX)(s) + OH(s)$	0.00	-2.24
11	$HfHX(s)(c\cdot n\cdot = 7) \rightleftharpoons Hf(s)(c\cdot n\cdot = 6) + HX(g)$	0.56	-0.14
12	$4\,HfCl_4(s) + 4\,H_2O(s) + H_2O(g) \rightleftharpoons 3\,HfCl_4(s) + 4\,H_2O(s) + HfXCl(s) + OH(s) + HCl(g)$	0.00	-1.14
13	$2\,HfCl_3(s) + OH(s) \rightleftharpoons HfX_3(s) + HfCl_2(s) + OH(s) + HCl(g)$	0.46	-1.30
14	$3\,HfCl_2(s) + OH(s)(c\cdot n\cdot = 3) \rightleftharpoons 2\,HfCl_2(s) + Hf(HCl)Cl(s) + O(s)(c\cdot n\cdot = 3)$	0.00	
15	$2\,HfCl_2(s) + Hf(HCl)Cl(s) \rightleftharpoons 2\,HfCl_2(s) + HfCl(s) + HCl(g)$	0.13	-1.23
16	$3\,HfCl_2(s) + H_2O(g) \rightleftharpoons 2\,HfCl_2(s) + HfCl(s) + H_2O(s) + Cl(g)$	0.00	-1.32
17	$3\,HfCl_2(s) + 2\,H_2O(g) \rightleftharpoons 2\,HfCl_2(s) + Hf(s) + 2\,H_2O(s) + 2\,Cl(g)$	0.00	-1.92

fragments of AlX_2 and AlX are considered beside each other in Fig. 4.3c. The activation energy for proton diffusion from the highlighted OH to AlX_2 is 0.26 eV due to coordination to AlX in its neighbourhood (Table 4.1 reaction 3). The highlighted OH group is 3 coordinated again (excluding. H). Desorption of the last X from AlX is an exothermic reaction in which $E_a = 1.24$ eV is required as activation energy (Table 4.1 reaction 4). Cooperation effect from the neighbouring adsorbate was not observed for the last desorption of X from AlX.

Adsorption of AlX_3 makes the surface OH more acidic. Hence, proton transfers to the ligands, with consequent ligand desorption, are facilitated indirectly through the incoming metal precursors. After first desorption of HX, there is more cooperation between the smaller remaining fragments and oxygen, the c.n. of surface oxygen is increased and the proton diffusion rate to the ligands increases significantly (Fig. 4.1). Therefore, the rate of desorption increases significantly for the second HX due to the cooperative effect. Desorption of the last HX from AlX is relatively difficult, which makes it a less probable reaction at low temperature. Hence, it is most likely that the reactions terminate at an AlX covered

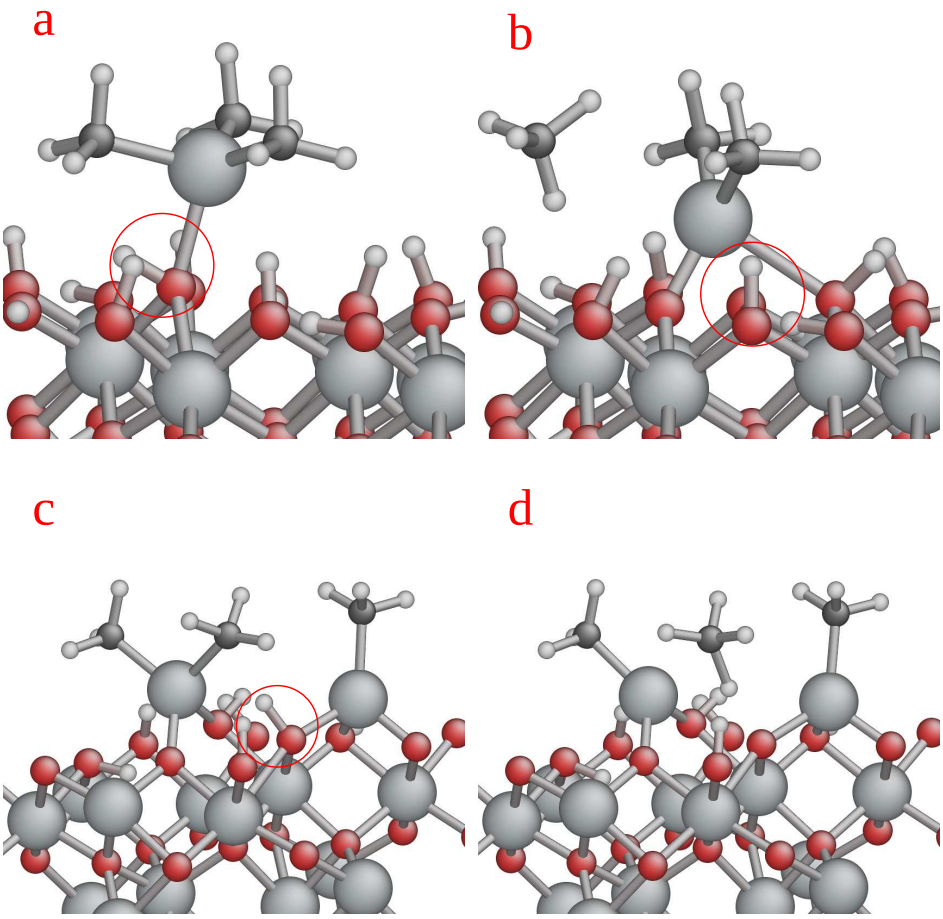


Figure 4.3: Through multiple adsorptions of AlX_3, the surface oxygen becomes coordinatively saturated (Fig. 4.1). The rate of proton diffusion from the saturated oxygen increases and causes the desorption of HX and bonding of the metal of the precursor to the another surface oxygen. (a) Adsorption of AlX_3. Circle shows the OH group to which AlX_3 is anchored. (b) Desorption of HX due to proton transfer from the anchor OH group. Circle shows a low coordinated OH group. (c) Co-existence of remaining precursors, resulting in coordinative saturation of the OH group (circle). (d) Desorption of second HX due to proton diffusion from coordinatively saturated OH group. (red = O, white = H, large gray = Al, small gray = C).

surface.

As mentioned above, the most probable surface species at low temperature at the end of the TMA pulse would be AlX. However, we find that a single AlX cannot dissociate the incoming H_2O molecule during the water pulse (similar to the alkylamide[95]). This seems to be because there are not enough Lewis acid and base sites to dissociate the incoming H_2O molecule. Instead, a surface cluster of 3 AlX in close proximity is considered (Fig. 4.4a). To examine the influence of cooperation between the incoming H_2O molecules on dissociation of remaining HX in the cluster, one and two H_2O molecules are added to the cluster and then

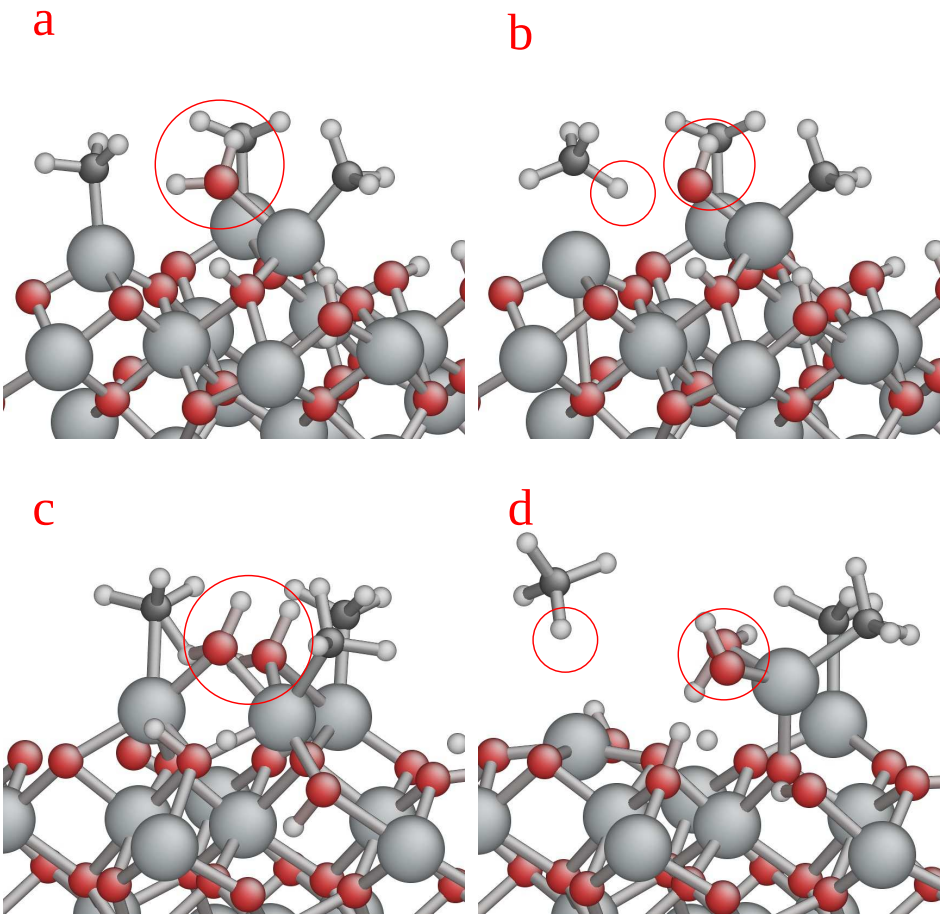


Figure 4.4: Effect of multiple adsorptions of H_2O molecules in the cluster of 3 AlX. By including more H_2O molecules, the proton diffusion and relevant desorption of HX become barrierless (Fig. 4.2). By this process, the remaining ligand is replaced with an OH group. (a) Cluster of 3 AlX. Circle shows an incoming H_2O molecule. (b) Dissociation of the incoming H_2O molecule. Circles show the dissociated parts of the original H_2O molecule. (c) Arrival of two H_2O molecules into the cluster. (d) An H_2O molecule from (c) is barrierlessly dissociated leading to desorption of HX from cluster.

the activation energy for proton diffusion from the incoming H_2O molecule to the carbon of the remaining ligands is calculated.

Fig. 4.4a shows the first incoming H_2O molecule in the oxygen pulse. $E_a = 0.52$ eV is required to take apart the incoming H_2O molecule as it adsorbs (Table 4.1 reaction 5). The proton transfer to the methyl group causes dissociation of the methyl group from AlX immediately (Fig. 4.4b). Alternatively, the arrival of a second H_2O molecule in Fig. 4.4c, makes the activation energy for proton transfer barrierless (Table 4.1 reaction 6). The relevant adsorption and desorption processes are found to be exothermic (Table 4.1 reactions 5 and 6).

Creation of such a cluster (*e.g.* 3 AlX) is a required step for dissociative adsorption of H_2O with consequent methane desorption at low temperature ALD.

The existence of remaining precursor fragments seems to make the surface oxygen near the cluster more Brønsted basic. In this situation at the start of the H_2O pulse, the surface is depleted of protons. Hence, the incoming H_2O molecule can be easily adsorbed and dissociated in the cluster. With arrival of more H_2O molecules the proton transfer barrier decreases, indicating cooperation between H_2O molecules in the oxygen pulse (Fig. 4.2). In other words, the flow of oxygen precursor removes the remaining alkyl in the oxygen pulse and replaces them with OH groups at low temperature. Hence, room temperature ALD of Al_2O_3 from AlX_3/H_2O becomes possible[99] and the surface is left with bulk-like aluminium and oxygen atoms terminated with OH (c.n. = 1 or 2) at the end of oxygen pulse.

4.4 Cooperative effect in growth of HfO_2 from amide precursors and H_2O molecules

ALD reactions for the case of alkylamide are different from the case of alkyl. As shown in section 3.6, desorption of HX (here X=N$(CH_3)_2$) from HfX_4 does not occur through single proton diffusion. Protonated amines can remain bound to the Hf centre. Once multiple proton diffusion from the surface oxygen to the nitrogen of alkylamines occurs, desorption of HX commences. Due to steric repulsion between alkylamide groups, no cooperation between the precursor fragments is observed before densification.

In order to examine the cooperation between the remaining (densified) precursors, we considered two neighbouring HfX_2 (Fig. 4.5a) and compared activation energies for proton diffusion and HX desorption with those for a single HfX_2. The activation energy for proton diffusion from the anchor OH group (bridging oxygen) (Fig. 4.5a) is 0.64 eV (Table 4.1 reaction 7) (Fig. 4.5b). The previously reported value for a single HfX_2 was $E_a = 0.88$ eV (section 3.6). Hence, the presence of another precursor (Fig. 4.1), makes the rate of proton diffusion from the surface oxygen atoms to the nitrogen of the ligands, 3 orders of magnitude larger than previous reported value (using the computed E_a in the Arrhenius equation for 500 K). Hence, the probability of protonation of the remaining ligands is increased. The protonation of alkylamides is an exothermic reaction (*e.g.* -0.2 eV) (chapter 3). In Fig. 4.5d, all nitrogen atoms of the ligands are protonated. The average Hf−N distance changes from 2.0 to 2.4 Å owing to the protonation of ligands. Due to protonation of all ligands and repulsion between the remaining fragments, the activation energy for dissociation of HX from 2 Hf(HX)(HX) is decreased from 0.30 eV (previous reported value, section 3.6) to 0.18 eV (Table 4.1 reaction 8).

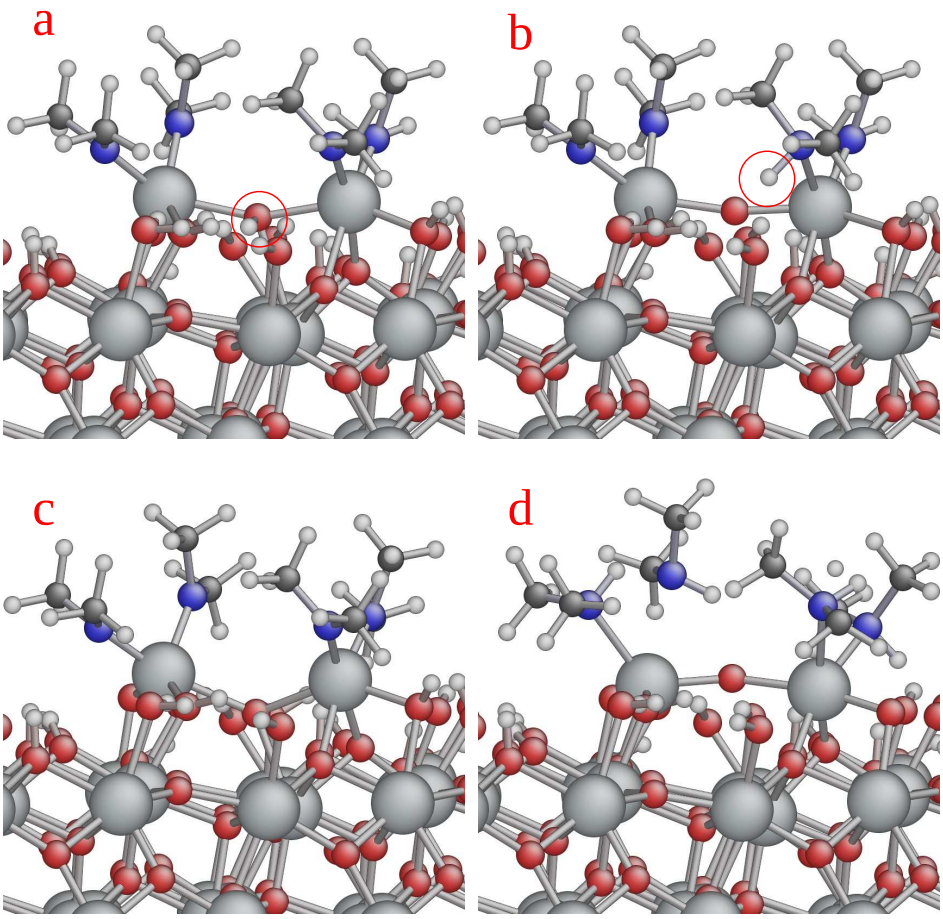


Figure 4.5: Densification of multiple fragments (here $2HfX_2$) beside each other increases the c.n. of shared oxygen (Fig. 4.1). The rate of proton diffusion from coordinatively saturated oxygen increases significantly. Due to repulsion between the remaining ligands, the rate of desorption of HX is also increased. (a) Remaining of two HfX_2 precursors. Circle shows coordinatively saturated OH group. (b) Proton transfer of coordinatively saturated OH group (a) to the remaining ligand. Circle shows proton. (c) $2\,HfX_2$ together. (d) Repulsion between densified precursors from (c) increases the desorption of protonated ligands. (red = O, blue = N, white = H, large gray = Hf, small gray = C).

The more densification of the remaining precursor fragments to the surface oxygen, the better proton diffusion to the remaining precursors occurs. In other words, densification of the remaining precursor fragments to the surface makes OH more acidic (chapter 3). Therefore, the involved surface oxygen atoms in the cluster release protons which diffuse to the remaining ligands. In addition to increasing the rate of proton diffusion through densification, repulsion between the remaining ligands in the case of $(2\,HfX_2)$ makes the ligands more basic than a single HfX_2. Therefore, proton diffusion and ligand desorption are facilitated through the steric repulsion between the remaining ligands.

As seen before (chapter 3)), HfX is the most probable species in the Hf pulse

energetically and statistically. The last desorption of HX from a single HfX is endothermic with activation energy of 1.64 eV (Table 4.1 reaction 9). Similar to alkyl precursor, cooperation effect from the neighbouring adsorbate was not observed for the last desorption of alkylamide from HfX. To examine the cooperation between the remaining ligands to dissociate an incoming H_2O molecule in the oxygen pulse, we considered 4 HfX as a typical example of the remaining ligands from the metal pulse (Fig. 4.6a). The first H_2O molecule arriving into the cluster is easily dissociated by proton transfer to the neighbouring basic atoms (nitrogen here) (Fig. 4.6b) and this dissociation is barrierless (Table 4.1 reaction 10). Through the introduction of more H_2O molecules into the cluster (Fig. 4.6c), Hf of the remaining precursor obtains a higher c.n. from the oxygen of the incoming H_2O molecules (Fig. 4.6d). In this situation, dissociation of the last ligand HX becomes exothermic. The activation energy of the last HX desorption is then 0.56 eV (Table 4.1 reaction 11).

After densification of the remaining alkylamide precursor fragments, owing to the depletion of surface of protons and repulsion between the remaining ligands, the incoming H_2O molecule is readily adsorbed and dissociated. The surface oxygen atoms involved in the (4 (HfX)) cluster are stronger basic sites than those near a single HfX and the nitrogen atoms of ligands in the cluster are stronger basic sites than those of a single HfX. The cooperation between the remaining ligands of the metal precursor and the incoming H_2O molecules causes a drop in the activation energy of HX desorption (Fig. 4.2). The corresponding reactions of proton diffusion to the alkylamide precursor and ligand desorption as HX show a low barrier (and are exothermic) (Table 4.1 reactions 10 and 11), which makes it possible to achieve ALD for HfO_2 from HfX_4 and H_2O at low temperature.[25] Hence, the remaining alkylamines are replaced with OH groups and the surface is left with the bulk-like hafnium and oxygen atoms and an OH-termination (c.n. = 1 or 2) at the end of the oxygen pulse.

4.5 Cooperative effect in growth of HfO_2 from halide precursors and H_2O molecules

So far, computed ALD reactions from halide precursors have been reported to be endothermic.[30] In other words, no intrinsic driving force for the growth reaction has been obtained. As reported before,[30] adsorption of the hafnium chloride precursor is energetically favorable. Our calculations show that after adsorption of $HfCl_4$ the surface protons do not diffuse to the chloride of adsorbed precursor, because there are large barriers ($E_a \geq 1.0$ eV). Therefore, we suppose that the

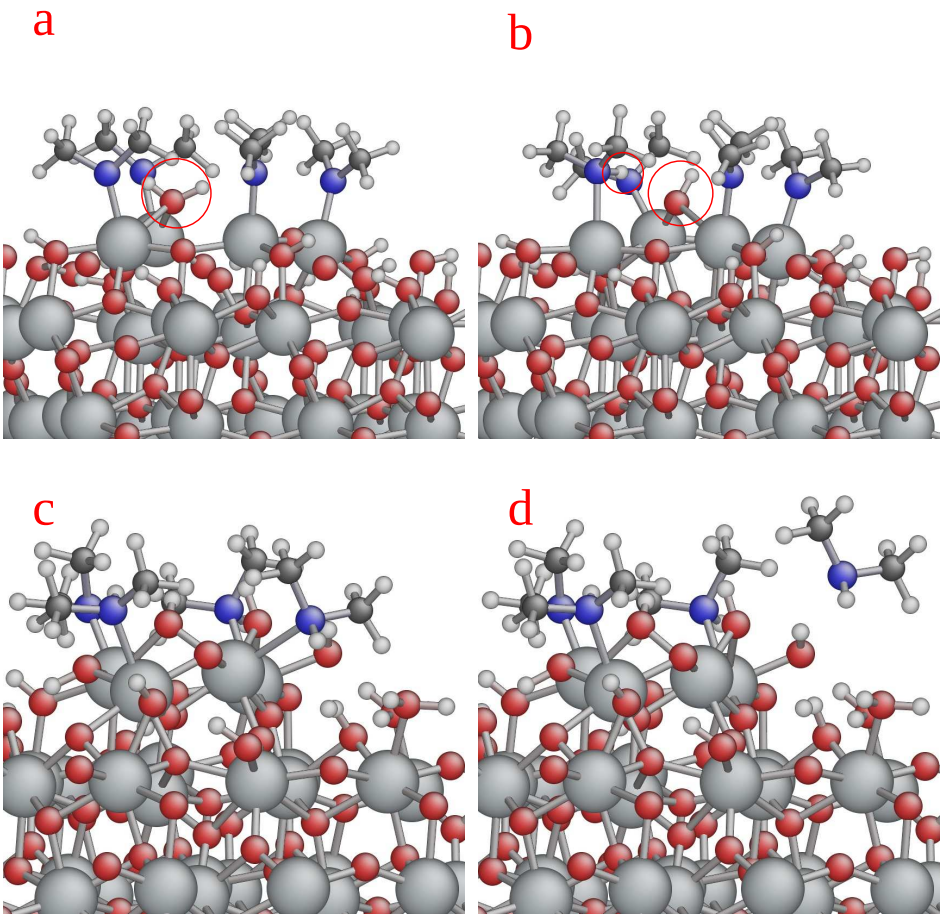


Figure 4.6: The incoming H_2O molecule is readily dissociated in the cluster of remaining precursor (here 4 HfX). Due to multiple adsorptions of H_2O molecules, dissociation of the remaining ligands becomes energetically possible (Fig. 4.2). (a) Cluster of 4 HfX. Circle shows an incoming H_2O molecule. (b) The incoming H_2O molecule is barrierlessly dissociated. (c) Multiple adsorptions of H_2O molecules into the cluster. (d) Desorption of the remaining ligands is facilitated through multiple adsorptions of H_2O molecules.

intact $HfCl_4$ molecule can be the energetically favorable surface species at the end of the metal precursor pulse.

At the beginning, a dative chemical bond between the hafnium of the adsorbing $HfCl_4$ precursor and a surface oxygen atom is created.[30] Once the surface is covered by a monolayer of halide precursors, creation of chemical bonds between the surface oxygen and the metal of the precursor is stopped. However, we observe in simulation that the presence of other $HfCl_4$ allows further adsorption of $HfCl_4$ through the creation of Hf−Cl−Hf bridges, so that chains of $HfCl_4$ are made at the surface. This results in multiple mono-layers of adsorbate that are physically and chemically bonded to each other and to the surface. In this situation, we expect that the number of layers depends on the ALD temperature: since many adsorbates are physisorbed at the top layers, increasing temperature cause them

to desorb. Hence, a lower growth rate can be expected at high temperature,[24] while at low temperature, growth may not be self-limiting.

We therefore investigate the H_2O pulse. In order to examine the effect of cooperation between the incoming H_2O molecules on desorption of remaining ligands from $HfCl_4$ clusters, we considered 4 $HfCl_4$ adsorbed beside each other and continued adsorption and optimization of H_2O molecules one by one. Initially, a chain of $HfCl_4$ at the surface linked by bridging chloride is observed (Fig. 4.7a). The adsorption of the first H_2O molecule into the cluster of $HfCl_4$ is shown in Fig. 4.7b. The oxygen of the incoming H_2O molecule bonds to one hafnium atom of the precursors. At the beginning, no evidence of H_2O dissociation or HCl desorption is observed. However, with the arrival of more H_2O molecules into the cluster (*e.g.* here 5 H_2O molecules, Fig. 4.7c), spontaneous proton diffusion to the chloride is observed (Fig. 4.7d). Adsorption of a H_2O molecule becomes exothermic for the fifth adsorption (-1.14 eV, Table 4.1 reaction 12).

With the start of the H_2O pulse, dissociation of HCl commences. The transferred protons come from the incoming H_2O molecules. Owing to the cooperation between the adsorbed H_2O molecules and proton diffusion to the chloride, ligand desorption becomes barrierless and exothermic in strong contrast to the $HfCl_4$ pulse. As mentioned above, low temperature ALD of halides results in several layers of adsorbate during the metal pulse. In low temperature ALD therefore, the by-product HCl may be buried in the growing layers and this may cause chlorine contamination and/or etching in the films.[24] The physisorbed layers of $HfCl_4$ at high temperature are probably thinner than at low temperature. Hence, the by-product HCl can be more easily desorbed at high temperature and less contamination is observed.[24]

After the first HCl desorption, the remaining halide precursor $HfCl_3$ is not densified into the surface (Fig. 4.7d). In a simple model, in which only a single $HfCl_3$ is considered at the surface, the reported activation energy for second HCl desorption is high and the reaction is endothermic.[30]

In order to check the effect of cooperation between the remaining precursor fragments on ligand desorption and the effect of bridging oxygen, clusters of 2 $HfCl_3$ and 3 $HfCl_2$ are considered separately. Bridging oxygen either from the oxygen precursor or from the surface allows the hafnium of the metal precursor to obtain higher c.n.. In the 2 $HfCl_3$ cluster, bridging Cl is observed again (Fig. 4.8a) and a Hf−Cl bond is broken (4.2 Å) from the cluster, probably due to the steric effect (repulsion between Cl). The highlighted proton in Fig. 4.8a requires 0.46 eV as activation energy to diffuse to the detached Cl (Fig. 4.8b). The second HCl desorption in the above situation is exothermic (Table 4.1 reaction 13). Similarly, 3 $HfCl_2$ are also considered beside each other (Fig. 4.8c). In this cluster, because

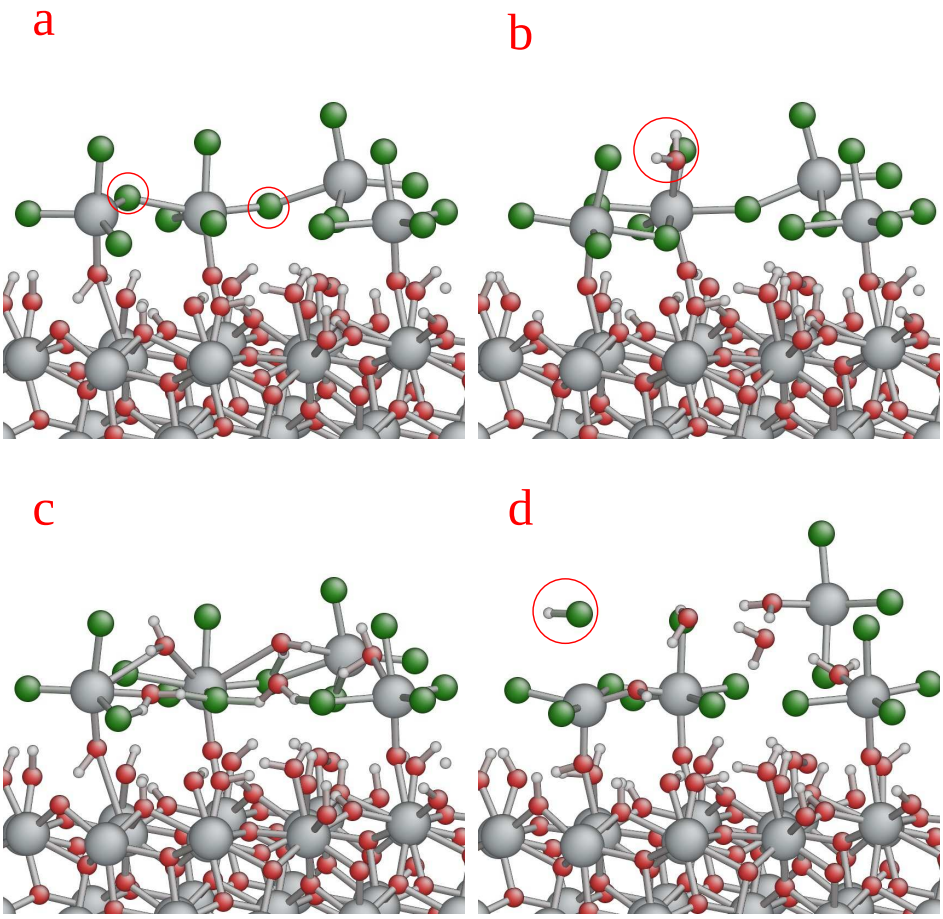


Figure 4.7: Considering the multiple adsorptions of $HfCl_4$ and H_2O molecules, the relevant activation energies for proton diffusion and dissociative reactions decrease significantly. (a) Chemisorption and physisorption of multiple precursors (here 4 $HfCl_4$) due to the bonding to the surface oxygen and bridging chloride. Circles show bridging Cl. (b) An incoming H_2O molecule adsorbing into the cluster. (c) Multiple adsorptions of H_2O molecules into the cluster. (d) Dissociation of the H_2O molecules and desorption of HCl. Circle shows the desorbed HCl. (red = O, green = Cl, white = H, large gray = Hf).

the highlighted oxygen is fully coordinated to Hf (c.n. = 3), it readily donates its proton. Hence proton diffusion to the chloride is barrierless (Fig. 4.8d) (Table 4.1 reaction 14). The activation energy for a third HCl desorption is also very low, at 0.13 eV (Table 4.1 reaction 15).

To model the effect of cooperation between the incoming H_2O molecules on the remaining ligands in the clusters of 2 $HfCl_3$ and 3 $HfCl_2$, H_2O molecules are added one by one to both clusters. For both clusters, the incoming H_2O molecule is replaced by the remaining Cl similar to Fig. 4.8a. Hf−Cl distance in both clusters is stretched (DFT calculations) and similar proton diffusion from highly coordinated oxygen is expected. The relevant chemical reactions are exothermic (Table 4.1 reactions 16 and 17).

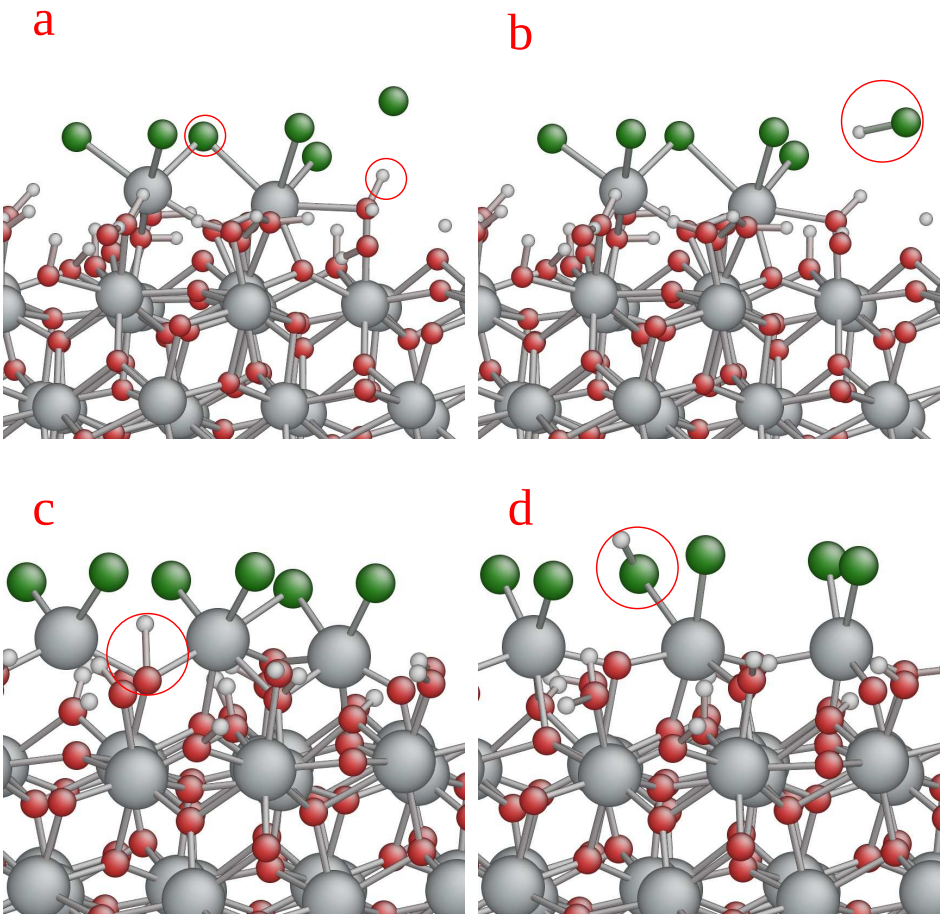


Figure 4.8: Proton diffusion from the coordinatively saturated oxygen to the remaining chloride in the clusters. These oxygen atoms can be either from the oxygen pulse (H_2O) or from the surface. (a) $2\,HfCl_3$ cluster. Circles show bridging Cl and surface proton. (b) Proton transfer from surface to detached Cl leading to desorption of HCl. Circle shows the desorbed HCl. (c) $3\,HfCl_2$ cluster. Circle shows the coordinatively saturated OH group. (d) Proton diffusion from the OH group to the remaining Cl.

Dissociation of HCl from the remaining chloride fragments (*e.g.* $HfCl_3$ and $HfCl_2$) is only possible once the hafnium becomes fully coordinated (5 or 6 coordinated). At the same time, the surface oxygen or the incoming oxygen precursor should also be fully coordinated in order to release protons for transfer to the remaining chloride. These two conditions are not frequently fulfilled during the $HfCl_4$ pulse, and so adsorbates like $HfCl_4$ and $HfCl_3$ predominate in the metal pulse. Including the cooperative effect, the calculated activation energies are lower than in the simple model and the reactions are exothermic. In the complicated models that consider cooperation between adsorbates, the surface OH are seen to become more acidic and the remaining ligands (halides) more basic (Fig. 4.1). In such circumstances, the rate of proton transfer from the coordinatively saturated OH group to the chloride increases. Hence, the remaining chlorides

are replaced with OH groups and the surface is left with bulk-like hafnium and oxygen atoms and an OH-termination (c.n. = 1 or 2) at the end of oxygen pulse.

4.6 Summary

In summary, our first-principles calculations of activation energies in different local environments show that co-adsorption of metal precursors makes the surface oxygen coordinatively saturated. Hence, the rate of proton diffusion from the surface oxygen to the remaining ligands increases significantly and causes desorption of the ligands. The same scenario is observed during the oxygen pulse. Co-adsorption of the oxygen precursors in a cluster of the remaining precursors makes the metal atoms of the precursors coordinatively saturated. Therefore, further desorption of the ligands occurs and the surface is left with bulk-like metal and oxygen atoms and the coordinated (c.n. = 1 or 2) OH groups at the end of oxygen pulse.

Chapter 5

Implementation of kinetic Monte-Carlo

To describe the ALD reactions of HfO_2 from $Hf(N(CH_3)_2)_4$ and H_2O, a 3D on-lattice KMC model is developed. The scope of this chapter is to detail the implementation of the results obtained from DFT into this model. In this model, all atomistic reaction pathways in DFT are implemented as reaction events on the lattice. This contains all steps (chapter 3), from the early stage of adsorption of each ALD precursor, kinetics of the surface protons, interaction between the remaining precursors (steric effect), influence of remaining fragments on adsorption sites (blocking), densification of each ALD precursor, migration of each ALD precursors, and cooperation between the remaining precursors to adsorb H_2O (co-operative effect).[95] The essential chemistry of the ALD reactions depends on the local environment at the surface. The c.n. and a neighbour list are used to implement these dependencies. The migration of the low coordinated remaining precursor fragments is also proposed. This process introduces a slow re-ordering motion ('crawling') at the mesoscale, leading to the smooth and conformal thin film that is characteristic of ALD.

5.1 Lattice site

In order to track the surface evolution and film morphology, a lattice based KMC method is used. The lattice can in principle be two or three dimensional. Tracking in three dimensions is much more difficult than in two dimensions due to the far greater topological complexity. However, to accurately translate the chemistry in the atomic scale to the mesoscale for ALD, three dimensional tracking is deemed necessary. The capability to describe the system in 3D makes modern KMC a powerful tool to explain both reaction kinetics and film morphology. The two

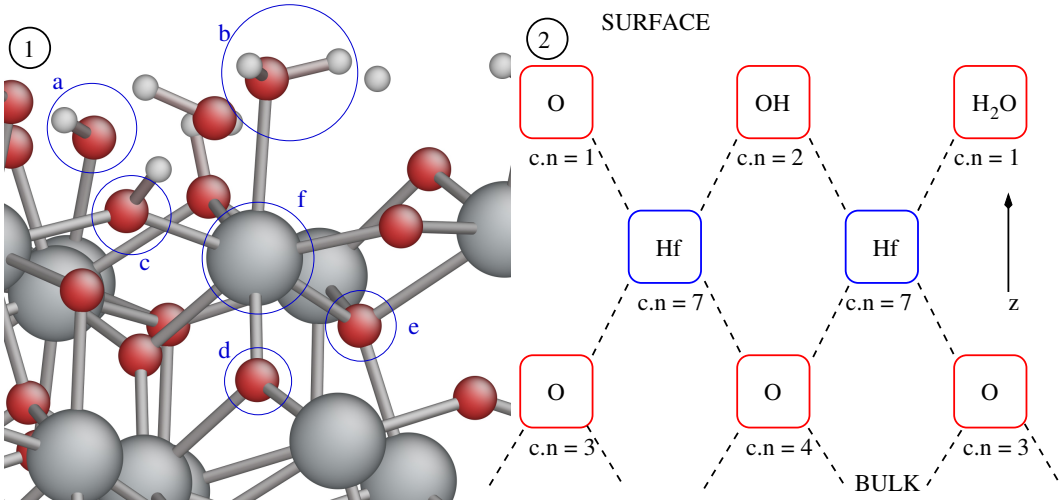


Figure 5.1: (1) DFT optimized surface structure of hydroxylated HfO_2 (section 3.3). Terminal hydroxyl group (a), terminal adsorbed water (b), bridging hydroxyl (c), 3 coordinated oxygen (d), 4 coordinated oxygen (e), and 7 coordinated hafnium (f) are highlighted. (Red = O, White = H, large grey = Hf). (2) Schematic two dimensional diagram illustrating mapping of the same surface structure. Blue and red boxes show the cation and anion sites respectively. The dashed lines show the connection between sites in this two dimensional diagram but the actual c.n. in three dimensions is also given.

precursors considered in this study are $Hf(N(CH_3)_2)_4$ and H_2O. In this section, the ligand $N(CH_3)_2$ is referred to as X for simplicity.

The lattice sites are defined based on monoclinic HfO_2 (space group $P2_1/c$)[116] as this is the most stable crystalline structure of the oxide after deposition and annealing. The three-dimensional lattice sites are occupied by either Hf or O atoms during the ALD simulation. In the monoclinic structure, every site of the cation sublattice is surrounded by seven anion sites and every site of the anion sublattice is surrounded by three or four cation sites (Fig. 5.1). Based on the counted number of first neighbour atoms of a cation or anion, the c.n. is defined. Every cation or anion site can have a c.n. ranging from 0 up to 7 or 4 respectively. We exclude bonds to H when quoting the c.n. of O.

The crystallographic directions <111> define the x, y, and z axes of the coordinate system. Periodicity is imposed in x and y but not in z. Two smooth layers of fixed oxygen and hydroxyl in the x-y plane are considered as the substrate in this example. The first cycle starts with a HfX_4 pulse. The crystal growth is then in the $+z$ direction. Each lattice site is associated with three variables describing the state of this site.

-The first variable contains the information regarding the chemical configuration of the site. This variable is updated frequently during the KMC simulation.

-Each lattice site also has a neighbour list that carries the information about the local bonding. Local bonding indicates which site is connected to which site and this assists in defining the reaction events in KMC. Structural relaxation, cooperative reactions and steric hindrance are implemented using the neighbour list.

-Finally, each lattice site is associated with a discrete variable describing the c.n. of the site. This variable, together with the neighbour list, allows us to implement the complicated chemistry at the surface. For instance, by densification of the hafnium atom of the precursor to the surface, the c.n. of the cation site changes from 3 to 8.

5.2 Pulse time and purge time

In the ALD process, gaseous precursors are admitted to the reactor in alternate pulses separated by periods of purging. To implement this in KMC, the respective adsorption reactions are turned on and off as simulation time advances. Adsorption reactions of the two precursors occur alternately as time progresses. During the purge, no adsorption reaction are allowed.

5.3 Event type

In our KMC model, reaction events are defined and used to implement the chemistry of ALD obtained from DFT calculations (chapter 3). For every position, geometry optimization was carried out by DFT calculations. The minima obtained from the DFT calculations are mapped onto the lattice sites for the subsequent KMC calculations. The events taking place within the KMC calculation modify the chemical occupation of the sites. This corresponds to the transition of the system from one minimum to another in the DFT calculation. The frequency of an event is derived using Eq. 2.23 from an activation energy obtained from NEB[122] calculation with DFT.

We consider that three types of events occur, each with different dependencies on neighbours. Here, the site under consideration is specified by $\square^{(0)}$. The first and second neighbours of the involved site are identified by $\square^{(1)}$ and $\square^{(2)}$ respectively. The occupation of the first or second neighbour site may also change as a result of an event at $\square^{(0)}$.

-type α

This type of event only changes the occupation of a single site. The event is dependent on the c.n. at that site and on the pulse/purge stage of the

ALD cycle. For instance, $OH^{(0)} \longrightarrow OH{-}HfX_4^{(0)}$ only occurs for the hydroxyl group with a c.n. of oxygen = 1 (excluding H) during the hafnium precursor pulse. The possibility of adsorption occupation during the metal pulse therefore is limited to the anion site with OH.

-type β

This event modifies the occupation of a site $\square^{(0)}$ and the second neighbour of this site $\square^{(2)}$. Clearly, the possibility of this event occurring depends on the characteristics of the site and on those of its second neighbour. As with type α, events, there can be a dependence on the c.n. and on the pulse/purge stage of the ALD cycle. For example, consider an adsorbate site as an anion site occupied with adsorbed HfX_4, whose first and second neighbours are cation and anion sites respectively. Then the event $[OH{-}HfX_4]^{(0)} + OH^{(2)} \longrightarrow [OH{-}Hf(HX)X_3]^{(0)} + O^{(2)}$ only occurs when there is a proton $OH^{(2)}$ in the second neighbour of the adsorbate site.

-type γ

This event type changes the occupation of a site and of its first neighbour. For instance, $[OH{-}HfX_2]^{(0)} + VAC^{(1)} \longrightarrow OH^{(0)} + HfX_2^{(1)}$ shows the motion of a hafnium precursor fragment to an adjacent vacant cation site. In this case, the event changes the occupation of the adsorbate site $\square^{(0)}$ (anion sublattice) and the vacancy site $\square^{(1)}$ (cation sublattice). Following an event of this type, the c.n.'s of both adsorbate and vacancy sites must be updated.

In the following discussion, the atomic-scale chemistry of the surface determined[95] from DFT (chapter 3) is translated into discrete events in order to describe the KMC simulation in more detail.

5.4 Hf precursor adsorption

Molecular HfX_4 chemisorption takes place with a probability given by Eq. 2.26. There are three criteria that adsorption sites of HfX_4 must satisfy as outlined below.

-Firstly, DFT calculations (section 3.4) have shown that the adsorption sites are singly-coordinated oxygen and hydroxyl groups ($\square^{(0)}$ = O or OH with c.n. = 1). In other words, the bridging oxygen and crystalline oxygen with c.n. > 1 are unsuitable for adsorption.

-Secondly, the adsorption sites can be blocked due to the remaining X at neighbouring sites. There are different rules for remaining ligands of HfX_4, HfX_3, HfX_2, and HfX as discussed in section 5.11.

-Thirdly, the adsorption sites can be blocked due to O at neighbouring sites. As anion sites are occupied by oxygen during the oxygen pulse, low coordinated O or OH (c.n. = 1) in the sub-layers become inaccessible to the precursor metal. To prevent adsorption at these sites, the number of oxygen atoms occupying second neighbours of the relevant oxygen site are counted. If this number is greater than 4/5 of the total sites, then the relevant site is blocked. This process only happens during the Hf pulse.

If all sites are occupied or blocked, the incident hafnium precursors are assumed to be reflected back to the gas phase. (i.e. $S_{\mathrm{n,B}}$=0).

5.5 HfX_4 desorption

The reverse of HfX_4 adsorption is desorption. As with adsorption, the desorption event is of type α. Neighbouring sites are unblocked via desorption of HfX_4. In our KMC calculation, desorption of charged precursor fragments like $[HfX_3]^+$ or intermediates like $[Hf(HX)X_3]^+$ is not allowed.

5.6 Proton diffusion

In our KMC model, various types of proton diffusion are defined. There is a strong correlation between these diffusion events and other reactions. For example, the ready availability of protons contributes to the facile elimination of ligands. Increased eliminations during the metal pulse is expected to lead to a higher rate of growth.[128] As one of the aims of this model is to judge exactly how the rate of growth is affected by these diffusion events, they are sorted into four types below.

-Proton diffusion from oxygen to oxygen

Proton diffusion from oxygen to oxygen is the reaction that allows mobility of protons across the surface. The c.n. of oxygen (at an anion site) is employed to distinguish between the proton diffusion barriers. DFT calculations show that it is energetically favorable for protons to move from high c.n. oxygen to low c.n. oxygen. Hence, under-coordinated oxygen (with c.n. = 1 or 2) are the Brønsted basic sites that are actively involved in proton diffusion. A one coordinated oxygen is a hyperactive site. It spontaneously decomposes a neighbouring H_2O molecule (type β) or takes a proton from a higher coordinated oxygen (c.n. $\geq$ 2). According to DFT calculations, both of these reactions are barrierless. A two coordinated oxygen is less active than a one coordinated oxygen. The two coordinated oxygen faces

a large barrier to taking a proton from a neighbouring oxygen (c.n. = 1). After depletion of protons at the surface due to desorption as HX, some oxygen atoms acquire a higher c.n. due to densification, while the other oxygen atoms acquire a reduced c.n. and become more Brønsted basic. These latter under-coordinated oxygen undergo a form of proton diffusion from oxygen to oxygen with the same c.n. A 0.75 eV barrier for these 1 or 2 coordinated oxygen atoms is obtained by DFT .

-Proton diffusion from oxygen to ligand nitrogen (from anion to anion site)

The other type of proton diffusion is from the surface oxygen to the nitrogen of the precursor and its reverse. In the case of alkylamide it has been shown that there are stable geometries with a proton bound to the nitrogen. The formation of HX in this manner is necessary prior to ligand elimination by desorption of HX (section 3.6). However, the activation energy strongly depends on the distance between N and O. If we suppose that $HfX_4^{(0)}$ is anchored to an $OH^{(0)}$ group at the surface (type α), the most accessible proton for hopping to the $N^{(0)}$ of the precursor is not the anchor $OH^{(0)}$, but rather the second neighbour protons ($OH^{(2)}$), because the $N^{(0)}-O^{(2)}$ distance is shorter. The activation energies for proton diffusion from the surface oxygen to the nitrogen of the ligand and its reverse range from 0.05 to 0.30 eV. To map this proton hopping behaviour into KMC, type β events are introduced that change the occupation of the site and its second neighbour.

In comparison to the barrier to rotation for the protonated ligand discussed in section 5.7, diffusion of the proton from nitrogen back to the oxygen has a lower barrier. This means that proton diffusion between the surface oxygen and the nitrogen and its reverse is much faster than rotation of the protonated ligand. The most likely events which occur are low barrier events. Hence, the KMC simulation advances extremely slowly, especially considering that the sum of probabilities is over a large number of sites, giving a total rate that is enormously large (superbasin, subsection 2.2.3). To overcome this difficulty, we propose that only the presence of a proton on surface oxygen is necessary for protonation and rotation of the ligand. In other words, we remove (filter) proton diffusion from the surface oxygen to the nitrogen and its reverse from the reaction list. Otherwise the realistic ALD time would be inaccessible to the current KMC simulation. A side-effect of this is that the absolute time taken for growth is shorter in the simulation than the realistic ALD time.

-Proton diffusion from oxygen to nitrogen (from anion to cation site)

This diffusion describes proton hopping from oxygen ($\square^{(0)}$) to the first neighbour nitrogen of the densified precursor ($\square^{(1)}$) which is explained in section 5.9. This diffusion occurs from the anion site to the cation site (type γ).

-Proton diffusion from nitrogen to nitrogen

Proton diffusion within the adsorbed precursor consists of proton hopping from nitrogen near the surface to the topmost nitrogen of the precursor. This diffusion is of type α.

In this calculation, no particular ligand orientation for proton diffusion is considered.

5.7 Rotation of the protonated ligand

After diffusion of a proton from the surface oxygen to the ligand nitrogen, there is a second reaction that facilitates elimination of HX, namely rotation of the protonated ligand. Activation energies of 0.42 to 0.51 eV are calculated for the rotation of alkylamide ligand (section 3.5). To implement this reaction in combination with proton diffusion from the surface oxygen to the nitrogen, event type β is used.

5.8 Elimination of the ligand

It is commonly assumed that protonated ligands (HX) rapidly desorb following proton transfer from the surface to the remaining fragment during ALD.[129] However, we have shown (section 3.6) that further proton transfer to the remaining fragment before desorption facilitates the ligand elimination. For instance, the activation energy for desorption of the first HX after the first protonation and rotation is 0.89 eV. This energy decreases to 0.39 eV after the second protonation. A third protonation allows spontaneous desorption ($E_a = 0$ eV) of two HX and densification of the metal precursor. In order to map the desorption of HX into the KMC model, the occupation of a single site is modified (type α). Neighbouring sites have no direct influence on the desorption event. The last HX desorption from the Hf precursor is an endothermic reaction. Such an event takes place only if either of the following occurs:

- The Hf of the precursor is densified into an empty cation site surrounded by at least 6 oxygen atoms; in other words, an empty site in the subsurface layer.

- The c.n. of Hf of the precursor is increased by adsorption of H_2O during the oxygen pulse, as explained later (section 5.13).

5.9 Densification of HfX_2

Ab initio MD calculations show that after elimination of two ligands from the adsorbed HfX_4, the Hf atom of the remaining HfX_2 fragment becomes strongly bonded to nearby under coordinated oxygen at the surface (section 3.6). This structural relaxation is termed "densification" and is implemented in the KMC model as event type γ with a small barrier (0.2 eV). The $O-HfX_2^{(0)}$ remnant moves from the anion site where it was adsorbed to one of the neighbouring cation sites $\square^{(1)}$ where the Hf belongs (Fig. 5.2). To implement densification in the KMC simulation, the c.n. of the anion and cation sites involved in densification are modified. As mentioned above, every site $\square^{(0)}$ of the anion sublattice is connected to 2 or 3 cation sites $\square^{(1)}$ at the surface. To determine which cation site is chosen, a random procedure is employed, which is not strictly correct. The correct dependence on c.n. is included via the migration process (see section 5.10).

The hafnium should finally become densified to the cation site that has highest c.n. to surface oxygen. In other words, the higher the number of Brønsted base sites, the stronger the attraction applied to the hafnium. For instance, in Fig. 5.2 the five-coordinated empty site exerts a stronger attraction to the hafnium than the empty two coordinated site. Therefore, the hafnium of the precursor should densify to the cation site with a higher c.n. rather than moving randomly. This tendency will be included using the migration process (section 5.10).

Typically hafnium, together with the remaining fragments, forms three or four bonds to the smooth surface following densification (Fig. 5.7). In this case, densification is highly exothermic ($\Delta G \leq$ -4 eV) and an enormous activation energy is needed for the reverse reaction. Also densification into the sub-layers (filling gaps in a rough surface) is expected to be even more exothermic than on a smooth surface. This means that a huge amount of energy is needed to detach the hafnium (with the remaining precursor) from 3 or 4 oxygen atoms, which is not possible energetically in the ALD process. Hence, the reversal of densification is neglected in our calculation.

5.10 Migration of HfX_2

In our KMC model, densification happens all over the surface. It may happen into the sub-layer, in which case a high c.n. for Hf to previously under-coordinated

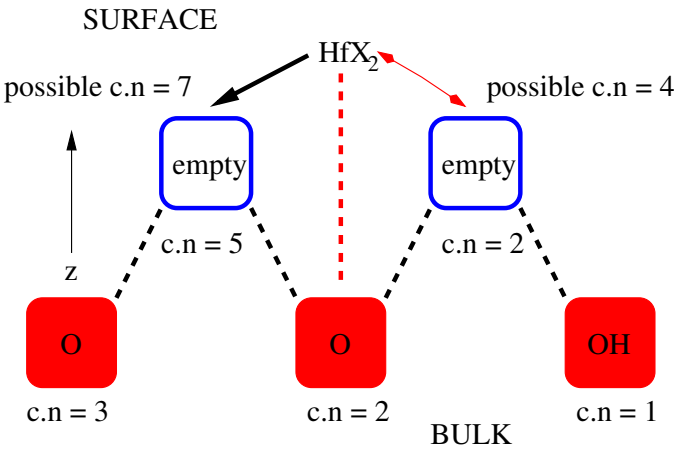


Figure 5.2: Schematic diagram of densification of HfX_2 into empty cation sites. The presence of more under-coordinated oxygen around the left-hand cation site applies speculatively a stronger attractive force on the HfX_2 adsorbate than that at the right-hand site. The thicker black arrow indicates the stronger attraction where reverse densification is impossible. Red arrows show migration process. (Same scheme as Fig. 5.1).

oxygen is obtained, or it may happen by reorganisation of bonding at the smooth surface, typically leading to a Hf c.n. of 3 or 4 from the under-coordinated oxygen. In the cases discussed earlier (section 5.9 and 3.6), hafnium with its remaining ligands has a total c.n. of 5 at least. However, densification may also happen when there is a low population of surface oxygen (Fig. 5.3). In this case, the hafnium is not coordinatively saturated. For instance, if HfX_2 contains two bonds due to the bonding to the surface oxygen, it has total c.n. of 4. In this situation, DFT calculations show that the hafnium of the precursor keeps its two ligands and no HX desorption has been seen, since the activation energy is high. The mobility of this 4-coordinated HfX_2 has been seen during ab initio MD (section 3.6, Fig. 3.9).

The migration process is only defined for 3 or 4 coordinated HfX_2 ($E_a = 0.40$ and 0.50 eV respectively). In this picture, a $HfX_2^{(0)}$ fragment that has migrated to a cation site, can come back to an oxygen atom $O^{(1)}$ at an anion site. The reverse can also take place ($O{-}HfX_2^{(0)}$ anion site to $\square^{(1)}$ cation site) as shown in Fig. 5.3. In this situation, migration events continue until the metal of the precursor becomes 5 or more coordinated in total. For instance, if HfX_2 does densify into possible sites with c.n.= 5 or 7 (section 5.3), the hafnium atom remains pinned at this cation site. No reverse migration is then possible any more. In this manner, any concerns regarding the occurrence of random densification in the low coordinated cation site are addressed.

Migration combines with the processes of random densification to introduce a slow motion of Hf fragments over the low coordinated anion sites of the oxygen-

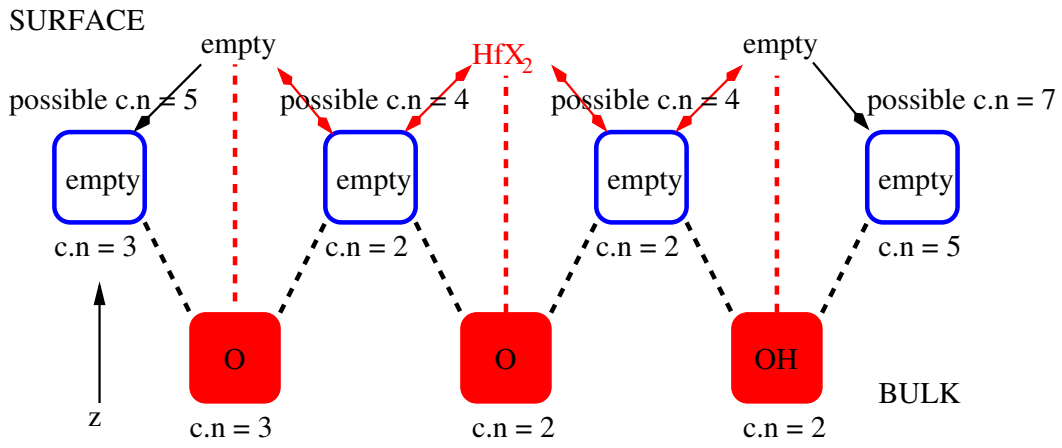


Figure 5.3: Schematic diagram of densification and migration of HfO_2 (Same scheme as Fig. 5.1). Black arrows show potential densification where reverse densification is impossible. Red arrows show migration process. The migration process occurs until a c.n. greater than 2 is obtained by hafnium of the precursor.

covered surface. We call this motion "crawling". The precursor fragment crawls over areas with a low population of surface oxygen until the hafnium of the precursor finds a site that is abundant in oxygen and thus obtains a high enough c.n. from the surface oxygen. This mechanism allows sub-surface vacancies to be filled. Our tests show that this mechanism has a profound effect on film growth in KMC (subsection 6.1.2).

5.11 Steric effect

The metal cation in the precursor molecule is surrounded by ligands that are often large, as in the current case of $X = N(CH_3)_2$. These ligands take up substantial space at the surface when the precursor molecule or its fragments are adsorbed. Many potential adsorption sites around such a fragment therefore lose their capability to adsorb further precursors. This steric effect is obviously an important consideration, which affects the rate of ALD growth and the statistics of the different configurations in the KMC calculation. In order to model the interactions between the remaining fragments of the precursors, and their secondary influence on the adsorption sites, DFT calculations are employed. Fig. 5.4 shows the optimized structure of two neighbouring HfX_3 precursors at the surface, where both are anchored to under-coordinated oxygen at the surface. The distance between the hafnium atoms of the fragments is 8.4 Å. Optimizing the geometry from other adsorption sites for HfX_3, no shorter Hf−Hf distance could be obtained, so this may be viewed as a minimum value. The sites where closer approach was impossible (the highlighted oxygen atoms in Fig. 5.4) have

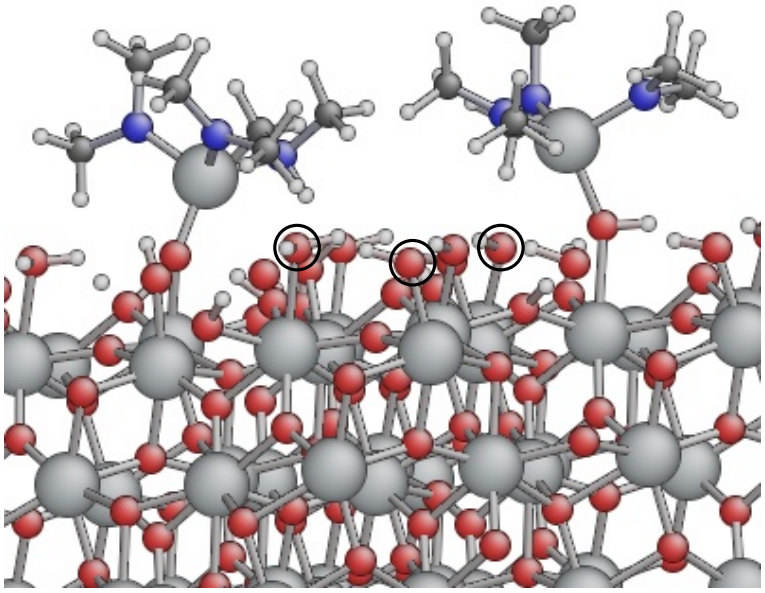


Figure 5.4: Steric hindrance between two HfX_3 from DFT calculation. Steric hindrance leads to a change in the adsorption pattern of the precursors in ALD. Some of the blocked sites are highlighted with circles indicating that they are unable to adsorb the next Hf precursor. (Red = O, White = H, large grey = Hf, dark grey = C, and blue = N).

therefore temporarily lost their ability to adsorb another precursor molecule. We term this process 'blocking'.

To implement this blocking at the surface, the neighbour list of the site is used. Following adsorption of HfX_4 at the $OH^{(0)}$ (c.n. = 1) site, the relevant neighbouring anion sites (the second neighbours $\square^{(2)}$ and fourth neighbours $\square^{(4)}$) are flagged as blocked and drop out from the reaction list for adsorption (Fig. 5.5). Similar blocking of $\square^{(2)}$ and $\square^{(4)}$ is also applied when fragments of precursors remain, namely $HfX_3^{(0)}$ and $HfX_2^{(0)}$ before densification. Implementation of blocking after densification is slightly different, as now $HfX_2^{(0)}$ is on a cation site. The neighbouring anion sites that it blocks are $\square^{(1)}$ and $\square^{(3)}$ (see Fig. 5.6).

The other potential steric effect is the blocking of Hf fragments from densifying at cation sites, due to the existence of fragments at adjacent sites. When hafnium, together with the remaining ligands, is densified to a cation site $\square^{(0)}$, it might prevent further densification in the neighbouring cation sites $\square^{(2)}$. However, DFT calculations show that densification of such fragments to adjacent cation sites is possible. Fig. 5.7 shows three neighbouring HfX_2 in which ligands are aligned with each other. The distance between Hf−Hf in the HfX_2 is slightly stretched

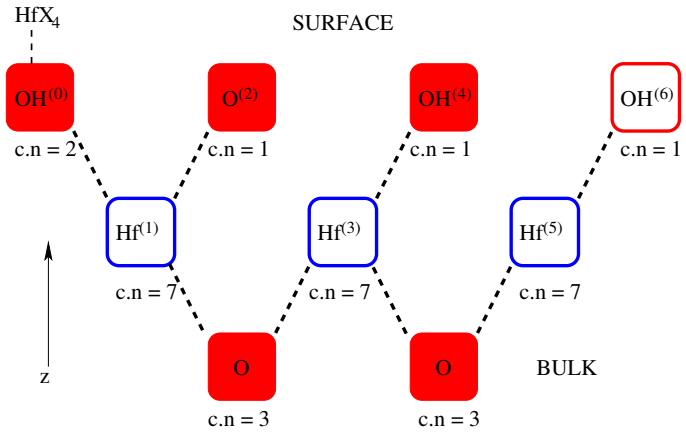


Figure 5.5: Schematic two-dimensional diagram of blocking after adsorption of the un-densified hafnium precursor. The filled boxes show blocked sites with respect to further adsorption of HfX_4 due to the presence of HfX_4 adsorbate at the surface site on the left (Same scheme as Fig. 5.1).

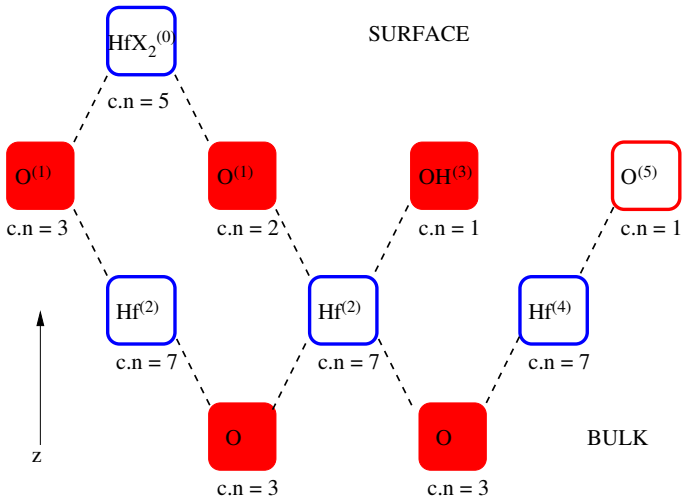


Figure 5.6: Schematic diagram of blocking after densification of the hafnium precursor onto a cation site. The presence of HfX_2 at the cation site precludes adsorption (filled boxes) at fewer sites than in HfX_4 at an anion site (Fig. 5.5).

to minimize repulsion between the remaining fragments. Applying the blocking process to the adjacent anion sites ensures that there is enough surface area available for these fragments.

DFT calculations show that as many HfX as possible can be densified into the adjacent cation positions. In Fig. 5.8, four HfX are densified into adjacent cation positions. The typical minimum distance between Hf−Hf in bulk HfO_2 is 3.3 Å. In Fig. 5.8, the distance between the highlighted Hf in the cluster is also 3.3 Å. This means that the repulsion between the remaining ligands declines in a surface covered with HfX when compared to HfX_2. The presence of HfX does not prevent adsorption at next neighbouring anion sites $\square^{(3)}$. Therefore, following desorption

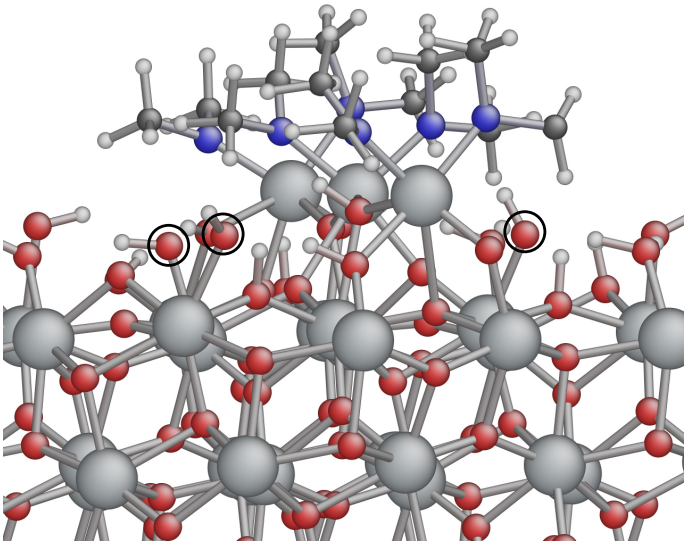


Figure 5.7: A cluster of three HfX_2 in adjacent cation/cation sites (DFT). The highlighted oxygen atoms are some of those that are blocked with respect to adsorption of another hafnium precursor. The Hf−Hf distance is stretched (3.9 Å) to minimize repulsion between the aligned ligands.

of HX from HfX_2 to leave HfX, blocking is lifted from all the surrounding anion sites.

5.12 H_2O adsorption

The probability of H_2O adsorption from the gas phase, like HfX_4 adsorption, is described by Maxwell-Boltzmann statistics (Eq. 2.26). In DFT simulations, we find that adsorption of Lewis basic H_2O takes place at specific sites of sufficient Lewis acidity, namely Hf atoms that are not coordinatively saturated. For instance, the X fragments in adsorbed HfX_3 push H_2O away from Hf and prevent bonding of the water molecule. Results from ab initio MD and DFT calculations show that adsorption of a H_2O molecule to an existing HfX occurs, provided that another HfX exists as a second neighbour of this HfX site, a so-called "co-operative" reaction (chapter 4). Therefore, adsorption of H_2O occurs at a pair of HfX or low coordinated Hf. The H_2O molecule is initially bridging between under-coordinated hafnium, and is then decomposed by the neighbouring oxygen or nitrogen into H + OH. The adsorption of H_2O is therefore a type β event. There is no steric blocking of adjacent sites by adsorbed H_2O.

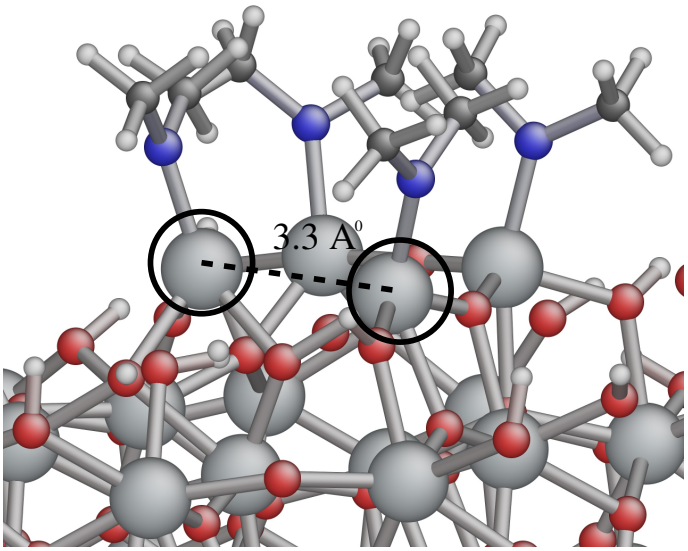


Figure 5.8: A cluster of four HfX in adjacent cation/anion sites (DFT). The distance between highlighted hafnium atoms (3.3 Å) shows that repulsion between the aligned ligands is less problematic than in the case depicted in Fig. 5.7.

5.13 H_2O densification and ligand exchange

Possible H_2O adsorptions at the HfX$-H_2O^{(0)}$ (cation site) clusters are followed by densification of the H_2O molecule on to the $\square^{(1)}$ anion sublattice so that oxygen becomes coordinated to a greater number of neighbouring Hf. Similar to HfX_2, densification of a H_2O molecule is a type γ event which changes the occupation of an anion and its neighbouring cation site. Upon densification, the c.n. of affected sites are updated, particularly the neighbouring HfX. The result of DFT calculations demonstrate that the presence of bridging O atoms in the neighbourhood of the HfX significantly enhances the rate of desorption of HX at this site. Thus, densification of H_2O and the resulting increase in the c.n. of the HfX sites means that desorption of the remaining HX is more likely to occur during the oxygen pulse. The net effect is an exchange of X^- with OH^-, albeit via an indirect route and with a change in surface location. This process is a combination of structural relaxation and a cooperative effect.

As mentioned earlier, desorption of the last HX from HfX has an activation energy which depends on the c.n. of the cation site. For instance, barriers to desorption of HX from 5, 6, and 7 coordinated Hf(HX) in the cation sites are 1.64, 0.83, and 0.56 eV respectively. Hence, desorption of this HX is facilitated by densification of a H_2O molecule to a neighbouring anion site, as this causes the c.n. to increase. Desorption of the last ligand from 7 or 8 coordinated HfX

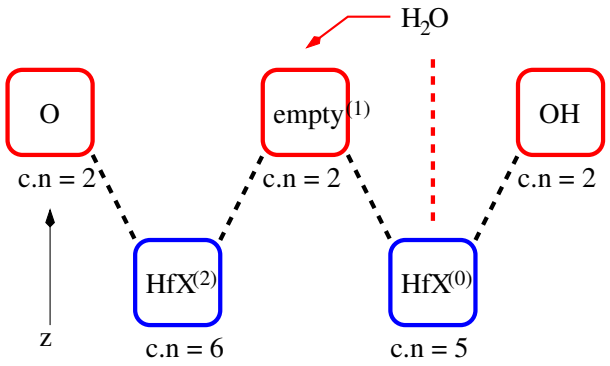


Figure 5.9: Schematic diagram of H_2O molecule adsorption in two dimensions. H_2O adsorption occurs in the cation site, due to the presence of another $HfX^{(2)}$ at the neighbouring cation site (cooperative event). Densification of the H_2O molecule (red arrow) occurs randomly into an empty anion site $\square^{(1)}$. (Same scheme as Fig. 5.1).

leaves Hf in the cation site with bulk-like coordination to O.

5.14 H_2O migration

After adsorption of a H_2O molecule, it is densified into an empty anion site, chosen randomly. In most cases, the adsorbed H_2O molecule is quickly dissociated by neighbouring oxygen atoms to yield OH + OH (section 5.15). These oxygen are usually strongly basic. However, in some cases, the H_2O molecule densifies to a low coordinated anion site and so becomes attached to fewer Hf atoms. As with HfX_2 migration above, migration of H_2O is introduced so as to allow the molecule to escape from such less favourable sites. This event is type γ. Activation energies for migration of a water molecule from anion to cation sites depends on the c.n. achieved as a result of densification: 0.43, 0.83, and 1.20 eV respectively for one, two, and three coordinated H_2O. However, when migration of the H_2O molecule is removed from the reaction list, the effect on the growth rate and quality of film is found to be insignificant. We conclude that the difference between random densification and densification incorporating H_2O migration is negligible.

5.15 H_2O decomposition

Results of DFT calculations show that the densified H_2O molecule is easily dissociated by the loss of H^+ to basic oxygen or nitrogen atoms. In order to include this in the KMC model, the H_2O molecule is decomposed into OH + OH due to the existence of under-coordinated oxygen at a neighbouring anion site $\square^{(2)}$ (type β). Fig. 5.10 shows how the proton of densified H_2O can be abstracted by

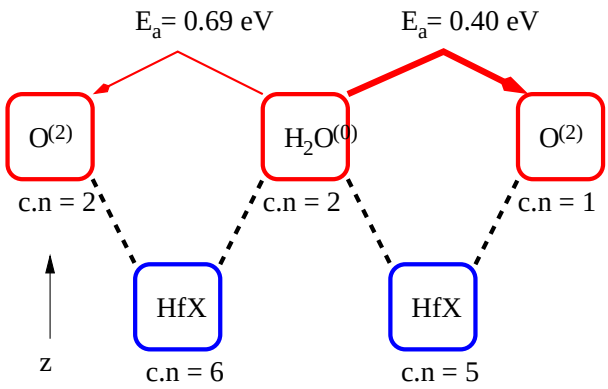


Figure 5.10: Schematic diagram of H_2O molecule decomposition in two dimensions. The activation energies for proton transfer are specified by the different c.n. of the two oxygen neighbours. The thicker arrow indicates stronger attraction by one coordinated oxygen to abstract a proton from H_2O. (Same scheme as Fig. 5.1).

oxygen at neighbouring anion sites. DFT calculations show that only one or two coordinated oxygen atoms can dissociate the H_2O molecule, and that the dissociation rate strongly depends on the c.n. of the neighbouring anion site. This reaction was not observed for more highly coordinated oxygen neighbours (c.n. = 3 or 4).

5.16 H_2O desorption

As described in the previous section, an adsorbed H_2O molecule decomposes due to the existence of adjacent Lewis bases (low coordinated oxygen, c.n. = 1 or 2). In the absence of Lewis basic sites, it remains as a molecule of H_2O and can possibly desorb from the system. Ab initio MD shows that desorption of a H_2O molecule happens more readily than desorption of the metal precursor. No other process for desorption of oxygen is considered here, as the other O-containing fragments are charged (O^{2-}, OH^-, $[OHfX]^+$, etc.). NEB calculations show that an activation energy of 0.46 eV is required to detach H_2O with c.n. = 1 for O (excluding H) from fully coordinated hafnium with c.n. = 7 and 0.83 eV for that from c.n. = 6. Such energy barriers (0.46 eV) can be easily overcome during the ALD process, especially if the temperature is increased. This event is type α.

5.17 Neglected reactions

Since every site of the anion sublattice is connected to 3 or 4 cation sites, through densification oxygen can obtain up to c.n. = 4 to Hf over the span of the oxygen pulse. We consider oxygen with c.n. = 3 or 4 as bulk-like oxygen. However,

some of the oxygen remains 1 or 2 coordinated to Hf. One-coordinated oxygen (possibly with H) are the active sites for adsorbing HfX_4 in the next pulse. The activation energy computed with DFT for hopping of O or OH after densification is too high to be significant for low temperature ALD. Hence, in the present study, oxygen and OH diffusion are ignored (as distinct from H^+ diffusion section 5.6).

Following adsorption of a H_2O molecule, densification or decomposition into OH groups may occur (section 4.4). However, no evidence was observed by DFT of two hydroxyl groups recombining again to produce a H_2O molecule. Therefore this recombination reaction is not considered in our KMC model.

The final type of reaction to be neglected was CVD-like reactions where the ligand X decomposes. These are known to be a significant component of HfO_2 growth from alkylamide precursors. We expect that the inclusion of CVD-like reactions would increase the growth rate. However, in the current calculations, the growth achieved by pure ALD reactions only is reported.

5.18 Summary

In this chapter, we develop a 3D on-lattice KMC model to describe the ALD reactions for growth of HfO_2 from $Hf(N(CH_3)_2)_4$ and H_2O. We implement all reactions (see Appendix A) that had been observed in first principles calculations (chapter 3) as discrete events in the on-lattice KMC simulation. The fundamental chemistry of ALD and its dependence on the local environment at the surface are implemented using c.n. and neighbour list. This includes all steps, from the early stage of adsorption of each ALD precursor, kinetics of the surface protons, interaction between the remaining precursors (steric effect), influence of remaining fragments on adsorption sites (blocking), densification of each ALD precursor, migration of each ALD precursor, and cooperation between the remaining precursors to adsorb H_2O (cooperative effect). Without any fitted parameters, the resulting simulations show the growth of smooth and conformal thin film at growth rates in agreement with experiment (chapter 6).

Chapter 6

Results of kinetic Monte-Carlo simulations and discussion

In this chapter the results of the combination of DFT and KMC calculations is presented. All DFT-derived reaction pathways (chapter 3 and 4) are implemented into the KMC (chapter 5) without any fitting parameters. The validity and necessity of the proposed reaction pathways are statistically established at the mesoscale. The adsorption of the HfX_4 precursors, ($X = N(CH_3)_2$), the formation of one monolayer of precursor fragments, and the statistical distribution of the precursor fragments in that layer, is shown at the end of the metal pulse. Adsorption and dissociation of the H_2O precursor onto that layer is described, leading to the delivery of oxygen and protons to the surface during the H_2O pulse. Through these processes, the remaining precursor fragments desorb from the surface, leaving the surface with bulk-like and OH-terminated HfO_2, ready for the next cycle. We will compare the theoretical results of KMC with *in situ* XPS and QCM experimental data.

6.1 Kinetics of reactions at the growing surface

6.1.1 Computational details and overview of growth

The dimensions of the simulation cell are 5.8×5.8×6.8 nm. The cell can contain 20 (111) layers of bulk monoclinic HfO_2 in the z direction. Every (111) layer of HfO_2 includes 256 sites for Hf (cation sites) and 512 sites for O (anion sites) which will become occupied during the simulation. Growth of up to 15360 atoms can therefore be explicitly simulated in this cell. The size of the simulation box determines the number of events per unit time. Hence, a larger box would mean an increase in the total rate, and so the KMC simulation would run more slowly. The size of box is considered reasonably large to fulfill the points of interest within

reasonable simulation time.

Fig. 6.1 shows the top view of the evolution of the surface during the first ALD cycle. Growth begins from an ideal situation in which the substrate is saturated with a regular array of OH groups (Fig. 6.1-1). The initial surface cell is constructed so as to consist of 256 O (c.n. = 2 or 3) atoms and 256 OH groups (c.n. = 1, for O excluding H). It was assumed that these highly coordinated oxygen (c.n. = 2 or 3) are attached to hafnium atoms of a sublayer beyond the cell. Fig. 6.1-2, Fig. 6.1-3, and Fig. 6.1-4 are snapshots taken at the end of the first metal precursor pulse time, at the end of the purge time, and at the end of the first oxygen pulse time respectively. In this study, saturation is obtained with the pulse and purge time both set at 0.1 ms for $T = 500$ K. No further adsorption of HfX_4 is observed by choosing to use a longer pulse time (i.e. 0.2 ms) at $T = 500$ K. These matters will be the subjects of our future study.

During the metal pulse, protons are observed to 'bounce' frequently between the surface oxygen and the nitrogen of the HfX_4 or HfX_3 or HfX_2. These diffusion events continue in time until all the remaining nitrogen of a precursor fragment has become protonated (multiple proton diffusion, chapter 3). In this situation, desorption of HX is facilitated[95] and different species (the remaining fragments) can be seen at the surface, Fig. 6.1. We have carried out alternative KMC simulations where multiple proton diffusion is switched off and single proton diffusion is followed by HX desorption with slow kinetics. No evidence of growth is observed in these simulations at 500 K.

In H_2O pulses, the remaining ligands are desorbed from the surface and replaced with OH groups. In this process, blocking (section 5.11) is lifted from active sites through desorption of the remaining ligands. The net effect is deposition of bulk-like HfO_2 leaving an OH^- terminated surface for the following cycle. An average thickness of 0.60 ± 0.02 Å/cycle of HfO_2 is deposited in each cycle. Growth is observed simultaneously in multiple layers rather than a single smooth layer in each cycle. On average, 8.6×10^7 events per cell are executed in each cycle.

Our simulations show that the population of surface species changes with temperature. The presence of different species changes the dominant reaction pathways and their associated activation energies, impacting the growth rate. In this situation, owing to the change of activation energies being sampled, a longer pulse time should be considered at low temperature and surface saturation is achieved more rapidly at high temperature.

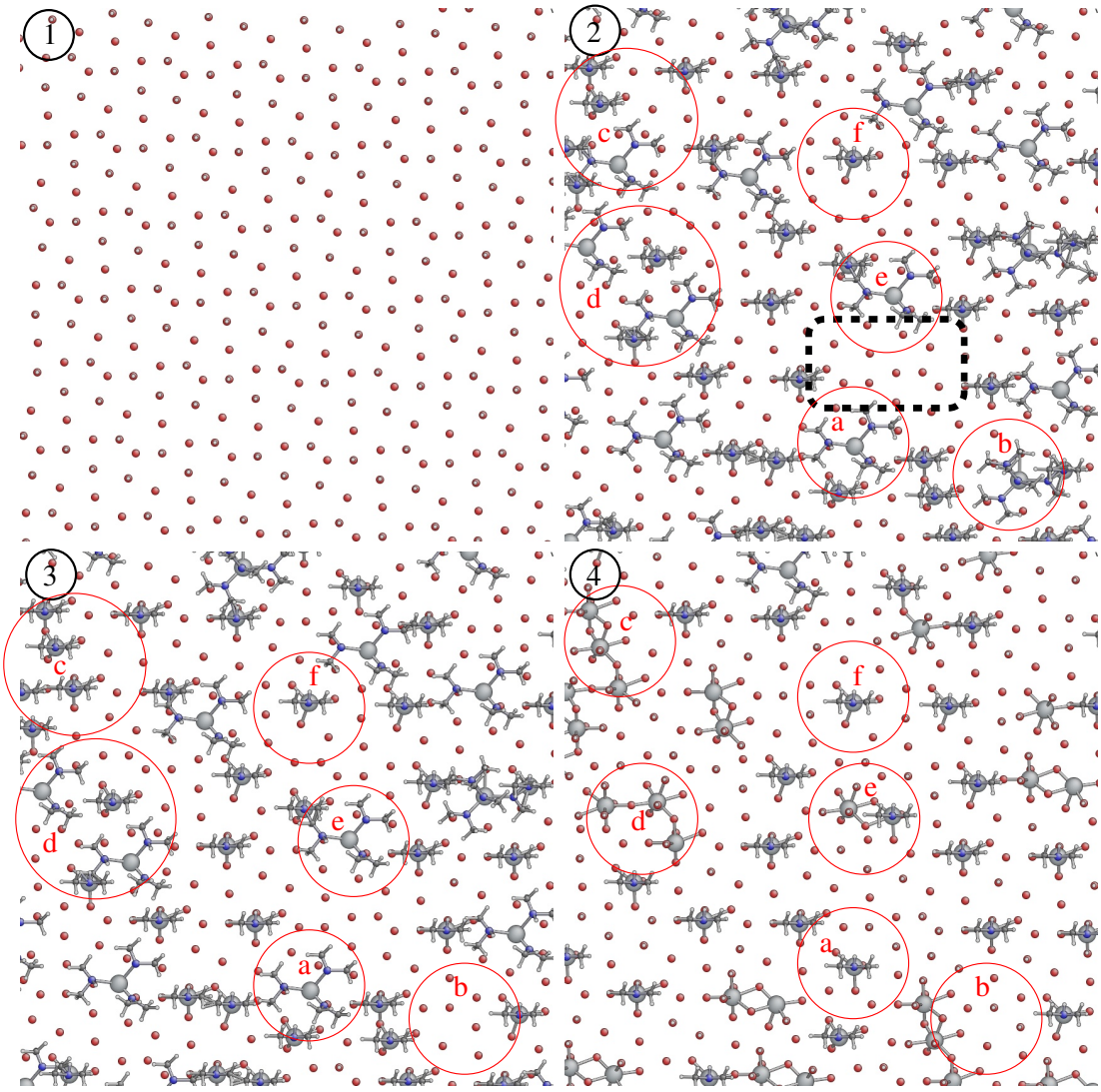


Figure 6.1: Top view of the surface evolution during the first cycle. Snapshots show: (1) The substrate which includes two layers of oxygen (O and OH groups). (2) The end of the metal pulse with a surface that is depleted of protons due to the desorption of HX. The dashed box shows an area where adsorption of the next metal precursor is blocked because of the steric effect. (3) The end of the purge with a minor amount of further desorption. (4) The end of the oxygen pulse in which the arrival of H_2O molecules causes oxygen and protons to be introduced to the surface. Fragments for discussion (a to f) are highlighted by circles.

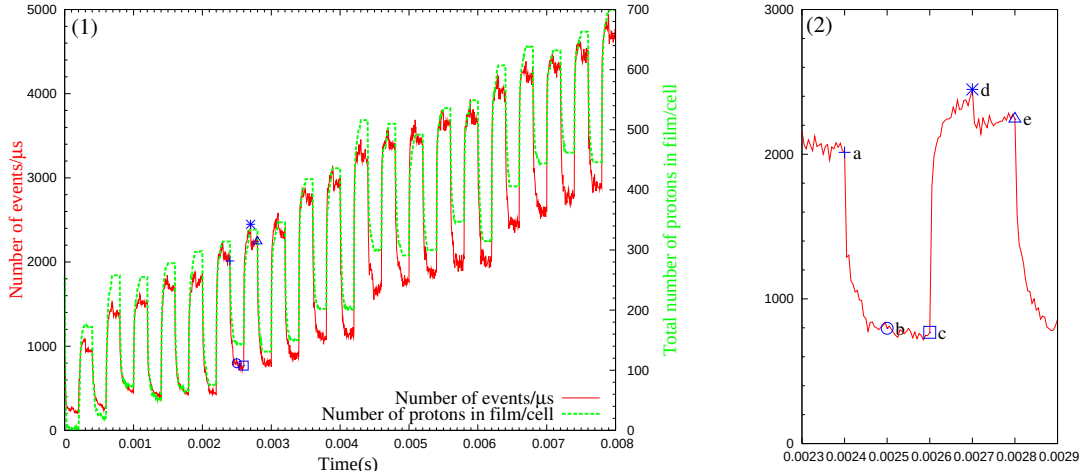


Figure 6.2: (1) Proton population in film and number of events for 20 cycles. Pulse and purge time have been both fixed at 0.1 ms and temperature is 500 K. Proton population and number of events increase constantly due to the accumulation of protons in the subsurface layers. (2) Magnification of one cycle (a) Start of metal pulse (cycle), (b) Start of purge, (c) Start of oxygen pulse, (d) Start of purge, (e) End of cycle.

6.1.2 The metal precursor pulse

In this section, surface reaction kinetics will be inspected during the metal precursor pulse. Fig. 6.1-2 shows the fragments remaining after one metal precursor pulse. Due to the ALD reactions, desorption of ligands as HX has occurred. The surface has become depleted of protons. The remaining HfX_3, HfX_2, and HfX fragments at the surface prevent further adsorption of HfX_4; that is, the surface is saturated. For instance, between species 2a and 2e, there are low coordinated substrate oxygen atoms, but insufficient space for adsorption of the metal precursor to occur. The proton population in the film as a function of time is shown for 20 cycles in Fig. 6.2. Desorption of HX is visible as a sharp decrease in the proton population at the start of each metal pulse. Correlated with this, there is a sharp decrease in the number of events at the beginning of each metal pulse.

The proton concentration remains low up to the start of the oxygen pulse (Fig. 6.1-3). Dissociation of the H_2O molecule supplies a source of protons for renewed HX desorption. At the beginning of the oxygen pulse, an increase in the number of events is observed (Fig. 6.2). This corresponds to an increase in the proton population, introducing many proton diffusion events between oxygen atoms. Hence, many of the remaining ligands are eliminated (Fig. 6.1-4).

The number of protons in the film increases constantly during subsequent ALD cycles (Fig. 6.2). Those protons remain in the layers below the surface. It is unclear whether this is an artifact of our KMC scheme or whether it matches experiment. The protons can undergo proton diffusion reactions within the sub-

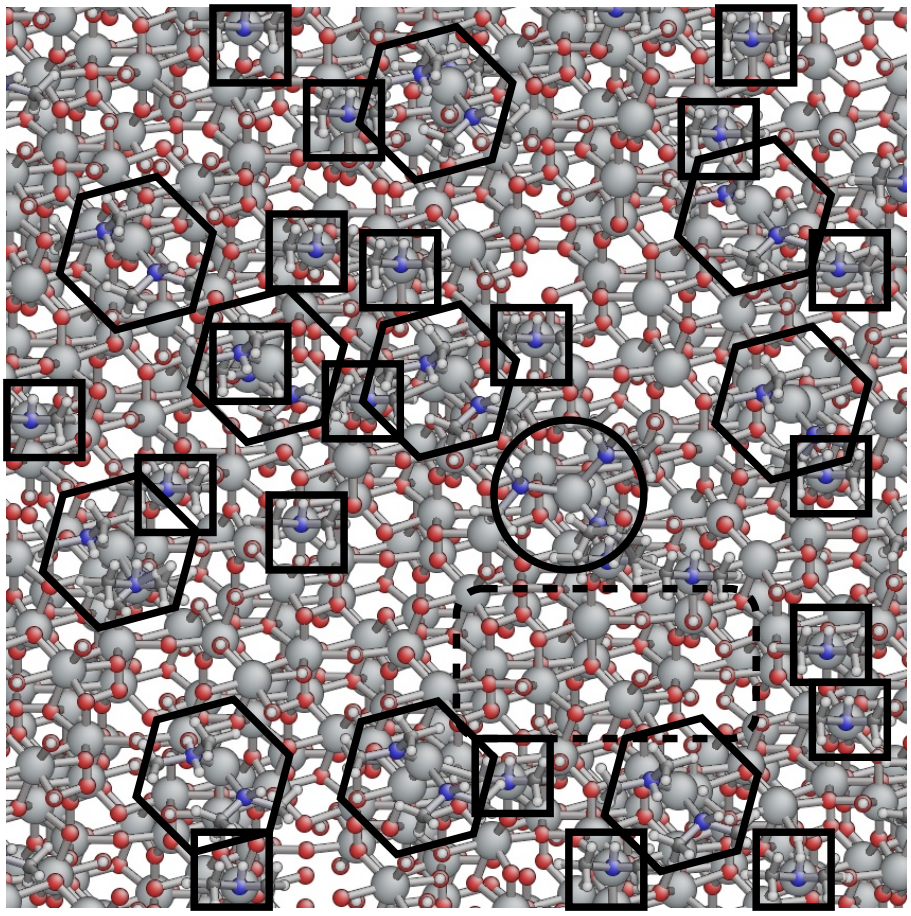


Figure 6.3: Top view of the surface at the end of the 18^{th} metal pulse. HfX_3, HfX_2, and HfX are highlighted by circles, hexagons, and squares respectively. The dashed box shows free space where adsorption of HfX_4 does not occur. The O and OH groups in the dashed box are highly coordinated or blocked by the remaining ligands.

layers but, without access to X, there is no effect on growth. These events are, therefore, wasteful of CPU time. For instance, the CPU time per cycle increases by a factor of 1.5 between the 5^{th} cycle and 40^{th} cycles, almost entirely due to unproductive diffusion of protons in sublayers. Those protons can be observed as OH groups in the dashed box of Fig. 6.3, which shows the end of the metal pulse after eighteen cycles. Those OH groups are highly coordinated or blocked. Despite the free space around them, adsorption of the next metal precursor does not take place.

During the metal pulse, the number of ALD reactions occurring (particularly desorption of HX) decreases, owing to the depletion of the H^+ co-reagent. Interactions between the remaining precursors prevents further adsorptions. However, the self limiting nature of ALD is not solely a consequence of depletion of co-reagent. As highlighted in Fig. 6.3 (dashed box), depletion of active sites also prevents further adsorptions. In addition, inert HfX and HfHX fragments

(squares) resist desorption of the final ligand, regardless of H^+ concentration.

All energetically accessible remnants of the Hf precursor (HfX_4, HfX_3, HfX_2, and HfX) can be observed at the end of the metal pulse, which we now discuss. One HfX_4 can be seen in Fig. 6.1-2b and this species is desorbed intact during the purge (Fig. 6.1-3) as there are not enough protons in its neighbourhood to protonate its ligands. The HfX_4 population changed from $0.14/nm^{-2}$ at the end of the first cycle to zero at the end of 18^{th} cycle.

HfX_3 is the other species that is often seen during the initial cycles. This species is highlighted as a, e, c, and d (Fig. 6.1-2). If there are insufficient protons in the neighbourhood of the adsorbed HfX_4, then the product is HfX_3 rather than HfX_2. This is because desorption of HX from HfX_3 is more difficult than from HfX_4.[95] This species has been observed less in later cycles than in first cycles. For instance, the HfX_3 population changed from $0.62/nm^{-2}$ at the end of the first metal pulse to only $0.02/nm^{-2}$ HfX_3 at the end of the 18^{th} metal pulse (circle in Fig. 6.3).

HfX_2 is not visible in the snapshots of the first cycle shown (Fig. 6.1) although it is an important intermediate during KMC. This is because its lifetime is too short here. However, in the next cycles, HfX_2 does appear at the surface and lasts longer. For instance, the HfX_2 population is $0.59/nm^{-2}$ at the end of the 18^{th} metal pulse (Fig. 6.3 hexagon), which is much higher than that in the first cycle. The Hf atoms in these HfX_2 are always 3 or 4 coordinated.

We now discuss the reasons for the persistence of HfX_2 in later cycles. If through the densification process Hf becomes highly coordinated (c.n. $\geq$5), ALD reactions will continue rapidly until the remaining fragment is HfX. In Fig. 6.3 and Fig. 6.1-2a the dominant configuration is HfX. However, if Hf remains under coordinated (c.n. $<$ 5), despite the densification process, migration events can occur. In this case, the HfX_2 population is constant while this species diffuses slowly across the surface (referred to as "crawling"). Crawling will continue until the precursor remnant densifies into a cation site with a higher c.n.. ALD reactions will then occur rapidly on the remaining fragment of HfX_2, until it terminates at HfX again, ultimately resulting in a smooth and dense film (Fig. 6.6-2, Fig. 6.4-2).

The growth rate for the 16^{th}-20^{th} cycles of ALD is reported in Fig. 6.5. When all the ALD reactions are included in the event list, the growth rate varies between 0.49 and 0.75 Å/cycle from cycle to cycle. This simulation includes both cooperative effects and structural relaxation (densification and migration) (chapters 3 and 5). These KMC growth rates are in excellent agreement with experimental results considering that no activation energies were fitted to experiment.[26,31,130] For example, a growth rate of 0.78 Å/cycle is reported by Cho et al.[31] at 300 °C.

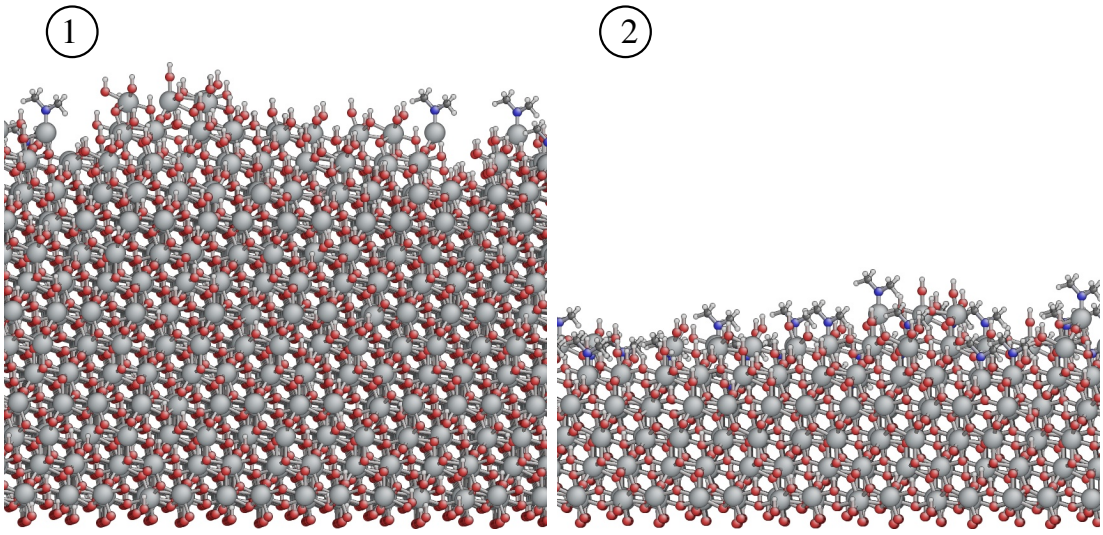


Figure 6.4: Side view of ALD growth for HfO_2 after 20 cycles. (1) Direct adsorption of H_2O molecules through HfX is considered (cooperative effect is neglected). As a result, the growth rate is overestimated by a factor of 2 compared to that obtained when including the cooperative effect only. (2) Cooperation between the HfX is required in order to adsorb a H_2O molecule.

In order to examine the effect of HfX_2 migration on the growth rate in KMC, the migration process was turned off. Turning this migration off resulted in a growth rate that varies between 0.12 and 0.20 Å/cycle for the 16^{th}-20^{th} cycles (Fig. 6.5). In other words, excluding the migration causes a low growth rate and poor quality of growth (Fig. 6.6-1).

In spite of migration being allowed, Hf in the remaining HfX_2 fragment sometimes does not obtain a high enough c.n. and remains 3 or 4 coordinated. In those situations, dissociation of HX does not happen, even though there are suitable protons at the surface (Fig. 6.3, dotted box). The system becomes trapped in a set of adjacent local minima (a superbasin) (subsection 2.2.3), where migration happens repeatedly, with no net effect, other than wasting CPU time.

HfX fragments are the dominant species at the growing surface at the end of metal pulse (Fig. 6.1-2 and Fig. 6.3 (square)). For instance, the HfX population changes from $1.51/nm^{-2}$ at the end of first cycle to $1.42/nm^{-2}$ and $1.90/nm^{-2}$ at the end of the 18^{th} and 20^{th} cycles, respectively. Such variation may be correlated with the cycle-to-cycle variation in growth rate.

6.1.3 The purge

When ALD reactions self-terminate, the remaining ligands block the surface and this persists into the purge step. We have examined our KMC simulations to

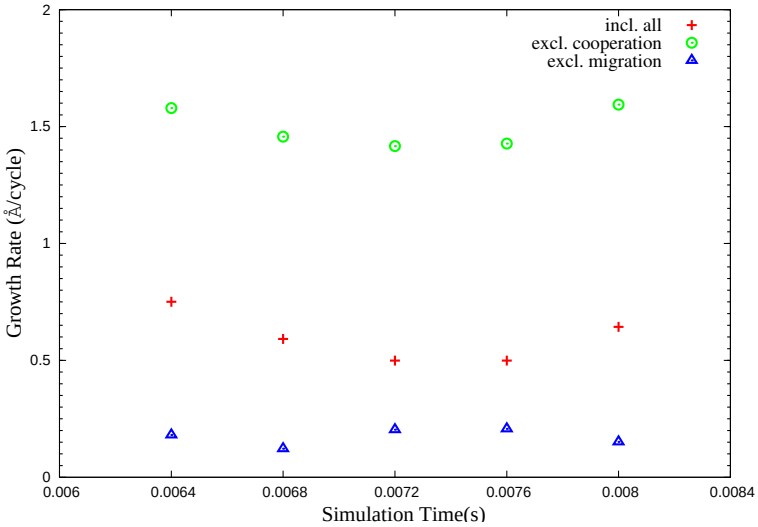


Figure 6.5: Growth rate of HfO_2 in different circumstances versus time for the 16^{th}-20^{th} cycles. The thickness of a monolayer of HfO_2 is 2.8 Å. Cross shows growth rate considering all observed ALD reactions. Circle shows growth rate when direct ligand exchange during oxygen pulse is considered rather than co-operative effect. Triangle shows growth rate when migration process is switched off.

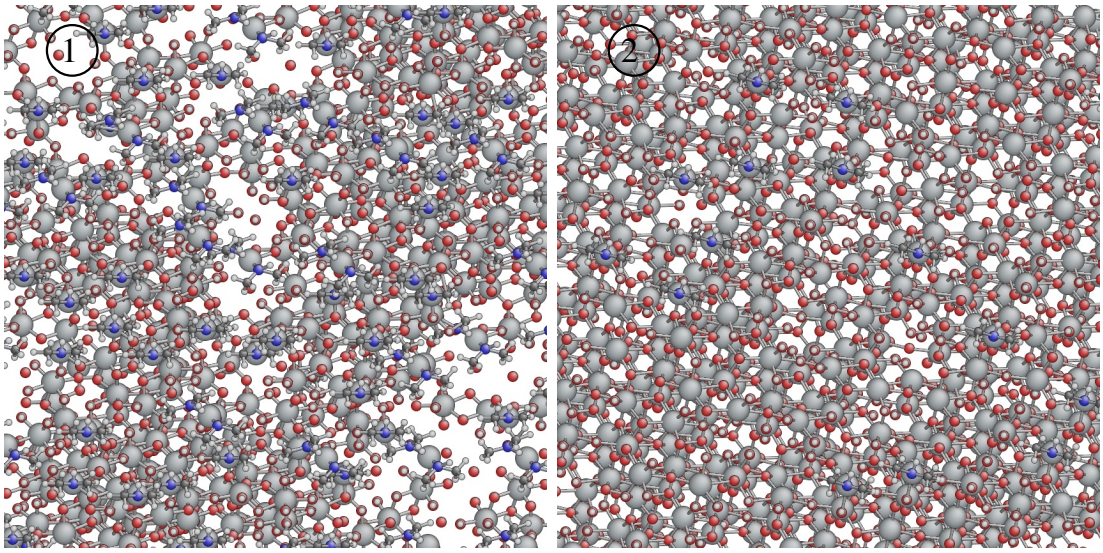


Figure 6.6: Top view of ALD film growth for HfO_2 after 20 cycles. (1) Migration is removed from the reaction list; a low growth rate and poor quality of film is obtained. (2) Structural relaxation events are considered; a realistic growth rate and dense film is achieved.

see if further surface reactions are taking place during the purge. For instance in Fig. 6.1-2c, we see that some HfX_3 remains at the surface because there are not enough protons in its neighbouring sites. After a period of time during the purge, due to longer-range proton diffusion across oxygen atoms, all nitrogen atoms of these HfX_3 fragments become protonated and some of them desorb as HX. Then, the remnant densifies to the neighbouring HfX (Fig. 6.1-3c). This illustrates that slow proton diffusion and associated reactions such as desorption of HX continue during the purge time. Indeed, Fig. 6.2 shows that reaction events (mainly proton diffusion) continue at roughly the same frequency during both purges, with just a small decrease over time. This decrement corresponds to the minor desorption during the purge time. Of course, a longer pulse duration would allow this desorption to occur during the pulse instead of during the purge.

The KMC simulations thus illustrate that fast reactions saturate quickly, while slow reactions take orders of magnitude longer. This disparity may explain experimental saturation curves and the difficulty in choosing the optimum pulse/purge time.[129]

6.1.4 The oxygen precursor pulse

Chemisorption of the H_2O molecule onto a Lewis acidic Hf site is a necessary first step for dissociation of the H_2O molecule. Individual Hf have low acidity when bound to a ligand X like $N(CH_3)_2$. However, we have found that the H_2O molecule can adsorb through cooperation between a cluster of HfX fragments (section 3.7). Such a cluster can be seen in Fig. 6.1-3c, where five HfX are in close proximity. In Fig. 6.1-4c all of these X ligands have been replaced with OH groups. The cluster in Fig. 6.1-3d undergoes a similar reaction to Fig. 6.1-4d. The lifetime of adsorbed molecular H_2O is too short for it to be observed frequently during the simulation.

By contrast, isolated HfX that is not part of a cluster cannot undergo ligand exchange during the oxygen pulse (Fig. 6.1-4f) (section 3.7). We have attempted running the KMC model with direct ligand exchange at isolated HfX rather than in a cluster and we observe that the growth rate increases to 1.41-1.59 Å/cycle, over twice that obtained when only the cooperative effect is included (Fig. 6.5). A side view of the simulation box for this direct exchange simulation is shown in Fig. 6.4-1.

As indicated in Fig. 6.1-3c, creation of a cluster of HfX during the metal pulse is statistically probable. The necessity of the cooperative effect for adsorption of a H_2O molecule, discussed energetically in section 3.7, is shown quantitatively here. Dissociation of the H_2O molecule creates active sites (OH groups) for the

next cycle, as seen in Fig. 6.1-4c.

Incoming protons from dissociation of H_2O molecules in the clusters (*e.g.* Fig. 6.1-4c), cause nitrogen atoms in the remaining ligands to become protonated (Fig. 6.1-3d). Hence, two HfX_3 lose their remaining ligands to become HfX and densify into the surface. Then, those HfX create a cluster such as Fig. 6.1-3c, during the oxygen pulse. The lifetime of this intermediate is short and therefore it is not visible in this snapshot. Ligand exchange immediately happens through the reaction pathway presented for Fig. 6.1-4c, causing the final HX desorb and leaving an OH^- terminated surface (Fig. 6.1-4d).

As well as delivering protons, dissociation of H_2O molecules will also deliver oxygen to the surface. The new oxygen atoms become highly coordinated as the number of remnant ligands decreases, and so these oxygen atoms are densified into the surface and subsurface layers resulting in a dense film. As a result, further desorption of the remaining ligands is facilitated. However, if the adsorbed oxygen atoms remain poorly coordinated, then they become the active sites for the next Hf pulse (section 3.4).

The incoming protons from the dissociation of H_2O also cause desorption of the remaining ligands. The HfX_3 fragment in Fig. 6.1-3a at the end of the purge loses HX until it terminates as HfX in Fig. 6.1-4a at the end of the oxygen pulse. Since there is no HfX at the neighbouring sites, in the case of Fig. 6.1-4a as well as 4f, the metal precursor terminates in HfX at the end of the cycle. This is significantly different from the common assumption that all ligands are eliminated in every ALD cycle.[131] The case illustrated in Fig. 6.1-3e is slightly different. Desorption of HX results in densification of the metal precursor to a pre-existing HfX neighbour. One of the Hf atoms obtains sufficient c.n. from the densified oxygen by dissociation of the H_2O molecule at this site. Further desorption of HX thus occurs from this cluster and fully coordinated Hf does not cooperate to adsorb a further H_2O molecule. Hence, another HfX present in the cluster remains under-coordinated in Fig. 6.1-4e.

In each cycle, the "freshly-deposited" fragments of Hf precursor are usually spaced widely, rather than in clusters, due to the steric bulk of the precursor. Therefore, creation of a cluster of HfX may not happen during a single cycle. However, metal precursors arriving during the next metal pulse may combine with pre-existing HfX to create clusters. These clusters are active sites for adsorption of H_2O molecules such as those shown in Fig. 6.1-3c. In this way, almost all ligands are eventually eliminated over many cycles. Moreover, the ALD growth continues simultaneously in different layers (section 6.2) and, therefore, a cluster may be created that spans multiple layers.

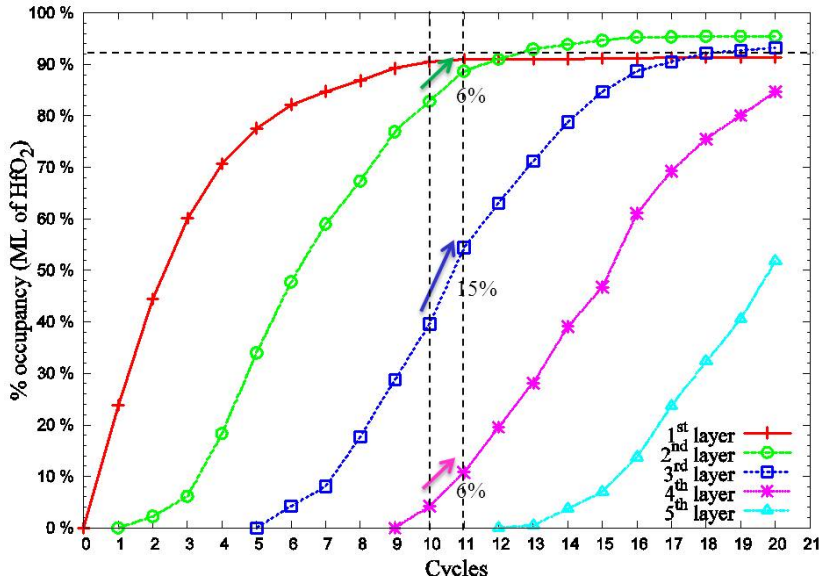


Figure 6.7: The pattern of growth in ALD film for HfO_2 at the end of each cycle during 20 cycles. Each layer converges to >92% of a crystalline monolayer of HfO_2 (horizontal dotted line). Growth between cycles 10 and 11 (vertical dotted line) is indicated in three different layers. Simultaneous growth in different layers is observed in each cycle.

6.2 Simultaneous growth in different layers

Fig. 6.7 shows the growth pattern and illustrates that more than 10 cycles is required for a monolayer of HfO_2 to be filled (closed). Each layer of HfO_2 converges to more than 92% of a crystalline monolayer of HfO_2, but never converges to 100%. This means that some sites in our on-lattice KMC remain empty as vacancies in the closed layer. Similar growth behaviour was observed for 40 cycles. Only the first layer contains the substrate effect.

The simultaneous growth of thin film in three different layers is observed as a constant feature of the KMC simulations for HfO_2 ALD from $Hf(N(CH_3)_2)_4$ and H_2O. As an example, we examine the partial growth rate for each of three layers of HfO_2 between cycles 10 and 11 (Fig. 6.7). 6% of the total growth rate is gained by the 2^{nd} layer as it approaches the convergence limit. While the same amount of the total growth rate is gained by 4^{th} layer, the highest proportion of the total growth rate in this cycle (15%) occurs in the 3^{rd} layer. The total increase in site occupancy is 27% of a monolayer. Once the occupancy of layer N is > 20%, growth in layer N+1 commences. The pattern of shared growth across multiple layers in our KMC model is in sharp contrast to the traditional idea in ALD of achieving a closed oxide layer and then starting a new layer. Although this finding is expressed in terms of the discrete crystalline layers of our lattice-KMC model, we suggest that the same behaviour is seen in actual ALD, whether

of crystalline or amorphous films, since here too new material will nucleate on top of pre-existing sections.

6.3 Simulated atomic ratio from KMC

The O/Hf atomic ratio for each growing monolayer of HfO_2 is shown in Fig. 6.8 for 30 cycles. The 1^{st} layer is converged to a ratio of 2.6 and the substrate effect is observed here again. Each of the 2^{nd} to 5^{th} layers is converged to O/Hf = 2.3.

Clearly, crystalline HfO_2 should have an O/Hf atomic ratio of 2. As shown in Fig. 6.8, at the beginning of deposition of each layer, there is more Hf than O. This means that initially the remaining Hf precursors are low coordinated. Through the incoming oxygen precursors in the next cycles, Hf become fully coordinated to O. In this circumstance, the O/Hf ratio in each layer crosses the first dashed line (ratio=2). In the next cycles, O atoms from the incoming oxygen precursor have a higher ability to penetrate into sublayers than Hf atoms from the incoming metal precursor. While Hf atoms are fully coordinated (c.n.=7) in each layer, some of its O atoms are partially coordinated (*e.g.* c.n.=2). In this circumstance, the O/Hf ratio in each layer converges to a higher value. This result is in excellent agreement with *in situ* XPS experimental data for TDMAHf + H_2O where the O/Hf ratio calculated from the peak intensities of the O1s and Hf4d is also 2.3.[27]

This corresponds to the high proton population in sublayers. In Fig. 6.9 the proton population in each layer of HfO_2 is shown over a period of 20 cycles. 100%H means all oxygen atoms in a layer of HfO_2 are protonated (*e.g.* 512 OH groups per layer). The proton population in each layer ascends to approximately 30% during 8-10 ALD cycles (*e.g.* 6^{th} layer). Following this ascent, the proton population in each layer descends to approximately 20% but never descends to 0%.

The accumulated protons in a sublayer cause oxygen to stay in low coordination (c.n. = 2 excluding H). As mentioned before (subsection 6.1.2), the accumulated protons increase the number of proton diffusion events leading to a waste of CPU time. Many proton diffusion events continue to take place, both in inter- and intra-layers, mediated by low coordinated oxygen.

The atomic concentration analysis shows that grown thin film is deposited with some extra OH. These OH groups are located in the closed layers or at the growing surface. If the atomic concentration is written as $[HfO_2]+x[Hf(OH)_4]$, then we find that x varies from 0.21 to 0.20 between cycles 20 and 30 respectively. This explains the oxygen excess in the film (O/Hf=0.23).

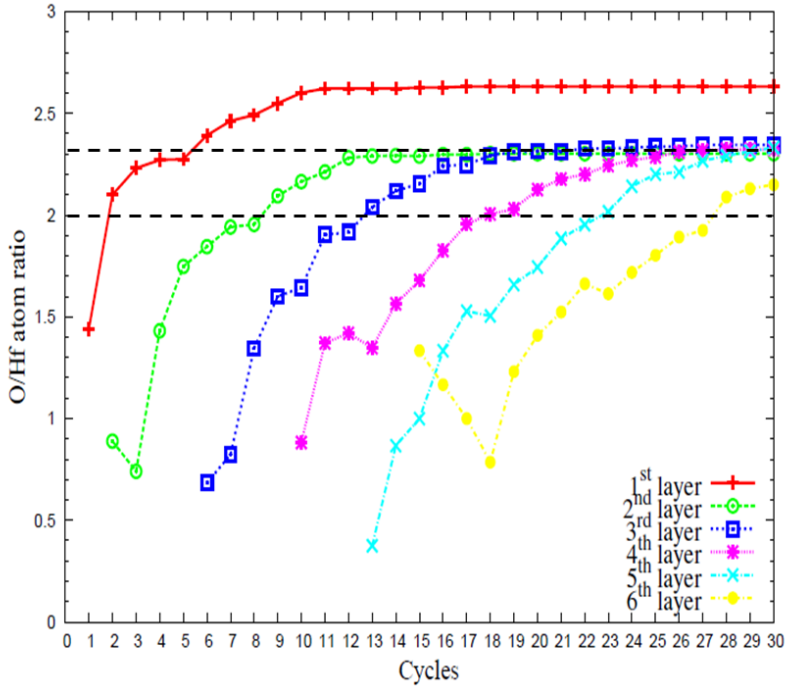


Figure 6.8: O/Hf atomic ratio simulated from the KMC in each layer of HfO_2 during 30 cycles. With neglecting the substrate effect (1st layer), the O/Hf atomic ratio in each layer converges to 2.3.

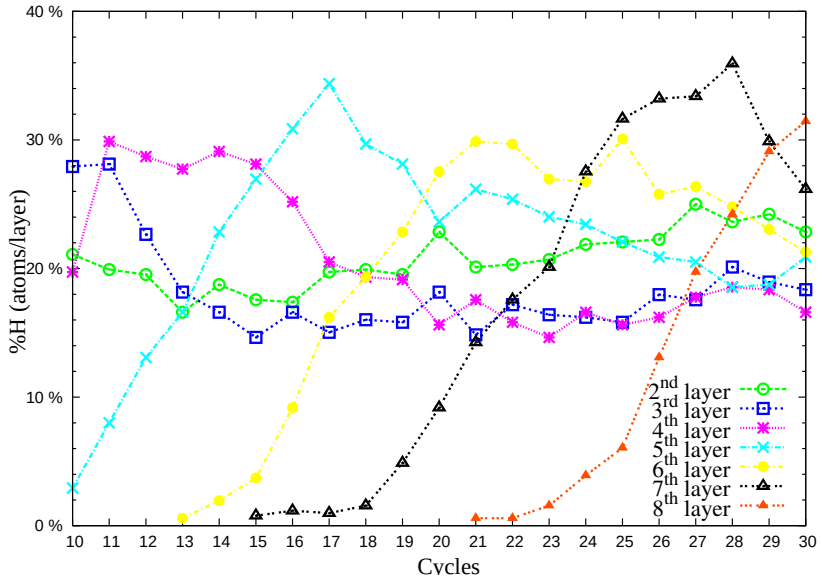


Figure 6.9: The proton population in each layer of HfO_2 over a period of 20 cycles. The ascent of the proton population in each layer corresponds to the beginning of growth in that layer and the subsequent descent signals the creation of a closed layer.

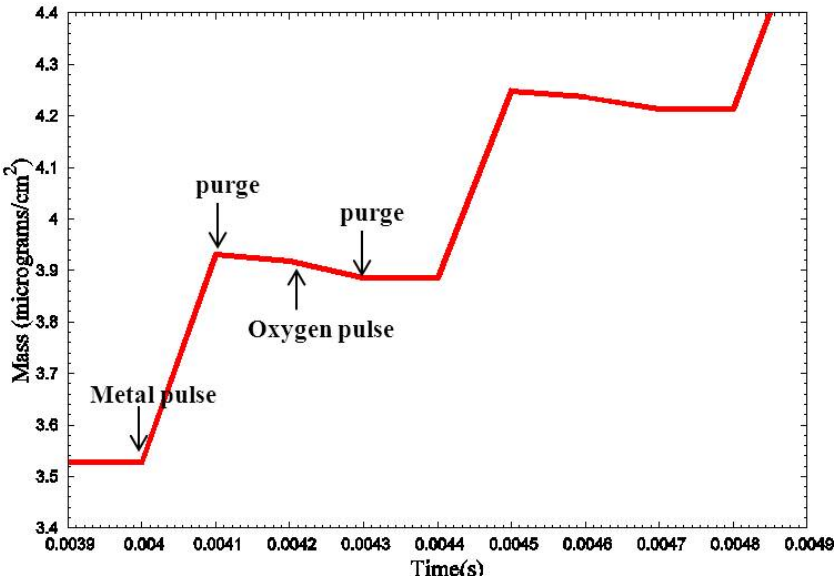


Figure 6.10: Mass increment of HfO_2 during two cycles of ALD simulated by KMC. The calculated mass gain/loss ratio varies between 9.7 and 10.9 from cycle to cycle. The calculated rate of net mass increase is 0.38 ± 0.01 μg/cm^2 per cycle.

6.4 Calculated mass gain from KMC

In QCM studies of this process a large mass gain occurs during the metal pulse exposure.[132] The desorption of fragments during the purge and ligand exchange during the oxygen pulse cause a mass loss. A subsequent mass gain is again produced when the metal pulse deposits hafnium to the surface oxygen or substrate region. This periodic behaviour of mass gain/loss is observed during our KMC simulation. Fig. 6.10 shows the mass increment of HfO_2 during two cycles of ALD simulated by KMC. The start of each pulse and each purge are specified. The calculated ratio of mass gain/loss varies between 9.7 to 10.9 in different cycles. The measured mass gain/loss ratio is about 7.3 from QCM experiment[132] at $T = 473$ K, which is lower than the KMC value.

The calculated net mass increase for a cycle of ALD is 0.38 ± 0.01 μg/cm^2 in KMC. The net mass increase during a cycle from experiment[132] was 0.24 μg/cm^2 which is lower than the theoretical mass increase from KMC. This is reasonably good agreement considering that our work is completely theoretical. It seems that due to the small size of the cell and the on-lattice KMC regime, a dense and smooth thin film was achieved theoretically by KMC rather than the less dense observed experimentally.[131] With a larger simulation box, including CVD type reactions and allowing off-lattice KMC, we would be able to simulate the growth of less dense film in ALD and perhaps obtain better agreement with experiment.

6.5 Discussion and conclusion

Adsorption of HfX_4 and the self-terminating formation of one monolayer of precursor fragments - crucial for ALD - the statistical distribution of the remaining fragments at the end of the metal pulse is observed in our simulations (subsection 6.1.2). Adsorption and dissociation of H_2O in clusters of adsorbed HfX are described, leading to the delivery of oxygen and protons to the surface during the oxygen pulse. Through these processes, ligands desorb from the surface in both pulses, leaving the surface with bulk-like HfO_2 terminated by OH for the next cycle. However, creation of a cluster of HfX may not happen during a single cycle. Therefore, we see that some isolated HfX remains on the surface at the end of the oxygen pulse and persists for multiple cycles. We speculate that an increase of pressure would raise the impingement rate of the H_2O molecule. This increase in molecular flux may wipe off the ligand of isolated HfX and replace it with OH (section 7.2). Simulating such a situation would be a possible future topic.

Proton transfer is the dominant reaction in the event list. The number of reaction events per unit time thus correlates strongly with the concentration of protons in the film. The kinetics of the surface protons are effective in leading to ligand desorption. Depletion of protons during the metal pulse and delivery of protons during the oxygen pulse cause respectively a decrease and then an increase in the number of events. Some of the introduced protons persist in the bulk and do not participate further in the ALD reaction, leading to an increase in CPU time required for KMC, but with no effect on growth. This eventually limits the number of cycles that can be simulated in reasonable CPU time. Dismissing proton diffusion in the closed layers would be an option to eliminate those events.

ALD growth is observed to occur simultaneously in different exposed surface layers. In this way, the inherent roughness or smoothness of the growth process can be quantified, which is another key property of ALD. The calculated O/Hf atomic ratio from KMC is in excellent agreement with that from *in situ* XPS experiment. However, the mass increase per cycle is lower than measured in QCM experiment.

Chapter 7

Ongoing research and future studies

7.1 Accuracy of reaction pathways

Sampling of reaction pathway in ALD chemistry is an important topic. In principle, massively-parallel computers allow hundreds/thousands of reaction pathways to be sampled simultaneously. However, practical experience shows that ALD chemistry is so complicated that automated transition state searches are rarely successful, and that the preference of the user in defining the model is still a major constraint. The higher number of atoms means the higher number of possible geometries and reaction pathways.

We showed in chapter 4 that considering higher number of atoms results another plausible pathway which has a significant impact on simulation of ALD. Considering this pathway is important for both atomistic simulation (*e.g.* DFT) and macroscale calculation (*e.g.* fluid flow) which is coupled with surface kinetics reaction.[34] In atomistic simulation, with advances in parallel computer architecture, the accuracy of the proposed pathway can be increased by using post-HF methods like CCSD.[35] This allows more realistic model is performed in higher-scale using the more accurate activation energies.

Care is needed in investigating the non-ALD reactions (*e.g.* CVD type) due to the changing numbers of electrons in the reaction as this can lead to uncontrolled errors in the DFT energetics as consequence of poor error cancellation. Non-ALD reactions need higher chemical accuracy, which can be reliably achieved by more advanced methods than DFT (subsection 2.1.5.2). Hence, we did not calculate non-ALD reactions by DFT here. We anticipate that including non-ALD reactions leads to better estimation of growth rate and increases the level of complexity of ALD chemistry.

7.2 Morphology and reaction condition

Both ALD and non-ALD reactions are sensitive to reactor conditions. An increase or decrease in temperature will change the adsorption of precursor and distribution of remaining precursors. An increase in pressure may introduce physisorption of precursors at the surface or substrate. These precursors may not become involved in ALD reactions and may be stored as intact molecules at the surface. If the temperature remains low, these intact molecules will result in a higher growth rate.

Above examples result to the different reaction pathways, growth rate, level of impurities, and film morphology. One of the ambitions in ALD is to build a model that explicitly describes how precursor chemistry and reactor conditions dictate nanomorphology. To build a desired approach, an accurate KMC which retains the accuracy of DFT obtained results, will be a suitable choice. However, two supplementary features would need to be implemented into KMC to describe nanomorphology in this way, as follows.

First, related to ALD chemistry, is consideration of physisorbed precursor. A proper adsorption and desorption rate of precursor should be regulated using DFT+D approach (subsection 2.1.5.3). Obviously, adsorption and desorption rate depend on reactor condition. For example, physisorbed precursor most likely desorb from the surface at high temperature and long purge time.

Second, to investigate the morphology of grown film (crystalline vs. amorphous), the fixed lattice sites of simulation box should be dismissed. To get rid of the predefined lattice site, an atomic site with its associated variables can be introduced on the fly based on graph theory. The introduction of a new site can be performed based on local bonds and local elements at a predetermined distance from an existing site at the surface.

7.3 Advantages and disadvantages of KMC-derived data

KMC offers a way to examine the combination together of provided mechanisms from the ab initio level. The logical sequence of reactions, depending on both availability of reactants or other reaction products, can be assessed. Occasionally, KMC can recognize a missing reaction that can be investigated by the ab initio method. For instance, cooperation between remaining ligands to adsorb and dissociate the incoming H_2O molecule (chapter 4) was discovered by KMC and computed by DFT.[95,133] However, a missing reaction or event may cause a significant error. Hence, one should expend extreme effort to avoid missing any

reactions.

It is well-known that DFT tends to underestimate activation energy. If all activation energies are underestimated, then their relative magnitude is correct and the order in which reactions are selected in KMC is also correct. However, this causes an unrealistic time evolution as a consequence of error propagation in the total rate (subsection 2.2.3). Hence, time advances slower than what is observed in practice.

Disparity between activation energies is the computational bottleneck of KMC. A more advanced model[108] has been proposed to handle this disparity. However, as a simple option, undesired reactions can be filtered or ignored. A point of interest can simply dictate which reaction type is filtered or ignored (section 5.6). The time evolution of the system is slightly disturbed again due to filtering out the unwanted reaction. However, the main points of interest of a system can be preserved and yield a reasonable solution or remarkable breakthrough.

Here, we assumed that ALD reactions are uncorrelated, which is a general principle in KMC. However, we should emphasize that this not a completely reasonable assumption. The energy produced from desorption of a ligand or densification of a precursor disperses among neighbouring atoms. In this situation, energy is scattered from minimum to minimum of the PES and cause biased dynamics or kinetics occurring with low activation energy. For instance, we predict that densification of the TMA precursor facilitates proton diffusion from the surface oxygen to the remaining ligands (section 4.3). Hence, more advanced techniques like accelerated MD[134,135] are required to investigate the kinetics of reactions sequences in ALD.

7.4 Problems well suited to being addressed by KMC

The KMC approach is equally applicable to many parallel systems. Battaile *et al.*[101] used KMC to simulate growth of material by a CVD process. To improve the understanding of CVD system, using c.n. and neighbour list (section 5.1) is suggested. The more complicated chemistry of a CVD, obtained by ab initio method,[136] is transferable to KMC through c.n. and neighbour list. However, special care is needed in considering activation energies. In most studies, the influence of neighbouring fragments on activation energies is constantly ignored for simplicity. In chapter 4, we discussed the essential role of the cooperative effect. Implementation of cooperative the effect for a CVD system is feasible

using c.n. and neighbour list.

Reuter *et al.*[37,104] used KMC for heterogeneous catalysis. In their excellent studies, the ab initio method provided details of reactions used as basic ingredients of a KMC model. It was recently shown[126,127] that adsorbate-adsorbate interaction results in change of dissociation barriers in heterogeneous catalysis. Implementation of adsorbate-adsorbate interactions at the surface into KMC may therefore cause an improvement in results. This implementation can be performed through c.n. and neighbour list that handle the mentioned chemistry locally.

An obvious extension of ALD growth simulation is to the initial cycles of growth on a particular substrate, to see how the substrate affects the interface and film structure. An example is the so-called "clean-up" of native oxide during ALD of oxides onto III-V substrates. Wallace *et al.*[137] measured self-cleaning of GaAs substrates by ALD of Al_2O_3 and HfO_2. Klejna *et al.*[138] determined the set of mechanism of clean-up during oxide ALD. After a limited number of cycles, surface oxygen atoms from the GaAs substrate move to the growing high-k material. This was shown using the shift of binding energy of reduced metals in *in situ* XPS spectra.[138] The interplay of this discovered reaction pathways can be examined through KMC approach. In such circumstances, the thickness of native oxide and number of cycles can be considered as macroscopic constraints and determined pathways and possible missed reaction pathways (*e.g.* adsorbate-adsorbate interactions, chapter 4) can be justified accurately.

The other technological research topic in ALD is the growth of transition metals.[3] This process requires reduction of a metal precursor so that the transition metal may be deposited.[17,139,140] Dey *et al.* simulated the reaction energetics of the metal precursor reduction. However, accurate activation energies of reaction pathways need to be calculated if they are to be used by KMC. We anticipate that metal diffusion at the surface increases the level of complexity of ALD chemistry. However, KMC is a suitable approach to handle transition metal ALD.

The ALD literature of metal alkylamide precursors is tiny in comparison with that of metal chloride precursors. In some cases therefore, we could not compare our KMC results with any experiment (section 6.2). However the prospects for validation are improving. We are collaborating with Cadien *et al.*[141] to investigate the roughness and dielectric properties of HfO_2 thin film grown by ALD. They use *in situ* spectroscopic ellipsometry to characterize composition, roughness, thickness, crystalline nature, doping concentration, electrical conductivity and other material properties during each pulse and from cycle to cycle. Ellipsometry is an optical technique that is very sensitive to the change of optical response when incident radiation is reflected/scattered by the sample. Rather than attempting to fit the optical parameters for bulk HfO_2 to the ellipsometry data for the growing

thin film, it may be possible to use the KMC predictions of film structure and ligand concentration to help interpret this experiment. Such collaboration is certainly likely to yield insights not accessible to either the computational or ellipsometry approaches alone.

Appendix A

List of all ALD reactions included in KMC calculation

Here, we list details of all implemented ALD reactions in KMC. The appendix contains three tables of different reaction types according to the number of sites involved (section 5.3). T was set to 500 K. The items in the tables are explained as follows.

The labels **from** and **to** indicate the initial and final chemical identity of a site. E_a is the activation energy. Here, **A** indicates either of two quantities: first, if the activation energy is 0.00, then **A** shows the adsorption rate of a precursor given by Maxwell-Boltzmann statistics (subsection 2.2.2). Second, **A** is the prefactor for an ALD reaction with a given activation energy (subsection 2.2.2). **coordination** shows the c.n. of the chemical identity of a site before execution of a reaction. Implementation of steric effect causes the c.n. of sites to become negative. Hence, those sites (oxygen sites) temporary lose their capability to adsorb further precursors. However, preserving the kinetics of proton diffusion over the oxygen site is essential to keep the growth rate balanced and therefore, the reaction of proton diffusion with negative c.n. is introduced. **pressureOn** shows the dependence of a reaction on the simulation time. If **pressureOn** is 0, this means that the associated reaction is independent of time and it is possible throughout of simulation time. If **pressureOn** is 1 or 2, this indicates that the associated reaction is only possible during metal or oxygen pulse, respectively.

from	to	A	E_a (eV)	coordination	pressureOn
O	HfX4O	44879.2084	0.00	1	1
HfX4O	O	1.042296E13	1.00	2	0
OH	HfX4OH	44879.2084	0.00	1	1
HfX4OH	OH	1.042296E13	1.00	2	0
HfX4OH	HfHX4O	1.042296E13	1.35	2	0
HfHX4O	HfX4OH	1.042296E13	1.76	2	0
HfHX4OH	HfH2X4O	1.042296E13	1.35	2	0
HfH2X4O	HfHX4OH	1.042296E13	1.76	2	0
HfX3OH	HfHX3O	1.042296E13	1.35	2	0

HfHX3O	HfX3OH	1.042296E13	1.76	2	0
HfH2X4OH	HfH3X4O	1.042296E13	1.35	2	0
HfH3X4O	HfH2X4OH	1.042296E13	1.76	2	0
HfH2X3O	HfHX3OH	1.042296E13	1.35	2	0
HfHX3OH	HfH2X3O	1.042296E13	1.76	2	0
HfH3X3O	HfH2X3OH	1.042296E13	1.35	2	0
HfH2X3OH	HfH3X3O	1.042296E13	1.76	2	0
HfH3X4OH	HfH4X4O	1.042296E13	1.35	2	0
HfH4X4O	HfH3X4OH	1.042296E13	1.76	2	0
HfHX4O	HfX3O	1.042296E13	0.89	2	0
HfX3O	HfHX4O	1.042296E13	1.24	2	0
HfHX3O	HfX2O	1.042296E13	1.69	2	0
HfX2O	HfHX3O	1.042296E13	2.87	2	0
HfHX4OH	HfX3OH	1.042296E13	0.89	2	0
HfX3OH	HfHX4OH	1.042296E13	1.24	2	0
HfH2X4O	HfHX3O	1.042296E13	0.89	2	0
HfHX3O	HfH2X4O	1.042296E13	1.83	2	0
HfH2X4OH	HfHX3OH	1.042296E13	0.89	2	0
HfHX3OH	HfH2X4OH	1.042296E13	1.83	2	0
HfH3X4O	HfH2X3O	1.042296E13	0.39	2	0
HfH2X3O	HfH3X4O	1.042296E13	0.83	2	0
HfH3X4OH	HfH2X3OH	1.042296E13	0.39	2	0
HfH2X3OH	HfH3X4OH	1.042296E13	0.83	2	0
HfH2X3OH	HfHX2OH	1.042296E13	1.09	2	0
HfHX2OH	HfH2X3OH	1.042296E13	4.01	2	0
HfH2X3O	HfHX2O	1.042296E13	1.09	2	0
HfHX2O	HfH2X3O	1.042296E13	4.01	2	0
HfH4X4O	HfH3X3O	1.042296E13	0.70	2	0
HfH3X3O	HfH4X4O	1.042296E13	2.82	2	0
HfH4X4OH	HfH3X3OH	1.042296E13	0.70	2	0
HfH3X3OH	HfH4X4OH	1.042296E13	2.82	2	0
HfHX3OH	HfX2OH	1.042296E13	1.69	0	0
HfX2OH	HfHX3OH	1.042296E13	2.87	0	0
HfHX3O	HfX2O	1.042296E13	1.69	0	0
HfX2O	HfHX3O	1.042296E13	2.87	0	0
HfH3X3OH	HfH2X2OH	1.042296E13	1.07	0	0
HfH2X2OH	HfH3X3OH	1.042296E13	3.99	0	0
HfH3X3O	HfH2X2O	1.042296E13	1.07	2	0
HfH2X2O	HfH3X3O	1.042296E13	3.99	2	0
HfH2X2	HfHX	1.042296E13	0.80	4	0
HfH2X2	HfHX	1.042296E13	0.30	5	0
HfH2X2	HfHX	1.042296E13	0.30	6	0
HfH2X2	HfHX	1.042296E13	0.30	7	0
HfH2X2	HfHX	1.042296E13	0.25	8	0
HfH2X2	Hf	1.042296E13	0.20	9	0
HfHX2	HfX	1.042296E13	0.89	5	0
HfHX2	HfX	1.042296E13	0.89	6	0
HfHX2	HfX	1.042296E13	0.80	7	0
HfHX2	HfX	1.042296E13	0.80	8	0
HfHX2	HfHX	1.042296E13	1.68	5	0
HfX	HfHX2	1.042296E13	1.92	5	0
HfX	HfHX2	1.042296E13	1.92	4	0
HfX2	HfX	1.042296E13	0.90	7	0
HfX	HfX2	1.042296E13	1.85	6	0
HfHX	Hf	1.042296E13	1.64	0	0
HfX	Hf	1.042296E13	0.64	7	0
HfHX	Hf	1.042296E13	0.83	6	0
HfHX	Hf	1.042296E13	0.56	7	0
OH2HfHX	OH2Hf	1.042296E13	0.50	7	0

OH2HfX	OH2Hf	1.042296E13	0.50	7	0
Hf	HfHX	1.042296E13	0.62	3	1
Hf	HfHX	1.042296E13	0.62	4	1
Hf	HfHX	1.042296E13	0.62	5	1
HfHX	Hf	1.042296E13	0.50	8	0
HfX	Hf	1.042296E13	0.50	8	0
HfX2	HfX	1.042296E13	2.00	0	0
HfHX2	HfX	1.042296E13	2.00	0	0
HfH2X2	HfHX	1.042296E13	2.00	0	0
Hf	OH2Hf	2.154290E5	0.00	4	2
OH2Hf	Hf	2.154290E5	0.00	4	2
Hf	OH2Hf	2.154290E5	0.00	5	2
OH2Hf	Hf	2.154290E5	0.00	5	2
Hf	OH2Hf	2.154290E5	0.00	6	2
OH2Hf	Hf	1.042296E13	0.46	6	0
OH2Hf	Hf	1.042296E13	0.83	5	0

Table A.1: This table contains reaction type α.

from	to	from	to	A	E_a (eV)	coordination	pressureOn
O	OH	OH2	OH	1.042296E13	0.40	1	0
O	OH	OH2	OH	1.042296E13	0.40	-9	0
O	OH	OH2	OH	1.042296E13	0.40	-19	0
O	OH	OH2	OH	1.042296E13	0.69	2	0
O	OH	OH2	OH	1.042296E13	0.69	-8	0
O	OH	OH2	OH	1.042296E13	0.69	-18	0
HfHX	OH2HfHX	HfHX	HfHX	2.154290E5	0.00	4	2
HfHX	OH2HfHX	HfHX	HfHX	2.154290E5	0.00	5	2
HfHX	OH2HfHX	HfHX	HfHX	2.154290E5	0.00	6	2
OH2HfHX	HfHX	HfHX	HfHX	2.154290E5	0.00	4	2
OH2HfHX	HfHX	HfHX	HfHX	2.154290E5	0.00	5	2
OH2HfHX	HfHX	HfHX	HfHX	2.154290E5	0.00	6	2
HfX	OH2HfX	HfX	HfX	2.154290E5	0.00	4	2
HfX	OH2HfX	HfX	HfX	2.154290E5	0.00	5	2
HfX	OH2HfX	HfX	HfX	2.154290E5	0.00	6	2
OH2HfX	HfX	HfX	HfX	2.154290E5	0.00	4	2
OH2HfX	HfX	HfX	HfX	2.154290E5	0.00	5	2
OH2HfX	HfX	HfX	HfX	2.154290E5	0.00	6	2
HfHX	OH2HfHX	HfX	HfX	2.154290E5	0.00	4	2
HfHX	OH2HfHX	HfX	HfX	2.154290E5	0.00	5	2
HfHX	OH2HfHX	HfX	HfX	2.154290E5	0.00	6	2
OH2HfHX	HfHX	HfX	HfX	2.154290E5	0.00	4	2
OH2HfHX	HfHX	HfX	HfX	2.154290E5	0.00	5	2
OH2HfHX	HfHX	HfX	HfX	2.154290E5	0.00	6	2
HfX	OH2HfX	HfHX	HfHX	2.154290E5	0.00	4	2
HfX	OH2HfX	HfHX	HfHX	2.154290E5	0.00	5	2
HfX	OH2HfX	HfHX	HfHX	2.154290E5	0.00	6	2
OH2HfX	HfX	HfHX	HfHX	2.154290E5	0.00	4	2
OH2HfX	HfX	HfHX	HfHX	2.154290E5	0.00	5	2
OH2HfX	HfX	HfHX	HfHX	2.154290E5	0.00	6	2
O	OH	OH	O	1.042296E13	0.46	1	0
O	OH	OH	O	1.042296E13	0.75	2	0
O	OH	OH	O	1.042296E13	0.46	-9	0
O	OH	OH	O	1.042296E13	0.75	-8	0
O	OH	OH	O	1.042296E13	0.46	-19	0
O	OH	OH	O	1.042296E13	0.75	-18	0
O	OH	OH	O	1.042296E13	0.46	-29	0
O	OH	OH	O	1.042296E13	0.75	-28	0
O	OH	OH	O	1.042296E13	0.95	3	0

HfX4O	HfX4OH	OH	O	1.042296E13	0.75	2	0
HfX4OH	HfX4O	O	OH	1.042296E13	0.75	2	0
HfHX4O	HfHX4OH	OH	O	1.042296E13	0.75	2	0
HfHX4OH	HfHX4O	O	OH	1.042296E13	0.75	2	0
HfH2X4O	HfH2X4OH	OH	O	1.042296E13	0.75	2	0
HfH2X4OH	HfH2X4O	O	OH	1.042296E13	0.75	2	0
HfH4X4O	HfH4X4OH	OH	O	1.042296E13	0.75	2	0
HfH4X4OH	HfH4X4O	O	OH	1.042296E13	0.75	2	0
HfH3X4O	HfH3X4OH	OH	O	1.042296E13	0.75	2	0
HfH3X4OH	HfH3X4O	O	OH	1.042296E13	0.75	2	0
HfHX3O	HfHX3OH	OH	O	1.042296E13	0.75	2	0
HfHX3OH	HfHX3O	O	OH	1.042296E13	0.75	2	0
HfX3O	HfX3OH	OH	O	1.042296E13	0.75	2	0
HfX3OH	HfX3O	O	OH	1.042296E13	0.75	2	0
HfH2X3O	HfH2X3OH	OH	O	1.042296E13	0.75	2	0
HfH2X3OH	HfH2X3O	O	OH	1.042296E13	0.75	2	0
HfH3X3O	HfH3X3OH	OH	O	1.042296E13	0.75	2	0
HfH3X3OH	HfH3X3O	O	OH	1.042296E13	0.75	2	0
HfX4O	HfHX4O	OH	O	1.042296E13	0.51	2	0
HfHX4O	HfX4O	O	OH	1.042296E13	0.64	2	0
HfX4OH	HfHX4OH	OH	O	1.042296E13	0.51	2	0
HfHX4OH	HfX4OH	O	OH	1.042296E13	0.64	2	0
HfHX4O	HfH2X4O	OH	O	1.042296E13	0.59	2	0
HfH2X4O	HfHX4O	O	OH	1.042296E13	0.76	2	0
HfHX4OH	HfH2X4OH	OH	O	1.042296E13	0.59	2	0
HfH2X4OH	HfHX4OH	O	OH	1.042296E13	0.76	2	0
HfH3X4OH	HfH4X4OH	OH	O	1.042296E13	0.42	2	0
HfH4X4OH	HfH3X4OH	O	OH	1.042296E13	2.72	2	0
HfH3X4O	HfH4X4O	OH	O	1.042296E13	0.42	2	0
HfH4X4O	HfH3X4O	O	OH	1.042296E13	2.72	2	0
HfH2X4OH	HfH3X4OH	OH	O	1.042296E13	0.49	2	0
HfH3X4OH	HfH2X4OH	O	OH	1.042296E13	0.81	2	0
HfH2X4O	HfH3X4O	OH	O	1.042296E13	0.49	2	0
HfH3X4O	HfH2X4O	O	OH	1.042296E13	0.81	2	0
HfX3O	HfHX3O	OH	O	1.042296E13	0.70	2	0
HfHX3O	HfX3O	O	OH	1.042296E13	0.98	2	0
HfX3OH	HfHX3OH	OH	O	1.042296E13	0.70	2	0
HfHX3OH	HfX3OH	O	OH	1.042296E13	0.98	2	0
HfHX3OH	HfH2X3OH	OH	O	1.042296E13	0.70	2	0
HfH2X3OH	HfHX3OH	O	OH	1.042296E13	0.98	2	0
HfHX3O	HfH2X3O	OH	O	1.042296E13	0.70	2	0
HfH2X3O	HfHX3O	O	OH	1.042296E13	0.98	2	0
HfH2X3O	HfH3X3O	OH	O	1.042296E13	0.38	2	0
HfH3X3O	HfH2X3O	O	OH	1.042296E13	0.20	2	0
HfH2X3OH	HfH3X3OH	OH	O	1.042296E13	0.38	2	0
HfH3X3OH	HfH2X3OH	O	OH	1.042296E13	0.20	2	0

Table A.2: This table contains reaction type β.

from	to	from	to	A	E_a (eV)	coordination	pressureOn
OH2HfX	HfX	VAC	OH2	1.042296E13	0.30	4	0
OH2HfX	HfX	VAC	OH2	1.042296E13	0.30	5	0
OH2HfX	HfX	VAC	OH2	1.042296E13	0.60	6	0
OH2HfHX	HfHX	VAC	OH2	1.042296E13	0.30	4	0
OH2HfHX	HfHX	VAC	OH2	1.042296E13	0.30	5	0
OH2HfHX	HfHX	VAC	OH2	1.042296E13	0.60	6	0
OH2Hf	Hf	VAC	OH2	1.042296E13	0.25	4	0
OH2Hf	Hf	VAC	OH2	1.042296E13	0.35	5	0
OH2Hf	Hf	VAC	OH2	1.042296E13	0.45	6	0

OH2	VAC	HfHX	OH2HfHX	1.042296E13	0.46	1	0
OH2	VAC	HfHX	OH2HfHX	1.042296E13	0.83	2	0
OH2	VAC	HfHX	OH2HfHX	1.042296E13	1.20	3	0
OH2	VAC	HfX	OH2HfX	1.042296E13	0.46	1	0
OH2	VAC	HfX	OH2HfX	1.042296E13	0.83	2	0
OH2	VAC	HfX	OH2HfX	1.042296E13	1.20	3	0
OH2	VAC	Hf	OH2Hf	1.042296E13	0.46	1	0
OH2	VAC	Hf	OH2Hf	1.042296E13	0.83	2	0
OH2	VAC	Hf	OH2Hf	1.042296E13	1.20	3	0
HfX2	HfHX2	OH	O	1.042296E13	0.91	0	0
HfHX2	HfX2	O	OH	1.042296E13	1.25	6	0
HfX	HfHX	OH	O	1.042296E13	0.70	0	0
HfHX	HfX	O	OH	1.042296E13	1.28	0	0
HfHX2	HfH2X2	OH	O	1.042296E13	0.88	0	0
HfH2X2	HfHX2	O	OH	1.042296E13	1.15	0	0
HfX2O	O	VAC	HfX2	1.042296E13	0.20	0	0
HfX2OH	OH	VAC	HfX2	1.042296E13	0.20	0	0
HfHX2O	O	VAC	HfHX2	1.042296E13	0.20	0	0
HfHX2OH	OH	VAC	HfHX2	1.042296E13	0.20	0	0
HfH2X2O	O	VAC	HfH2X2	1.042296E13	0.20	0	0
HfH2X2OH	OH	VAC	HfH2X2	1.042296E13	0.20	0	0
HfH4X4O	O	VAC	HfH2X2	1.042296E13	0.20	2	0
HfH4X4OH	OH	VAC	HfH2X2	1.042296E13	0.20	2	0
HfH2X2	VAC	O	HfH2X2O	1.042296E13	0.50	4	1
HfH2X2	VAC	O	HfH2X2O	1.042296E13	0.40	3	1
HfH2X2	VAC	OH	HfH2X2OH	1.042296E13	0.50	4	1
HfH2X2	VAC	OH	HfH2X2OH	1.042296E13	0.40	3	1
HfHX2	VAC	O	HfHX2O	1.042296E13	0.50	4	1
HfHX2	VAC	O	HfHX2O	1.042296E13	0.40	3	1
HfHX2	VAC	OH	HfHX2OH	1.042296E13	0.50	4	1
HfHX2	VAC	OH	HfHX2OH	1.042296E13	0.40	3	1
HfX2	VAC	O	HfX2O	1.042296E13	0.50	4	1
HfX2	VAC	O	HfX2O	1.042296E13	0.40	3	1
HfX2	VAC	OH	HfX2OH	1.042296E13	0.50	4	1
HfX2	VAC	OH	HfX2OH	1.042296E13	0.40	3	1

Table A.3: This table contains reaction type γ.

Bibliography

[1] Miikkulainen, V.; Leskela, M.; Ritala, M.; Puurunen, R. L. *Journal of Applied Physics* **2013**, *113*, 021301.

[2] George, S. M. *Chemical Reviews* **2010**, *110*, 111–131, PMID: 19947596.

[3] Elliott, S. D. *Langmuir* **2010**, *26*, 9179–9182.

[4] O'Mahony, A.; Monaghan, S.; Chiodo, R.; Povey, I.; Cherkaoui, K.; Nagle, R.; O'Connor, E.; Long, R.; Djara, V.; O'Connell, D.; Crupi, F.; Pemble, M.; Hurley, P. K. *ECS Transactions* **2010**, *33*, 69–82.

[5] Hurley, P. K. et al. *ECS Transactions* **2009**, *25*, 113–127.

[6] Leskela, M.; Ritala, M. *Angewandte Chemie International Edition* **2003**, *42*, 5548–5554.

[7] Rahtu, A.; Ritala, M. *Langmuir* **2002**, *18*, 10046–10048.

[8] Elers, K.-E.; Saanila, V.; Soininen, P. J.; Li, W.-M.; Kostamo, J. T.; Haukka, S.; Juhanoja, J.; Besling, W. F. A. *Chemical Vapor Deposition* **2002**, *8*, 149–153.

[9] Ritala, M.; Kalsi, P.; Riihela, D.; Kukli, K.; Leskela, M.; Jokinen, J. *Chemistry of Materials* **1999**, *11*, 1712–1718.

[10] Alen, P.; Juppo, M.; Ritala, M.; Sajavaara, T.; Keinonen, J.; Leskela, M. *Journal of The Electrochemical Society* **2001**, *148*, G566–G571.

[11] Juppo, M.; Ritala, M.; Leskela, M. *Journal of The Electrochemical Society* **2000**, *147*, 3377–3381.

[12] Juppo, M.; Alen, P.; Ritala, M.; Sajavaara, T.; Keinonen, J.; Leskela, M. *Electrochemical and Solid-State Letters* **2002**, *5*, C4–C6.

[13] Park, J.-S.; Park, H.-S.; Kang, S.-W. *Journal of The Electrochemical Society* **2002**, *149*, C28–C32.

[14] Klaus, J. W.; Ferro, S. J.; George, S. M. *Journal of The Electrochemical Society* **2000**, *147*, 1175–1181.

[15] Smith, S.; Li, W.-M.; Elers, K.-E.; Pfeifer, K. *Microelectronic Engineering* **2002**, *64*, 247 – 253, <ce:title>MAM2002</ce:title>.

[16] Maartensson, P.; Carlsson, J. *Journal of The Electrochemical Society* **1998**, *145*, 2926–2931.

[17] Lee, B.; Hwang, J.; Nam, J.; Lee, S.; Kim, J.; Koo, S.-M.; Baunemann, A.; Fischer, R.; Sung, M. *Angewandte Chemie International Edition* **2009**, *48*, 4536–4539.

[18] Aaltonen, T.; Alen, P.; Ritala, M.; Leskela, M. *Chemical Vapor Deposition* **2003**, *9*, 45–49.

[19] Rossnagel, S. M.; Sherman, A.; Turner, F. *Journal of Vacuum Science and Technology B* **2000**, *18*, year.

[20] Lee, Y. J.; Kang, S.-W. *Electrochemical and Solid-State Letters* **2002**, *5*, C91–C93.

[21] Chae, J.; Park, H.-S.; Kang, S.-w. *Electrochemical and Solid-State Letters* **2002**, *5*, C64–C66.

[22] Wilk, G. D.; Wallace, R. M.; Anthony, J. M. *Journal of Applied Physics* **2001**, *89*, 5243–5275.

[23] Puurunen, R. L. *Journal of Applied Physics* **2005**, *97*, 121301.

[24] Delabie, A.; Caymax, M.; Brijs, B.; Brunco, D.; Conard, T.; Sleeckx, E.; Ragnarsson, L.-A.; Van Elshocht, S.; De Gendt, S.; Heyns, M. *ECS Transactions* **2006**, *1*, 433–446.

[25] Hausmann, D. M.; Kim, E.; Becker, J.; Gordon, R. G. *Chemistry of Materials* **2002**, *14*, 4350–4358.

[26] Hausmann, D. M.; Gordon, R. G. *Journal of Crystal Growth* **2003**, *249*, 251 – 261.

[27] Karavaev, K. *In-Situ X-ray photoelectron spectroscopy data, PhD thesis*; University of Tech. Cottbus and BESSY, 2009; p 32.

[28] Jeloaica, L.; Esteve, A.; Rouhani, M. D.; Esteve, D. *Applied Physics Letters* **2003**, *83*, 542–544.

[29] Widjaja, Y.; Musgrave, C. B. *The Journal of Chemical Physics* **2002**, *117*, 1931–1934.

[30] Mukhopadhyay, A. B.; Musgrave, C. B.; Sanz, J. F. *Journal of the American Chemical Society* **2008**, *130*, 11996–12006.

[31] Cho, M.; Park, H. B.; Park, J.; Lee, S. W.; Hwang, C. S.; Jang, G. H.; Jeong, J. *Applied Physics Letters* **2003**, *83*, 5503–5505.

[32] Elliott, S. D. *In Rare earth oxide thin films: growth, characterization, and applications*; Springer-Verlag Berlin, Heidelberger Platz 3, D-14197 Berlin: Germany, 2007.

[33] Musgrave, C. B. In *Theoretical Modeling of ALD Processes*; Wiley-VCH Verlag GmbH and Co. KGaA, 2011; pp 1–21.

[34] Elliott, S. D. *Atomic Layer Deposition for Semiconductors*; Springer-Verlag Berlin, Heidelberger Platz 3, D-14197 Berlin: Germany, 2013.

[35] Bartlett, R. J.; Musiał, M. *Rev. Mod. Phys.* **2007**, *79*, 291–352.

[36] Greer, J. *Journal of Computational Physics* **1998**, *146*, 181 – 202.

[37] Reuter, K. In *First-Principles Kinetic Monte Carlo Simulations for Heterogeneous Catalysis: Concepts, Status, and Frontiers*; Wiley-VCH Verlag GmbH and Co. KGaA, 2011; pp 71–111.

[38] Voter, A. INTRODUCTION TO THE KINETIC MONTE CARLO METHOD. In *Radiation Effects in Solids*; Sickafus, K., Kotomin, E., Uberuaga, B., Eds.; Springer Netherlands, 2007; Vol. 235, pp 1–23.

[39] Bortz, A.; Kalos, M.; Lebowitz, J. *Journal of Computational Physics* **1975**, *17*, 10 – 18.

[40] Neizvestny, I.; Shwartz, N.; Yanovitskaja, Z. S.; Zverev, A. *Computational Materials Science* **2006**, *36*, 36 – 41.

[41] Kresse, G.; Hafner, J. *Phys. Rev. B* **1993**, *47*, 558–561.

[42] Hafner, J. *Journal of Computational Chemistry* **2008**, *29*, 2044–2078.

[43] Blöchl, P. E. *Phys. Rev. B* **1994**, *50*, 17953–17979.

[44] Slater, J. C. *Phys. Rev.* **1930**, *35*, 210–211.

[45] Aryasetiawan, F.; Gunnarsson, O. *Reports on Progress in Physics* **1998**, *61*, 237.

[46] Slater, J. C. *Phys. Rev.* **1951**, *81*, 385–390.

[47] Hohenberg, P.; Kohn, W. *Phys. Rev.* **1964**, *136*, B864–B871.

[48] Kohn, W.; Sham, L. J. *Phys. Rev.* **1965**, *140*, A1133–A1138.

[49] Almbladh, C.-O.; von Barth, U. *Phys. Rev. B* **1985**, *31*, 3231–3244.

[50] Staroverov, V. N.; Scuseria, G. E.; Tao, J.; Perdew, J. P. *The Journal of Chemical Physics* **2003**, *119*, 12129–12137.

[51] Perdew, J. P.; Burke, K.; Ernzerhof, M. *Phys. Rev. Lett.* **1996**, *77*, 3865–3868.

[52] Becke, A. D. *The Journal of Chemical Physics* **1993**, *98*, 5648–5652.

[53] Stephens, P. J.; Devlin, F. J.; Chabalowski, C. F.; Frisch, M. J. *The Journal of Physical Chemistry* **1994**, *98*, 11623–11627.

[54] Car, R.; Parrinello, M. *Phys. Rev. Lett.* **1985**, *55*, 2471–2474.

[55] Feynman, R. P. *Phys. Rev.* **1939**, *56*, 340–343.

[56] Hybertsen, M. S.; Louie, S. G. *Phys. Rev. B* **1986**, *34*, 5390–5413.

[57] Held, K.; Andersen, O. K.; Feldbacher, M.; Yamasaki, A.; Yang, Y.-F. *Journal of Physics: Condensed Matter* **2008**, *20*, 064202.

[58] Georges, A.; Kotliar, G.; Krauth, W.; Rozenberg, M. J. *Rev. Mod. Phys.* **1996**, *68*, 13–125.

[59] Perdew, J. P.; Schmidt, K. *AIP Conference Proceedings* **2001**, *577*, 1–20.

[60] Perdew, J. P.; Zunger, A. *Phys. Rev. B* **1981**, *23*, 5048–5079.

[61] Perdew, J. P.; Wang, Y. *Phys. Rev. B* **1992**, *45*, 13244–13249.

[62] Voorhis, T. V.; Scuseria, G. E. *The Journal of Chemical Physics* **1998**, *109*, 400–410.

[63] Perdew, J. P.; Kurth, S.; Zupan, A. b. u.; Blaha, P. *Phys. Rev. Lett.* **1999**, *82*, 5179–5179.

[64] Harris, J.; Jones, R. O. *Journal of Physics F: Metal Physics* **1974**, *4*, 1170.

[65] Gunnarsson, O.; Lundqvist, B. I. *Phys. Rev. B* **1976**, *13*, 4274–4298.

[66] Wigner, E. *Phys. Rev.* **1934**, *46*, 1002–1011.

[67] Oliver, G. L.; Perdew, J. P. *Phys. Rev. A* **1979**, *20*, 397–403.

[68] Armiento, R.; Mattsson, A. E. *Phys. Rev. B* **2005**, *72*, 085108.

[69] Perdew, J. P.; Ruzsinszky, A.; Csonka, G. I.; Vydrov, O. A.; Scuseria, G. E.; Constantin, L. A.; Zhou, X.; Burke, K. *Phys. Rev. Lett.* **2008**, *100*, 136406.

[70] Wu, Z.; Cohen, R. E. *Phys. Rev. B* **2006**, *73*, 235116.

[71] Moroni, E. G.; Kresse, G.; Hafner, J.; Furthmüller, J. *Phys. Rev. B* **1997**, *56*, 15629–15646.

[72] Constantin, L. A.; Perdew, J. P.; Tao, J. *Phys. Rev. B* **2006**, *73*, 205104.

[73] Staroverov, V. N.; Scuseria, G. E.; Tao, J.; Perdew, J. P. *Phys. Rev. B* **2004**, *69*, 075102.

[74] Tao, J.; Perdew, J. P.; Staroverov, V. N.; Scuseria, G. E. *Phys. Rev. Lett.* **2003**, *91*, 146401.

[75] Vosko, S. H.; Wilk, L.; Nusair, M. *Canadian Journal of Physics* **1980**, *58*, 1200–1211.

[76] Lee, C.; Yang, W.; Parr, R. G. *Phys. Rev. B* **1988**, *37*, 785–789.

[77] Adamo, C.; Barone, V. *The Journal of Chemical Physics* **1999**, *110*, 6158–6170.

[78] Jaramillo, J.; Scuseria, G. E.; Ernzerhof, M. *The Journal of Chemical Physics* **2003**, *118*, 1068–1073.

[79] Dudarev, S. L.; Botton, G. A.; Savrasov, S. Y.; Humphreys, C. J.; Sutton, A. P. *Phys. Rev. B* **1998**, *57*, 1505–1509.

[80] Liechtenstein, A. I.; Anisimov, V. I.; Zaanen, J. *Phys. Rev. B* **1995**, *52*, R5467–R5470.

[81] Rohrbach, A.; Hafner, J.; Kresse, G. *Journal of Physics: Condensed Matter* **2003**, *15*, 979.

[82] Nolan, M.; Elliott, S. D.; Mulley, J. S.; Bennett, R. A.; Basham, M.; Mulheran, P. *Phys. Rev. B* **2008**, *77*, 235424.

[83] Petersen, M.; Hafner, J.; Marsman, M. *Journal of Physics: Condensed Matter* **2006**, *18*, 7021.

[84] Wigner, E. *Trans. Faraday Soc.* **1938**, *34*, 29–41.

[85] Eyring, H. *The Journal of Chemical Physics* **1935**, *3*, 107–115.

[86] Wert, C.; Zener, C. *Phys. Rev.* **1949**, *76*, 1169–1175.

[87] Vineyard, G. H. *Journal of Physics and Chemistry of Solids* **1957**, *3*, 121 – 127.

[88] G. Henkelman, G. J.; Jonsson, H. *Methods for finding saddle points and minimum energy paths*; Kluwer Academic: New York, 2000.

[89] Mills, G.; Jónsson, H. *Phys. Rev. Lett.* **1994**, *72*, 1124–1127.

[90] Uberuaga, B. P.; Leskovar, M.; Smith, A. P.; Jónsson, H.; Olmstead, M. *Phys. Rev. Lett.* **2000**, *84*, 2441–2444.

[91] Mills, G.; Jónsson, H.; Schenter, G. K. *Surface Science* **1995**, *324*, 305 – 337.

[92] H. Jonsson, G. M.; Jacobsen, K. W. *Nudged elastic band method for finding minimum energy paths of transitions*; World Scientific: Singapore, 1998; p 385.

[93] Payne, M. C.; Teter, M. P.; Allan, D. C.; Arias, T. A.; Joannopoulos, J. D. *Rev. Mod. Phys.* **1992**, *64*, 1045–1097.

[94] Adomaitis, R. A. *Chemical Vapor Deposition* **2011**, *17*, 353–365.

[95] Shirazi, M.; Elliott, S. D. *Chemistry of Materials* **2013**, *25*, 878–889.

[96] Puurunen, R. *Chemical Vapor Deposition* **2003**, *9*, 249–257.

[97] Alam, M. A.; Green, M. L. *Journal of Applied Physics* **2003**, *94*, 3403–3413.

[98] Hu, Z.; Shi, J.; Heath Turner, C. *Molecular Simulation* **2009**, *35*, 270–279.

[99] Groner, M. D.; Fabreguette, F. H.; Elam, J. W.; George, S. M. *Chemistry of Materials* **2004**, *16*, 639–645.

[100] Amar, J. *Computing in Science Engineering* **2006**, *8*, 9 –19.

[101] Battaile, C. C.; Srolovitz, D. J. *Annual Review of Materials Research* **2002**, *32*, 297–319.

[102] Dkhissi, A.; Esteve, A.; Mastail, C.; Olivier, S.; Mazaleyrat, G.; Jeloaica, L.; Djafari Rouhani, M. *Journal of Chemical Theory and Computation* **2008**, *4*, 1915–1927.

[103] El-Mellouhi, F.; Mousseau, N.; Lewis, L. J. *Phys. Rev. B* **2008**, *78*, 153202.

[104] Reuter, K.; Frenkel, D.; Scheffler, M. *Phys. Rev. Lett.* **2004**, *93*, 116105.

[105] Amar, J. G. *Computing in Science and Engineering* **2006**, *8*, 9–19.

[106] Gillespie, D. T. *The Journal of Physical Chemistry* **1977**, *81*, 2340–2361.

[107] Mazaleyrat, G.; Estève, A.; Jeloaica, L.; Djafari-Rouhani, M. *Computational Materials Science* **2005**, *33*, 74 – 82.

[108] Chatterjee, A.; Voter, A. F. *The Journal of Chemical Physics* **2010**, *132*, 194101.

[109] Plimpton, S.; Battaile, C.; Chandross, M.; Holm, L.; Thompson, A.; Tikare, V.; Wagner, G.; Webb, E.; Zhou, X.; Cardona, C. G.; Slepoy, A. In *Crossing the Mesoscale No-Man's Land via Parallel Kinetic Monte Carlo*; Sandia report, 2009.

[110] Slepoy, A.; Thompson, A. P.; Plimpton, S. J. *The Journal of Chemical Physics* **2008**, *128*, 205101.

[111] Olivier, S.; Ducere, J.-M.; Mastail, C.; Landa, G.; Esteve, A.; Rouhani, M. D. *Chemistry of Materials* **2008**, *20*, 1555–1560.

[112] Kohn, W.; Becke, A. D.; Parr, R. G. *The Journal of Physical Chemistry* **1996**, *100*, 12974–12980.

[113] Harris, J. *Phys. Rev. B* **1985**, *31*, 1770–1779.

[114] Kresse, G.; Hafner, J. *Journal of Physics: Condensed Matter* **1994**, *6*, 8245.

[115] Elliott, S. D.; Greer, J. C. *J. Mater. Chem.* **2004**, *14*, 3246–3250.

[116] Zhao, X.; Vanderbilt, D. *Phys. Rev. B* **2002**, *65*, 233106.

[117] Aarik, J.; Aidla, A.; Kiisler, A.-A.; Uustare, T.; Sammelselg, V. *Thin Solid Films* **1999**, *340*, 110 – 116.

[118] Mukhopadhyay, A. B.; Sanz, J. F.; Musgrave, C. B. *Chemistry of Materials* **2006**, *18*, 3397–3403.

[119] Monkhorst, H. J.; Pack, J. D. *Phys. Rev. B* **1976**, *13*, 5188–5192.

[120] Kresse, G.; Hafner, J. *Phys. Rev. B* **1994**, *49*, 14251–14269.

[121] Ruggerone, P.; Ratsch, C.; Scheffler, M. Chapter 13 Density-functional theory of epitaxial growth of metals. In *Growth and Properties of Ultrathin Epitaxial Layers*; King, D., Woodruff, D., Eds.; Elsevier, 1997; Vol. 8, pp 490 – 544.

[122] Henkelman, G.; Uberuaga, B. P.; Jonsson, H. *The Journal of Chemical Physics* **2000**, *113*, 9901–9904.

[123] Henkelman, G.; Jonsson, H. *The Journal of Chemical Physics* **2000**, *113*, 9978–9985.

[124] Zydor, A.; Kessler, V. G.; Elliott, S. D. *Phys. Chem. Chem. Phys.* **2012**, *14*, 7954–7964.

[125] Weinreich, W.; Tauchnitz, T.; Polakowski, P.; Drescher, M.; Riedel, S.; Sundqvist, J.; Seidel, K.; Shirazi, M.; Elliott, S. D.; Ohsiek, S.; Erben, E.; Trui, B. *Journal of Vacuum Science and Technology A: Vacuum, Surfaces, and Films* **2013**, *31*, 01A123.

[126] Honkala, K.; Hellman, A.; Remediakis, I. N.; Logadottir, A.; Carlsson, A.; Dahl, S.; Christensen, C. H.; Nørskov, J. K. *Science* **2005**, *307*, 555–558.

[127] Miller, D. J.; Oberg, H.; Naslund, L.-A.; Anniyev, T.; Ogasawara, H.; Pettersson, L. G. M.; Nilsson, A. *The Journal of Chemical Physics* **2010**, *133*, 224701.

[128] Elliott, S. D.; Scarel, G.; Wiemer, C.; Fanciulli, M.; Pavia, G. *Chemistry of Materials* **2006**, *18*, 3764–3773.

[129] Elliott, S. D. *Semiconductor Science and Technology* **2012**, *27*, 074008.

[130] Nyns, L.; Delabie, A.; Swerts, J.; Van Elshocht, S.; De Gendt, S. *Journal of The Electrochemical Society* **2010**, *157*, G225–G229.

[131] Knapas, K.; Ritala, M. *Critical Reviews in Solid State and Materials Sciences* **2013**, *38*, 167–202.

[132] Hausmann, D. M. *Atomic layer deposition of metal oxide thin films, PhD thesis*; Harvard University, Cambridge, Massachusetts, 2002.

[133] Shirazi, M.; Elliott, S. D. *Journal of Computational Chemistry* **2014**, *35*, 244–259.

[134] Perez, D.; Uberuaga, B. P.; Shim, Y.; Amar, J. G.; Voter, A. F. Chapter 4 Accelerated Molecular Dynamics Methods: Introduction and Recent Developments; Elsevier, 2009; Vol. 5, pp 79 – 98.

[135] Voter, A. F.; Montalenti, F.; Germann, T. C. *Annual Review of Materials Research* **2002**, *32*, 321–346.

[136] Fang, Z.; Dixon, D. A. *The Journal of Physical Chemistry C* **2013**, *117*, 7459–7474.

[137] Hinkle, C. L.; Sonnet, A. M.; Vogel, E. M.; McDonnell, S.; Hughes, G. J.; Milojevic, M.; Lee, B.; Aguirre-Tostado, F. S.; Choi, K. J.; Kim, H. C.; Kim, J.; Wallace, R. M. *Applied Physics Letters* **2008**, *92*, 071901.

[138] Klejna, S.; Elliott, S. D. *The Journal of Physical Chemistry C* **2012**, *116*, 643–654.

[139] Vidjayacoumar, B.; Emslie, D. J. H.; Blackwell, J. M.; Clendenning, S. B.; Britten, J. F. *Chemistry of Materials* **2010**, *22*, 4854–4866.

[140] Vidjayacoumar, B.; Emslie, D. J. H.; Clendenning, S. B.; Blackwell, J. M.; Britten, J. F.; Rheingold, A. *Chemistry of Materials* **2010**, *22*, 4844–4853.

[141] Foroughi-Abari, A.; Cadien, K. C. *Journal of The Electrochemical Society* **2011**, *159*, D59–D64.